2015-5

Surface Plasmon Polaritons Based Nanophotonic Devices and their Applications

Youqiao Ma
Technological University Dublin

Surface Plasmon Polaritons based Nanophotonic Devices and their Applications

A Thesis presented for the Degree of

Doctor of Philosophy

by

Youqiao Ma, *MSc*.

Supervisors: Dr. Qiang Wu, Prof. Yuliya Semenova and Prof. Gerald Farrell

School of Electrical and Electronic Engineering

College of Engineering & Built Environment

Dublin Institute of Technology

Dublin, Ireland

May 2015

To my beloved wife and son, parents and siblings,

teachers and friends

Declaration

I certify that this thesis which I now submit for examination for the award of Doctor of Philosophy, is entirely my own work and has not been taken from the work of others, save and to the extent that such work has been cited and acknowledged within the text of my work.

This thesis was prepared according to the regulations for postgraduate study by research of the Dublin Institute of Technology and has not been submitted in whole or in part for another award in any other third level institution.

The work reported on in this thesis conforms to the principles and requirements of the Dublin Institute of Technology's guidelines for ethics in research.

DIT has permission to keep, lend or copy this thesis in whole or in part, on condition that any such use of the material of the thesis is duly acknowledged.

Signature _____ Date _____

Acknowledgements

This four years PhD study at DIT Photonic Research Center (PRC) has become the most significant period of time in my life. At this stage, I owe a great appreciation to many people around me who had helped and supported me during this phase so that I could complete my thesis.

First and foremost, I would like to thank my supervisor Dr. Qiang Wu for giving me an opportunity to work with him. I reserve my gratitude for his constant guidance and support over all these years. I am also grateful to him for creating good lab facilities that helped me to carry out my research work smoothly and independently. His enthusiasm, encouragement, advice, inspiration, patience, and great efforts for explaining things simply and clearly, made my thesis work more effective.

I also would like to give a huge amount of thanks to my co-supervisors Prof. Yuliya Semenova and Prof. Gerald Farrell for their invaluable suggestions, encouragement, and support on my research. Their positive attitude and advice gave me the confidence to approach many problems both in research and life. I also want to sincerely thank them for the careful reading, comments and perspectives given to my thesis.

Special thanks to my fellow colleagues at the PRC: Pengfei Wang, Ginu Rajan, Sunish Mathews, Jinesh Mathew, Manjusha Ramakrishnan, Lin Bo, Vishnu Kavungal, Arun Kumar Mallik, Dejun Liu, Wei Han, Binghui Li, Sha Li, Zhe Kang, and Hui Xiao for their support and friendship.

I am deeply indebted to my previous supervisor Prof. Jun Zhou for giving me the motivation and encouragement during my master's research at Ningbo University in China. His guidance and suggestions helped me immensely during the initial years of my research.

Many thanks to my friends in Ireland, Sinan Bunni, Arran Kennedy, Shelley Xiong, Luke

Slott, Zoe Obeimhen, and Tom Doyle, who have motivated me a lot and given their help from time to time, especially for the occasional dinner parties, which made my life more enjoyable in Ireland.

I am highly thankful to my wife Hongyan Zhu who supported and looked after me for past 4 years. Thanks to her patience and understanding. Particularly we had our cute son Aiyu Ma born in the later stages of my PhD studentship. Sincere best wishes to him for a very happy future.

I wish to thank to my elder sister Yue Ma for her support and prayers. I also would like to thank my entire extended family, my sister in law, bother in law, cousins, uncles, and aunties.

Finally, I want to thank my parents and parents in law for everything. Without their endless love, encouragement and support, I would not be able to reach in this point of my life.

Youqiao Ma

List of Publications

Journal Papers

1. **Youqiao Ma**, Gerald Farrell, Yuliya Semenova, Binghui Li, Jinhui Yuan, Chongxiu Yu, and Qiang Wu, Optical nanofiber-loaded surface plasmonic TE-pass polarizer, **Optics and Laser Technology**, under review.
2. **Youqiao Ma**, Gerald Farrell, Yuliya Semenova, and Qiang Wu, A hybrid wedge-to-wedge plasmonic waveguide with low loss propagation and ultra-deep-nanoscale mode confinement, **IEEE, Journal of Lightwave Technology**, in press.
3. **Youqiao Ma**, Gerald Farrell, Yuliya Semenova, and Qiang Wu, Hybrid nanowedge plasmonic waveguide for low loss propagation with ultra-deep-subwavelength mode confinement, **Optics Letters**, 973-976 (39) 2014.
4. **Youqiao Ma**, Gerald Farrell, Yuliya Semenova, Hau Ping Chan, Hongzhou Zhang, and Qiang Wu, Low loss, high extinction ratio and ultra-compact plasmonic polarization beam splitter, **IEEE, Photonics Technology Letters**, 660-663 (26) 2014.
5. **Youqiao Ma**, Gerald Farrell, Yuliya Semenova, Hauping Chan, Hongzhou Zhang, Qiang Wu, Sensitivity Enhancement for a Multimode Fiber Sensor with an Axisymmetric Metal Grating Layer, **Photonics and Nanostructures - Fundamentals and Applications**, 69-74 (12) 2014.
6. **Youqiao Ma**, Gerald Farrell, Yuliya Semenova, Hauping Chan, Hongzhou Zhang, Qiang Wu, Novel dielectric loaded plasmonic waveguide for tight-confined hybrid plasmon mode, **Plasmonics**, 1259-1263 (8) 2013.
7. **Youqiao Ma**, Gerald Farrell, Yuliya Semenova, Hauping Chan, Qiang Wu, Hybrid

plasmonic biosensor for simultaneous measurement of both thickness and refractive index, **Infrared Physics & Technology**, 134-136 (60) 2013.

8. **Youqiao Ma**, Gerald Farrell, Yuliya Semenova, Qiang Wu, Analysis and applications of nanocavity structures used as tunable filters and sensors, **Infrared Physics & Technology**, 389-394 (55) 2012.
9. P. Wang, T. Lee, M. Ding, Z. Lian, X. Feng, **Y. Ma**, L. Bo, Q. Wu, Y. Semenova, W. Loh, G. Farrell and G. Brambilla, White Light Trapping Using Supercontinuum Generation Spectra in a Lead-Silicate Fibre Taper, **IEEE, Journal of Lightwave Technology**, 40-45 (32) 2014.
10. Q. Wu, H. Chan, J. Yuan, **Y. Ma**, M. Yang, Y. Semenova, B. Yan, P. Wang, C. Yu, and G. Farrell, "Enhanced refractive index sensor using a combination of a long peroid fiber grating and a small core singlemode fiber structure," **Measurement Science and Technology**, 094002 (24) 2013.
11. Qiang Wu, **Youqiao Ma**, Jinhui Yuan, Yuliya Semenova, Pengfei Wang, Chongxiu Yu, and Gerald Farrell, "Evanescent field coupling between two parallel close contact SMS fiber structures," **Optics Express**, 3098-3109 (20) 2012.
12. Qiang Wu, Yuliya Semenova, **Youqiao Ma**, Pengfei Wang, Tuan Guo, Long Jin and Gerald Farrell, "Light coupling between a singlemode- multimode-singlemode (SMS) fiber structure and a long period fiber grating," **Journal of Lightwave Technology**, 3683-3688 (29) 2011.
13. Qiang Wu, Yuliya Semenova, Binbin Yan, **Youqiao Ma**, Pengfei Wang, Chongxiu Yu and Gerald Farrell, "Fiber refractometer based on a fiber Bragg grating and single-mode–multimode–single-mode fiber structure," **Optics Letters**, 2197-2199 (36) 2011.

Conference Proceedings

1. **Youqiao Ma**, Gerald Farrell, Yuliya Semenova, and Qiang Wu, Hybrid waveguide based long range suface plasmon biosensor, **SPIE Nanoscience+Engineering**, 8812, 2013. **Oral presentation.**
2. **Youqiao Ma**, G. Farrell, Y. Semenova, Qiang Wu, Novel Bragg Reflector and High-Q Cavity based on Dielectric Loaded Plasmonic Waveguide, **Photonics Ireland**, 4th -6th, Belfast, UK (2013).
3. **Youqiao Ma**, Gerald Farrell, Yuliya Semenova, H. P. Chan and Qiang Wu, High sensitivity refractive index sensor based on multimode fiber coated with axisymmetric metal grating layer, **Communications and Photonics Conference (ACP)**, 2162, 2012.
4. **Youqiao Ma**, Gerald Farrell, Yuliya Semenova, H. P. Chan and Qiang Wu, A Novel Biosensor based on a Coupled Surface Plasmon Nanostructure, **Optical fiber sensors (OFS)**, 8421, 2012.
5. **Youqiao Ma**, Gerald Farrell, Yuliya Semenova and Qiang Wu, A Novel Nano-Plasmonic band-gap Splitter based on a T-shaped Bragg Grating Waveguide, **SPIE Photonics Europe**, 8424, 2012.
6. **Youqiao Ma**, Qiang Wu, Y. Semenova, G. Farrell, The influence of the structure of a sub-wavelength metal grating on its transmission efficiency, **Photonics Ireland**, A56, 2011.
7. Qiang Wu, **Youqiao Ma**, Yuliya Semenova, Pengfei Wang, H. P. Chan and Gerald Farrell, Enhanced RI sensor using a combination of a long period fiber grating and a small core singlemode fiber (SCSMF) structure, **Optical fiber sensors (OFS)**, 8421, 2012.
8. Qiang Wu, **Youqiao Ma**, Lin Bo, Pengfei Wang, Yuliya Semenova, Gerald Farrell,

Singlemode hetero-core fiber based refractometer demodulated in a ratiometric system, **IEEE sensors**, 402-404, 2011.

Abstract

Guiding light at the nanoscale shows significant importance for the next generation on-chip information technology, as it could enable dramatic miniaturization of integrated photonic circuits (IPCs). Conventional dielectric photonic devices cannot be used to realize highly IPCs due to the diffraction limit. A promising solution to this challenge is to explore surface plasmon polaritons (SPPs) based waveguides, which can guide light beyond the diffraction limit. Therefore, a deeper understanding of SPPs based waveguides is developed in this thesis, as a basis for the design of novel plasmonic devices which are essential for building IPCs.

However inherent ohmic loss in plasmonic waveguide is very large and the loss will be further increased by reducing the size of IPCs, which limited their applications. Thus the critical challenge for SPPs waveguide is how to increase the propagation length, in the meanwhile maintain a tight mode confinement. Thus several novel plasmonic waveguides are developed to address the challenge of improving the propagation length while maintaining very tight mode confinement.

SPPs are exceptionally sensitive to the dielectric properties near the metal surface because of their highly localized fields at the metal surface, offering substantial potential for effective sensing applications. Therefore the application for plasmonic sensing is also explored in the thesis. Several new plasmonic biosensors are designed to achieve a high sensitivity and simultaneous measurements of multiple parameters.

Table of Contents

List of Figures

List of Abbreviations

ASM	Anti-symmetric Mode
ATR	Attenuated Total Reflection
BPM	Beam Propagation Method
BTHSPPs	Bow-Tie Hybrid Surface Plasmon Polaritons
CMT	Coupled Mode Theory
CRM	Cavity Resonance Mode
DLSPPs	Dielectric-Loaded Surface Plasmon Polaritons
DNA	Deoxyribonucleic Acid
EBL	Electron-Beam Lithography
EM	Electromagnetic
EMT	Effective Medium Theory
ER	Extinction Ratio
ERIMC	Effective Refractive Index Matching Condition
FDTD	Finite-Difference Time-Domain
FEM	Finite Element Method
FFT	Fast Fourier Transformation
FIB	Focused Ion Beam
FP	Fabry-Perot

HPCM	Hybrid Plasmonic-Cavity Mode
HRI	High Refractive Index
HSPPs	Hybrid Surface Plasmon Polaritons
IL	Insertion Loss
IMI	Insulator-Metal-Insulator
IPCs	Integrated Photonic Circuits
LRDLSPPs	Long Range DLSPPs
LRHSPPs	Long Range HSPPs
LRI	Low Refractive Index
LRSPPs	Long Range Surface Plasmon Polaritons
LRWHSPPs	Long Range Nanowedge HSPPs
LRWWHSPPs	Long Range Wedge-to-Wedge HSPPs
LSPPs	Localized Surface Plasmon Polaritons
MC	Mode Character
MFLSPPs	Microfiber Loaded Surface Plasmon Polaritons
MG	Metal Grating
MIM	Metal-Insulator-Metal
MoM	Method of Moment
OSA	Optical Spectrum Analyzer
PBS	Polarization Beam Splitter
PML	Perfect Matched Layer

PWG	Plasmonic Waveguide
Q	Quality Factor
RI	Refractive Index
RIE	Reaction Ion Etching
RIU	RI unit
RMG	Reflection MG
ROP	Ratio of Power
S	Sensitivity
SBTHSPPs	Symmetric BTHSPPs
Si	Silicon
SiO_2	Silica
SiWG	Silicon Waveguide
SM	Symmetric Mode
SMF	Single Mode Fiber
SNOM	Scanning Near-field Optical Microscope
SPPs	Surface Plasmon Polaritons
SPW	Surface Plasmon Wave
SRSPPs	Short Range SPPs
TE	Transverse Electric

TM	Transverse Magnetic
TMG	Transmission MG
TPMLF	Tapered Polarization Maintaining Lensed Fiber
TIR	Total Internal Reflection
VGHSPPs	V-Groove HSPPs
WHSPPs	Wedge HSPPs
WCSPPs	Waveguide Coupled SPPs
WG	Waveguide
WRR	Waveguide-Ring Resonator
2D	Two Dimensional
3D	Three Dimensional

Chapter 1: Introduction

1.1 Background

In an era of nanotechnology and ultrafast information processing, the Olympic motto ‘faster, higher, stronger’ might be phrased ‘faster, smaller, stronger’. ----- Mark Stockman [1].

The insatiable appetite for progressively faster information transport and processing capabilities has driven enormous progress in the photonics industry over the last two decades, resulting in a continuous development of photonic components that are faster, smaller (i.e. chip-scale) and stronger (i.e. more reliable) [2], to use the metaphor of the Olympic motto above. Smaller photonic components enable thousands of logic elements to be integrated into compact and lightweight processors, known as highly integrated photonic circuits (IPCs).

However, due to the diffraction limit, higher levels of miniaturization are very difficult to achieve for current photonic devices (i.e. the smallest device features are limited in size to about half a wavelength of light) [3]. One of the potential solutions to overcome the diffraction limit is to utilize so-called ‘surface plasmon polaritons’ (SPPs). At a metal-dielectric interface, SPPs originate from the strong coupling between electromagnetic waves and free electrons on the metal surface which propagate along the interface between the metal and dielectric, with a field strength that has a maximum intensity at the interface and which exponentially decays in both directions perpendicular to the interface [4]. Unlike dielectric waveguides, plasmonic waveguides are not restricted in size by the diffraction limit due to the subwavelength mode confinement of the SPPs mode, thus offering the potential to guide and manipulate light at a subwavelength scale. SPPs thus have the potential to be a key technology to underpin next generation high-density chip-scale photonic devices [5]. Subwavelength mode confinement

can also significantly enhance light-matter interactions which in turn offers fundamentally new solutions for biosensing [6], data storage [7] and spectroscopy [8].

However, currently plasmonic waveguides suffer the serious disadvantage of a very large propagation loss particularly when the mode confinement is at a subwavelength scale [9]. This fundamental limitation is inherent for all SPPs modes: stronger SPPs confinement pushes the field closer to the metal, which results in a larger metal power dissipation and thereby a shorter propagation length. Therefore a significant challenge is to design and develop novel plasmonic waveguide structures which allow for the realization of tight mode confinement whilst still offering a relatively low propagation loss.

SPPs are exceptionally sensitive to the dielectric properties near the metal surface because of their highly localized fields at the metal surface. This feature offers substantial potential for effective sensing applications. For example, a functionalized surface plasmon sensor reported in [10], utilized particular protein antibodies which were immobilized on the metal surface, so that the sensor was capable of monitoring a particular protein concentration and its binding behaviour when biological samples containing this particular protein antigen are introduced into the sensor. However current SPPs sensors have the disadvantage of relatively low sensitivity and also limitations in terms of the simultaneous measurement of multiple parameters [11]. High sensitivity combined with multi-parameter sensing to create platforms such as “lab-on-a-chip” or “lab-on-a-fiber” is seen by many as very desirable targets for sensor systems [12]. Therefore improving plasmon sensor’s sensitivity and also realizing simultaneous multiple parameter measurements, while it is challenging task, is a very worthwhile endeavour.

1.2 Objectives and Contributions

This thesis focuses on investigations of novel plasmonic waveguide devices and plasmonic sensors. The objectives of this research are three-fold: to develop a deeper understanding of SPPs based waveguides as a basis for the design of novel plasmonic devices which are essential for building highly integrated systems; to develop novel plasmonic waveguides to address the challenge of improving the propagation length while maintaining very tight mode confinement and finally to design new plasmonic biosensors to achieve high sensitivity and simultaneous measurements of multiple parameters. The following contributions are reported in this thesis.

a) A number of novel plasmonic waveguide devices for integrated photonic circuits are proposed and investigated numerically and experimentally, including an optical filter, a polarization beam splitter and a TE-pass polarizer. For example, the proposed TE-pass polarizer has been fabricated and experimentally demonstrated confirming the validity of the simulation results.

b) Several novel plasmonic waveguide designs are proposed with longer propagation lengths (~ 4000 μm vs. ~ 100 μm for a traditional SPPs waveguide) and tight mode confinement (mode area ~ λ^2/10000 vs. ~ λ^2/500 for a traditional SPPs waveguide). These specifications are better than those previously reported in the literature. For example, the proposed long range wedge-to-wedge hybrid SPPs (LRWWHSPPs) waveguide design offers a deep subwavelength mode confinement (mode area ranges from λ^2/10604 to λ^2/972) and a relatively long propagation length (ranges from 1680 μm to 4724 μm).

c) Two plasmonic based sensing structures are proposed and analyzed in detail. The proposed sensors are more sensitive than previously reported plasmonic sensors. More importantly,

the proposed subwavelength plasmonic grating based sensor is capable of simultaneous measurements of both the refractive index and the thickness of the analyte layer, and thus offers the potential for multiple parameter measurement in sensing applications.

1.3 Thesis organization

The thesis is organized as follows. Chapter 2 presents an overview of the theoretical fundamentals of SPPs, along with their two technologically important applications in light guiding and sensing. For light guiding, the dispersion relations for plasmonic modes supported by four popular waveguides: a metal-insulator-metal (MIM) waveguide, an insulator-metal-insulator (IMI) waveguide, a dielectric loaded SPPs (DLSPPs) waveguide and a hybrid SPPs (HSPPs) waveguide, are discussed and deduced from Maxwell's equations. Furthermore an introduction to plasmonic based sensing and its applications are presented. Finally, the two different numerical methods used in this thesis are briefly introduced, specifically the Finite-Difference Time-Domain (FDTD) method and the Finite Element Method (FEM).

Chapter 3 presents a detailed treatment of the theory of an SPPs mode supported by an MIM waveguide (SPPs_MIM) and a long range SPPs (LRSPPs) mode supported by an IMI waveguide. Based on the MIM and IMI configurations, designs for an ultra-compact MIM waveguide based Fabry-Perot filter and a compact IMI waveguide based polarization beam splitter are proposed and analyzed with the aim of developing basic building blocks for IPCs.

Chapter 4 presents a theoretical investigation of a long-range DLSPPs (LRDLSPPs) waveguide with the objective of improving its guiding performance in the context of the well-known tradeoff between the mode confinement and propagation length: that is to achieve a higher degree of mode confinement for the same propagation length or a longer propagation

length for the same mode confinement, compared to existing LRDLSPPs waveguides. This chapter also presents a novel low cost microfiber loaded SPPs (MFLSPPs) based TE-pass polarizer both in simulation and experiment. The fabrication, operating principle and measurements for the TE-pass polarizer are discussed in this chapter.

Chapter 5 further addresses the challenge of achieving both a long propagation length and tight mode confinement for a plasmonic waveguide. In doing so, two novel modified long range hybrid SPPs (LRHSPPs) waveguides are analyzed, respectively named a long range nanowedge HSPPs (LRWHSPPs) waveguide and long range wedge-to-wedge HSPPs (LRWWHSPPs) waveguide. A detailed optimization of the structural parameters and corresponding physical explanations is discussed in this chapter. Particularly for the LRWWHSPPs waveguide is shown that such a waveguide could achieve a better tradeoff compared to the most recently published structures.

Chapter 6 presents the studies of two novel SPPs based sensors. One structure is based on a multimode fiber coated with a metal grating structure, offering a higher sensitivity compared to a conventional multimode fiber sensor coated with uniform metal layer. Another structure is based on a reflection metal grating, demonstrating a capability for simultaneous measurement of refractive index and the thickness of the analyte layer.

Finally the conclusions arising from the research and a number of future research directions are presented in Chapter 7.

1.4 References

1. M. Stockman, Plasmonic lasers: on the fast track, *Nature Phys.*, 10, pp. 799-800, (2014).
2. R. Kirchain, and L. Kimerling, A roadmap for nanophotonics, *Nature Photon.*, 1, pp. 303-305, (2007).

3. M. Born, W. Emil, Principles of optics, Cambridge University Press (1997).

4. W. L. Barnes, A. Dereux, and T. W. Ebbesen, Surface plasmon subwavelength optics, *Nature*, 424, pp. 824-830, (2003).

5. R. Zia, J. A. Schuller, A. Chandran, M. L. Brongersma, Plasmonics: the next chip-scale technology, *Mater. Today*, 9, pp. 20-27, (2006).

6. A. G. Brolo, Plasmonic for future biosensors, *Nature Photon.*, 6, pp. 709-713, (2012).

7. D. O. Connor, and A. V. Zayats, Data storage: the third plasmonic revolution, *Nat. Nanotechnol.*, 5, pp. 482-483, (2010).

8. M. D. Sonntag, J. M. Klingsporn, A. B. Zrimsek, B. Sharma, L. K. Ruvuna, and R. P. Van Duyne, Molecular plasmonics for nanoscale spectroscopy, *Chem. Soc. Rev.*, 43, pp. 1230-1247, (2014).

9. T. W. Ebbesen, C. Genet, and S. I. Bozhevolnyi, Surface-plasmon circuitry, *Phys. Today*, 61, pp. 44-50, (2008).

10. J. Homola, Surface plasmon resonance based sensors, *Springer*, (2006).

11. S. A. Maier, Plasmonics: Fundamentals and Applications, (Springer, 2007).

12. G. Farrell, Optical Fiber Sensing: Sensing solutions from the macro world to the micro world, Invited talk, ICT2015 Conference, April 2015.

Chapter 2: Theoretical background and applications of Plasmonics

2.1 Introduction

Surface plasmon polaritons (SPPs) are electromagnetic waves coupled to collective electron oscillations and propagating along the interface between metal and dielectric media, exponentially decaying into both neighboring media. This chapter is devoted to illustrating the basic background to SPPs. As a starting point, section 2.2 firstly describes wave propagation using Maxwell's equations. Then the dispersion relation of SPPs at a single metal-dielectric interface is deduced, again from Maxwell's equations, in section 2.3. According to the dispersion relation, it is very difficult to excite SPPs where the excitation is normal to a flat metal-dielectric interface because of the wavevector mismatch between the injected light and SPPs. The main excitation methods for SPPs are discussed in section 2.3. Then two technologically important applications of SPPs in light guiding and sensing are discussed in section 2.4 and section 2.5, respectively, in each case supported by a brief review of research developments as presented in the literature. The chapter is concluded with a brief introduction to two numerical methods used in this thesis: the Finite-Difference Time-Domain (FDTD) method and Finite Element Method (FEM).

2.2 Maxwell's equations and wave propagation

Before investigating the physical properties of SPPs, the starting point is Maxwell's equations in the following form [1]:

$$\nabla \cdot \mathbf{D} = \rho \qquad (2.1a)$$

$$\nabla \cdot \mathbf{B} = 0 \qquad (2.1b)$$

$$\nabla \times \mathbf{E} = -\frac{\partial}{\partial t}\mathbf{B} \qquad (2.1c)$$

$$\nabla \times \mathbf{H} = \mathbf{j} + \frac{\partial}{\partial t}\mathbf{D} \qquad (2.1d)$$

where **E**, **H**, **D** and **B** represent the electric field, the magnetic field, the dielectric displacement and the magnetic flux density, respectively, ρ is the free charge density and **j** is the free current density. In optics it is usually assumed that the free charge and current are absent, i.e. ρ = 0 and **j** = 0.

In this thesis, only linear, isotropic and nonmagnetic media are considered, hence the relations between (**E**, **D**) and (**H, B**) can be defined as [1]:

$$\mathbf{D} = \varepsilon_0 \varepsilon \mathbf{E} \qquad (2.2a)$$

$$\mathbf{B} = \mu_0 \mu \mathbf{H} \qquad (2.2b)$$

where ε_0 ($\approx 8.854 \times 10^{-12}$ F/m) and μ_0 ($\approx 1.257 \times 10^{-6}$ H/m) are the permittivity and permeability of free space, respectively, ε and μ (=1, for a nonmagnetic medium) respectively represent the relative permittivity (or dielectric constant) and relative permeability of the medium.

Assuming a time-harmonic dependence for the electromagnetic (EM) field i.e. $e^{-i\omega t}$, then

$$\frac{\partial}{\partial t} = -i\omega \qquad (2.3)$$

where *i* is the imaginary unit, and ω is the angular frequency. Then eq. (2.1c) and eq. (2.1d) can be expanded in Cartesian coordinates as follows:

$$\begin{cases} \dfrac{\partial E_z}{\partial y} - \dfrac{\partial E_y}{\partial z} = i\omega\mu_0 H_x & (2.4a) \\ \dfrac{\partial E_x}{\partial z} - \dfrac{\partial E_z}{\partial x} = i\omega\mu_0 H_y & (2.4b) \\ \dfrac{\partial E_y}{\partial x} - \dfrac{\partial E_x}{\partial y} = i\omega\mu_0 H_z & (2.4c) \\ \dfrac{\partial H_z}{\partial y} - \dfrac{\partial H_y}{\partial z} = -i\omega\varepsilon_0\varepsilon E_x & (2.4d) \\ \dfrac{\partial H_x}{\partial z} - \dfrac{\partial H_z}{\partial x} = -i\omega\varepsilon_0\varepsilon E_y & (2.4e) \\ \dfrac{\partial H_y}{\partial x} - \dfrac{\partial H_x}{\partial y} = -i\omega\varepsilon_0\varepsilon E_z & (2.4f) \end{cases}$$

2.3 SPPs at a single metal-dielectric interface

As shown in Fig. 2.1, the simplest geometry sustaining SPPs is a single, flat interface between a metal ($z < 0$, with a complex dielectric constant ε_1, in which the real part is negative) and a dielectric ($z > 0$, with a positive dielectric constant ε_2). Specifically, assuming that the SPPs wave propagates along the x-direction with a wavevector β, then $\frac{\partial}{\partial x} = i\beta$, and that the structure is purely 2-dimensional, that is there is no spatial variation along the y-direction, then $\frac{\partial}{\partial y} = 0$ and so eq. (2.4) can be simplified as follows:

$$\begin{cases} \dfrac{\partial E_y}{\partial z} = -i\omega\mu_0 H_x & (2.5a) \\ \dfrac{\partial E_x}{\partial z} - i\beta E_z = i\omega\mu_0 H_y & (2.5b) \\ i\beta E_y = i\omega\mu_0 H_z & (2.5c) \\ \dfrac{\partial H_y}{\partial z} = i\omega\varepsilon_0\varepsilon E_x & (2.5d) \\ \dfrac{\partial H_x}{\partial z} - i\beta H_z = -i\omega\varepsilon_0\varepsilon E_y & (2.5e) \\ i\beta H_y = -i\omega\varepsilon_0\varepsilon E_z & (2.5f) \end{cases}$$

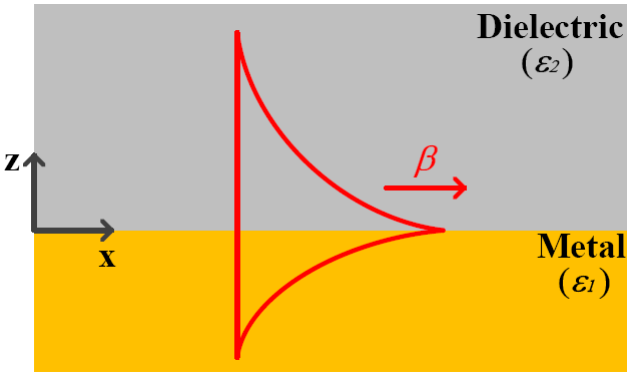

Fig 2.1. Schematic view of SPPs propagating along a single metal-dielectric interface in two dimensions.

It can be easily shown that the eq. (2.5) can be divided into two independent sets: (I) the transverse magnetic (TM) modes with only the field components E_x, E_z and H_y being nonzero; and (II) the transverse electric (TE) modes, where only the field components H_x, H_z and E_y are nonzero.

2.3.1 TM mode

For the TM mode, eq. (2.5) is reduced to:

$$\frac{\partial E_x}{\partial z} - i\beta E_z = i\omega\mu_0 H_y \qquad (2.6a)$$

$$E_x = -\frac{i}{\omega\varepsilon_0\varepsilon}\frac{\partial H_y}{\partial z} \qquad (2.6b)$$

$$E_z = -\frac{\beta}{\omega\varepsilon_0\varepsilon} H_y \qquad (2.6c)$$

The field components can be easily found from the solutions of eq. (2.6) and expressed as [2]:

for z < 0

$$H_y(z) = A_1 e^{i\beta x} e^{k_1 z} \qquad (2.7a)$$

$$E_x(z) = -\frac{iA_1 k_1}{\omega\varepsilon_0\varepsilon_1} e^{i\beta x} e^{k_1 z} \qquad (2.7b)$$

$$E_z(z) = -\frac{A_1\beta}{\omega\varepsilon_0\varepsilon_1} e^{i\beta x} e^{k_1 z} \qquad (2.7c)$$

for z > 0

$$H_y(z) = A_2 e^{i\beta x} e^{-k_2 z} \qquad (2.8a)$$

$$E_x(z) = \frac{iA_2 k_2}{\omega \varepsilon_0 \varepsilon_2} e^{i\beta x} e^{-k_2 z} \qquad (2.8b)$$

$$E_z(z) = -\frac{A_2 \beta}{\omega \varepsilon_0 \varepsilon_2} e^{i\beta x} e^{-k_2 z} \qquad (2.8c)$$

in which

$$k_i^2 = \beta^2 - k_0^2 \varepsilon_i \quad (i = 1, 2) \qquad (2.9)$$

The continuity of H_y and E_x at the boundary $z = 0$ results in

$$A_1 = A_2 \text{ and } k_1 \varepsilon_2 = -k_2 \varepsilon_1 \qquad (2.10)$$

Since the SPPs field is confined to the interface and evanescently decays in the *z*-direction, therefore the conditions Re $[k_1] > 0$ and Re $[k_2] > 0$ (for the convention of the signs in the exponents in eq. (2.7c, 2.8c)), demand that Re $[\varepsilon_1] < 0$ if $\varepsilon_2 > 0$. As it is known that for most metals and dielectrics this condition is satisfied in the visible and infrared wavelength range [3], the conclusion is that SPPs can exist for the TM polarization.

Combining eq. (2.9) and eq. (2.10), then the dispersion relation of SPPs at a single metal-dielectric interface is given by

$$\beta = k_0 \sqrt{\frac{\varepsilon_1 \varepsilon_2}{\varepsilon_1 + \varepsilon_2}} \qquad (2.11)$$

where $k_0 = \omega/c$ is the free-space wavevector and c is the speed of light in a vacuum. Eq. 2.11 will be discussed later but before that the possibility of SPPs for a TE polarization will be considered.

2.3.2 TE mode

For the TE mode, eq. (2.5) is reduced to:

$$\frac{\partial H_x}{\partial z} - i\beta H_z = -i\omega\varepsilon_0\varepsilon E_y \qquad (2.12a)$$

$$\frac{\partial E_y}{\partial z} = -i\omega\mu_0 H_x \qquad (2.12b)$$

$$i\beta E_y = i\omega\mu_0 H_z \qquad (2.12c)$$

The field components can be written as [2]:

for z < 0

$$E_y(z) = A_3 e^{i\beta x} e^{k_1 z} \qquad (2.13a)$$

$$H_x(z) = \frac{iA_3 k_1}{\omega\mu_0} e^{i\beta x} e^{k_1 z} \qquad (2.13b)$$

$$H_z(z) = \frac{A_3\beta}{\omega\mu_0} e^{i\beta x} e^{k_1 z} \qquad (2.13c)$$

for z > 0

$$E_y(z) = A_4 e^{i\beta x} e^{-k_2 z} \qquad (2.14a)$$

$$H_x(z) = -\frac{iA_4 k_2}{\omega\mu_0} e^{i\beta x} e^{-k_2 z} \qquad (2.14b)$$

$$H_z(z) = \frac{A_4\beta}{\omega\mu_0} e^{i\beta x} e^{-k_2 z} \qquad (2.14c)$$

The continuity of E_y and H_x at the boundary $z = 0$ results in

$$A_3 = A_4 \text{ and } k_1 = -k_2 \qquad (2.15)$$

One can see that eq. (2.15) does not satisfy the condition of Re [k_1] > 0 and Re [k_2] > 0 derived in the previous section. It can be concluded then that no SPPs can exist for the TE polarization.

2.3.3 Dispersion relation of SPPs

Now let us examine the properties of SPPs by considering the dispersion relation expressed by eq. (2.11). Fig 2.2 depicts plots of eq. (2.11) for SPPs at a single air-silver interface. The complex frequency-dependent permittivity of silver $\varepsilon_2(\omega)$ is characterized by the Drude model [4]:

$$\varepsilon_2(\omega) = \varepsilon_\infty - \frac{\omega_p^2}{\omega(\omega + i\gamma)} \qquad (2.16)$$

where ε_∞= 3.7, ω_p=1.38×10^{16} Hz and γ = 2.73×10^{13} Hz. From Fig. 2.2 it can be observed that the SPPs plot lies on the right side of the plot of the light in air which means that for a given frequency the wavevector of SPPs is always larger than that of the light in free space, i.e. $\beta > k_0$, thus the light cannot directly transform into SPPs due to this wavevector mismatch. Such a wavevector mismatch must be dealt with by way of the excitation method chosen if light is to be used to generate SPPs. This will be discussed in next section 2.3.4.

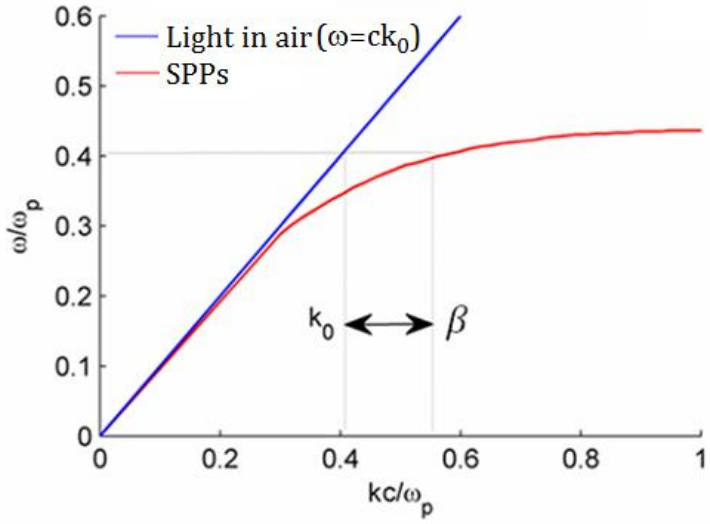

Fig. 2.2. Dispersion curves for SPPs at a single air-silver interface (the red solid line). The silver dispersion is described by the Drude model.

2.3.4 SPPs Excitation methods

As seen from Fig. 2.2, the generation of SPPs is restricted by the wavevector mismatch. Therefore special excitation techniques are required to deal with this wavevector mismatch, for example, prism coupling [5], grating coupling [6], near field excitation [7], and highly focused laser beam excitation [8]. In this section the two most popular techniques, prism coupling and grating coupling are presented.

2.3.4.1 Prism coupling---Kretschmann and Otto configurations

The excitation of SPPs using a prism is based on evanescent wave coupling mechanism. Fig. 2.3 shows two common geometries for prism coupling: (a) Kretschmann and (b) Otto configurations.

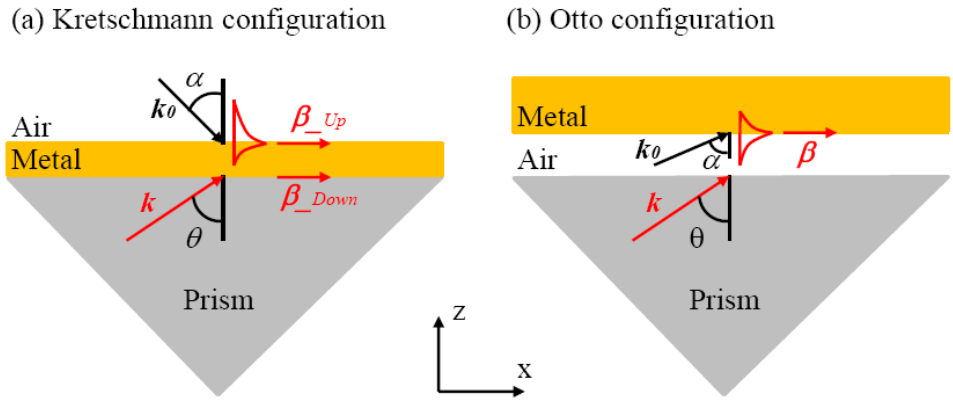

Fig. 2.3. Prism coupling to excite SPPs using the attenuated total internal reflection in the (a) Kretschmann and (b) Otto configurations.

For the Kretschmann configuration, as shown in Fig. 2.3 (a), a thin metal film is coated on the top of a glass prism with a dielectric constant of ε. SPPs at the metal-prism interface cannot be excited by the light beam with a wavevector k due to the wavevector mismatch between k and $\beta_{\_Down}$ i.e. $\beta_{\_Down} > k \geqslant k_x = k \sin\theta$. Similarly the SPPs at the metal-air interface cannot be directly excited by the light beam with a wavevector k_0 due to the fact that

$\beta_{\_Up} > k_0 \geqslant k_{0x} = k_0 \sin\alpha$. However it is easy to see that since k_x ($=k_{0x}\sqrt{\varepsilon}$) > k_{0x}, it is possible to achieve $k_x > k_0$ and then realize the phase match $k_x = \beta_{\_Up}$, indicating that it is possible to excite SPPs at the metal-air interface by a beam incident from the prism on to the metal at the metal-prism interface. Reflection takes place at the prism-metal interface and so-called Attenuated Total Reflection (ATR) [5] takes place when the incident angle θ is larger than the critical angle. However for ATR there exists an evanescent field which extends outside the prism [5]. Therefore if the thickness of the metal film is smaller than the decay length of the evanescent field, the evanescent field will penetrate through the metal film to excite the SPPs at the metal-air interface once the corresponding wavevectors are matched.

Another typical geometry is the Otto configuration (Fig. 2.3 (b)), in which the glass prism is separated from the metal film by a thin air gap. Similarly the SPPs at the metal-air interface cannot be directly excited due to the wavevector mismatch i.e. $\beta > k_0 \geqslant k_{0x} = k_0 \sin\alpha$. However, if ATR takes place at the prism-air interface, the induced evanescent field (with a wavevector of $k_x = k_{0x}\sqrt{\varepsilon} > k_{0x}$) can be coupled to the SPPs (with a wavevector of $\beta > k_{0x} = k_0 \sin\alpha$) at the metal-air interface via the wavevector matching i.e. $k_x = \beta$. It should be noted that in this case the width of the air gap should be smaller than the decay length of the evanescent field. Since the control of the air gap between the prism and metal film is difficult, the result is that the Otto configuration is not widely used in practice.

2.3.4.2 Grating coupling

The wavevector mismatch between SPPs and incident light can also be dealt with by using a metal grating. As an example, Fig. 2.4 depicts a one-dimensional metal grating with a period of T, where the surrounding dielectric is assumed as air. When the light is illuminated on the metal grating at an incident angle θ, the light will be diffracted by the grating. The

wavevector of the diffracted light will be superimposed on the incident light, and wavevector matching takes place if the condition [6]

$$\beta = k_0 sin\theta \pm \frac{2m\pi}{T} \qquad (2.17)$$

is fulfilled, where m is an integer (m = 1, 2, 3….) indicating the order of diffraction, and k_0 is the wavevector in the air. The incident light can be coupled to an SPPs mode when $2\pi m/T$ is equal to the wavevector mismatch. In addition, it should be noted that the reverse process can also take place: SPPs propagating at a metal-dielectric interface can be coupled to free space light and thus radiated by the grating [9].

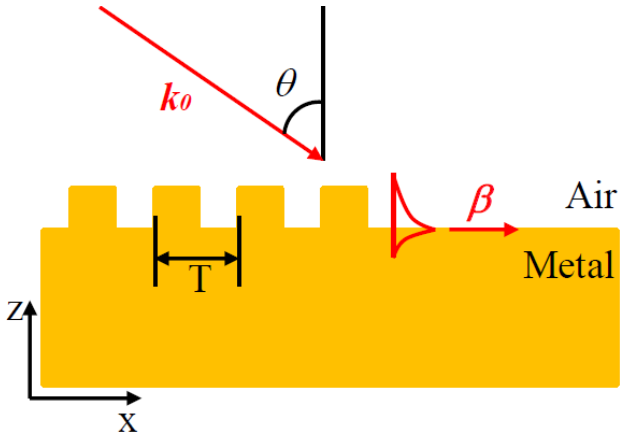

Fig. 2.4. Incident light to SPPs wavevector matching of using a metal grating.

2.4 SPPs waveguiding

Having described the basics of SPPs in section 2.3, in this section we continue to discuss the propagation properties of SPPs.

Two critical parameters that determine mode characteristics are the propagation length L_p and the normalized mode area A (i.e. a larger value of A corresponds to a lower degree mode confinement) and are defined as [10]

$$L_p = \lambda/[4\pi \mathrm{Im}(n_{\mathrm{eff}})] \qquad (2.18)$$

$$A = \frac{A_m}{A_0} = \frac{\iint_{-\infty}^{\infty} W(x,y)\mathrm{d}x\mathrm{d}y}{\max[W(x,y)]} \times \frac{1}{A_0} \qquad (2.19)$$

where λ is the operating wavelength, Im(n_{eff}) is the imaginary part of the mode effective refractive index n_{eff}, A_m is the mode area, $A_0 = \lambda^2/4$ is the diffraction limited mode area, and the energy density $W(x, y)$ is defined as

$$W(x,y) = \frac{1}{2}\,\mathrm{Re}\left\{\frac{d[\omega\varepsilon(x,y)]}{d\omega}\right\}|E(x,y)|^2 + \frac{1}{2}\mu_0|H(x,y)|^2 \qquad (2.20)$$

where $E(x, y)$ and $H(x,y)$ are the electric and magnetic fields, respectively.

Research on plasmonic waveguides dates back to the 1970s to 1980s [11-12]. In these early works, it was found that the SPPs waveguides can be used to localize guided modes beyond the diffraction limit. Later in 1997, J. Takahara et al firstly demonstrated the possibility of subdiffraction guiding of SPPs modes in a cylindrical metal nanowire or nanohole configuration [13]. However the subdiffraction guiding of SPPs (i.e. the subwavelength mode confinement) was achieved at the cost of a short propagation length [14]. Therefore from early 2000s, research interests started to focus on compromising the tradeoff between the mode confinement and propagation length. In early 2000s, two important plasmonic heterostructures were investigated, the insulator-metal-insulator (IMI) waveguide [15] and the metal-insulator-metal (MIM) [16] waveguide. The IMI waveguide can guide SPPs over distances of several centimeters, but the associated EM fields are weakly confined. While the MIM waveguide exhibits a subwavelength mode confinement, it has a large attenuation loss, leading to a propagation length that is only in the order of a micrometer or lower. In the years that followed various types of SPPs waveguides were proposed to mitigate this tradeoff, which included a metal wedge waveguide [17], a metal V-groove waveguide [18], and a dielectric loaded SPPs (DLSPPs) waveguide [19, 20]. It was found that the metal wedge and

V-groove waveguides can realize a subwavelength confinement and an acceptable propagation length up to tens of micrometers. While the DLSPPs waveguide possesses an increased propagation length (up to hundreds of micrometers) it does have a relatively larger mode area. The tradeoff remained challenging until 2008 when there was a proposal for a novel hybrid SPPs (HSPPs) waveguide by R. F. Oulton [10], which could simultaneously offer a subwavelength mode confinement and an extended propagation length up to hundreds of micrometers. This breakthrough research opened the way recently to a new range of SPPs based applications, such as a nanolaser [21, 22] and a nanotweezer [23].

In the sub-sections that follow, MIM, IMI, DLSPPs and HSPPs waveguide types will be discussed in more detail, due to their unique properties, such as the extremely strong mode confinement, the extremely long propagation length, compatibility with industrial photolithography techniques, and a significantly improved tradeoff, respectively.

2.4.1 Metal-Insulator-Metal waveguide

In this section, the properties of a metal-insulator-metal (MIM) waveguide are discussed. The MIM waveguide consists of a thin dielectric layer sandwiched between two metal claddings, as shown in Fig. 2.5 (a).

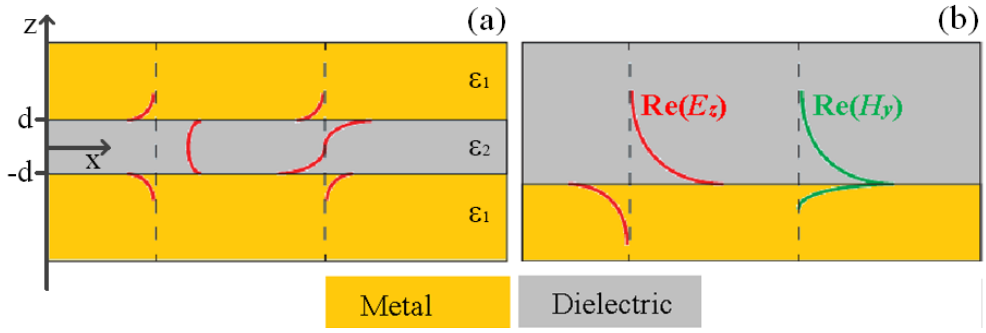

Fig. 2.5. Schematic views of (a) an MIM configuration and (b) a single metal-dielectric interface. The red lines denote Re(E_z), while the green lines represent Re(H_y).

As each metal-dielectric interface can sustain SPPs (Fig. 2.5 (b)), thus when the middle (dielectric) layer is thin enough, the interaction between the SPPs at the two metal surfaces gives rise to two coupled modes: a symmetric mode (SM) and an anti-symmetric mode (ASM), as depicted in Fig. 2.5 (a) [24].

In order to investigate the properties of the coupled modes for the MIM waveguide, it is assumed that SPPs propagate along the *x*-direction and there is no spatial variation along the *y*-direction. Similarly to the method described in section 2.3.1, the magnetic field (H_y) distributions are [2]:

$$H_y(z) = Ae^{i\beta x}e^{-k_2(z-d)} \quad (z > d) \qquad (2.21a)$$

$$H_y(z) = Be^{i\beta x}e^{k_2(z+d)} \quad (z < -d) \qquad (2.21b)$$

$$H_y(z) = Ce^{i\beta x}e^{k_1(z-d)} + De^{i\beta x}e^{-k_1(z+d)} \quad (-d < z < d) \qquad (2.21c)$$

and E_x (*z*) and E_z (*z*) are given by

$$E_x = -\frac{i}{\omega\varepsilon_0\varepsilon_i}\frac{\partial H_y}{\partial z} \qquad (2.22a)$$

$$E_z = -\frac{\beta}{\omega\varepsilon_0\varepsilon_i}H_y \qquad (2.22b)$$

in which

$$k_i^2 = \beta^2 - k_0^2\varepsilon_i \quad (i = 1, 2) \qquad (2.23)$$

According to the boundary conditions i.e. the continuity of H_y and E_x at the boundary $z = d$ and $z = -d$, the dispersion relations for the coupled modes can be expressed as [2]:

$$\text{SM:} \qquad \tanh k_1 d = -\frac{k_2\varepsilon_1}{k_1\varepsilon_2} \qquad (2.24a)$$

$$\text{ASM:} \qquad \tanh k_1 d = -\frac{k_1\varepsilon_2}{k_2\varepsilon_1} \qquad (2.24b)$$

For the fundamental ASM it is known that there is a cutoff thickness for the central dielectric layer which is equal to $\frac{\pi c}{\sqrt{\varepsilon_1}\omega}$ [25], while the fundamental SM does not exhibit the cutoff thickness for the central dielectric layer. In other words, the field of an SM can be confined into a central dielectric region with an arbitrarily small thickness, indicating it can provide a very high level of confinement ($A \sim \lambda^2/500$ was demonstrated in [20-21], which is far beyond the diffraction limit). However, this very strong mode confinement is achieved at the cost of a very short propagation length, typically in the order of a few micrometers ($L_p \sim 10$ μm [26]).

2.4.2 Insulator-Metal-Insulator waveguide

In addition to the MIM waveguide, there is another three-layer heterostructure: a thin metal layer sandwiched between two dielectric claddings, called the insulator-metal-insulator (IMI) waveguide, as shown in Fig. 2.6 (a). Similarly to the MIM waveguide, when the middle layer is thin enough, the interaction between the SPPs at the two metal surfaces gives rise to the coupled modes: SM and ASM.

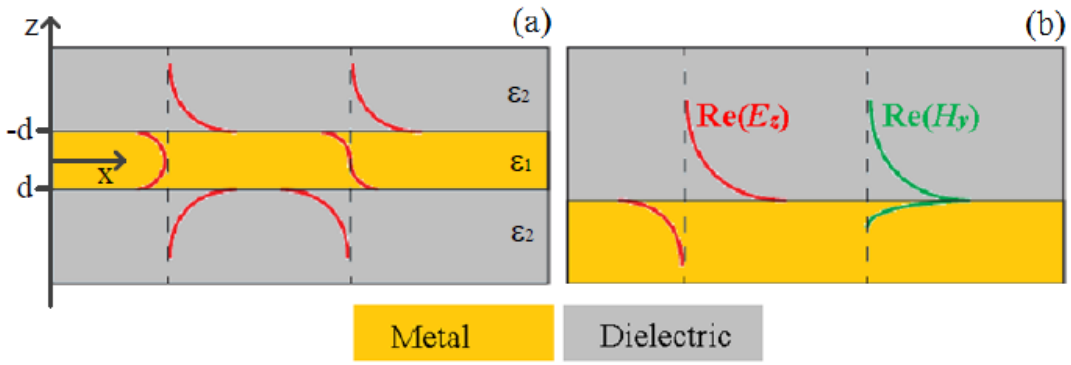

Fig. 2.6. Schematic views of (a) an IMI configuration and (b) a single metal-dielectric interface. The red lines denote Re(E_z), while the green lines represent Re(H_y).

The dispersion relations of the coupled modes for the IMI waveguide can be deduced in the same way as for the MIM waveguide and expressed by eq. (2.24). From the dispersion

relations, it is noted that the central metal layer has no cutoff thickness for both SM and ASM [15]. As the thickness of the central layer decreases, the confinement of the ASM close to the metal surface increases, giving rise to a reduction in the propagation length. While the SM exhibits the opposite behavior – the confinement of the SM decreases, the field spreads deeply into the dielectric medium, this implies a drastically increased propagation length. Therefore the SM for the IMI configuration is also referred to as the long range SPPs (LRSPPs) mode, which has attracted significant interest from researchers. The propagation length for the LRSPPs mode can be up to a few centimeters (L_p ~ 20 mm [15]), but this extended propagation length is accompanied by a very poor mode confinement (the mode area is comparable to that of the optical fiber mode [15]).

2.4.2 Dielectric loaded SPPs (DLSPPs) waveguide

A DLSPPs waveguide is one of the most popular plasmonic waveguides investigated in recent years. Fig. 2.7 shows a schematic view of the DLSPPs planar waveguide. Compared to a single planar dielectric-metal waveguide, a higher permittivity dielectric_1 layer is introduced in the DLSPPs waveguide, i.e. $\varepsilon_2 > \varepsilon_3$, with a thickness d.

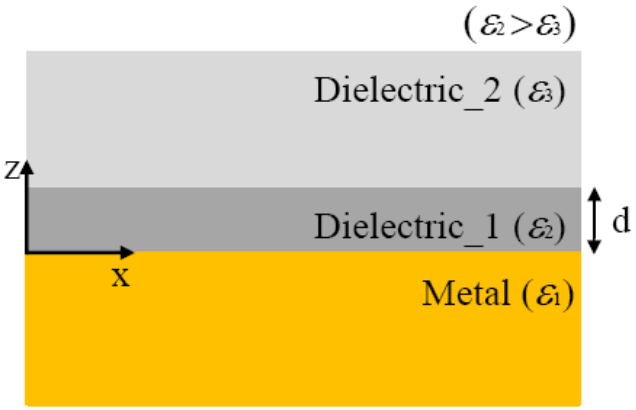

Fig. 2.7. Geometry of the 2D-DLSPPs waveguide with no permittivity variation along the y-direction.

To investigate the properties of the DLSPPs waveguide, it is assumed that SPPs propagate along the *x*-direction and there is no spatial variation along the *y*-direction. Then the magnetic field H_y can be expressed as follows [18]:

$$H_y(z) = Ae^{k_1 z}e^{i\beta x},\ z < 0 \qquad (2.25a)$$

$$H_y(z) = Be^{i\beta x}e^{k_2(z-d)} + Ce^{i\beta x}e^{-k_2 z},\ 0 < z < d \qquad (2.25b)$$

$$H_y(z) = De^{i\beta x}e^{k_3(z-d)},\ z > d \qquad (2.25c)$$

and $E_x(z)$ and $E_z(z)$ are given by eq. (2.22a) and eq. (2.22b), respectively, in which

$$k_i^2 = \beta^2 - k_0^2\varepsilon_i \quad (i = 1, 2, 3) \qquad (2.26)$$

By applying the boundary conditions, i.e. the continuity of H_y and E_x at the boundary $z = 0$ and $z = d$, the dispersion relation of the DLSPPs mode can be expressed as [18]:

$$tan\kappa d = \frac{\varepsilon_1\kappa(\varepsilon_2\theta + \varepsilon_3\gamma)}{\varepsilon_2\varepsilon_3\kappa^2 - \varepsilon_1^2\gamma\theta} \qquad (2.27)$$

where

$$\gamma = \sqrt{\beta^2 - k_0^2\varepsilon_2} \qquad (2.28)$$

$$\theta = \sqrt{\beta^2 - k_0^2\varepsilon_3} \qquad (2.29)$$

$$\kappa = \sqrt{k_0^2\varepsilon_1 - \beta^2} \qquad (2.30)$$

For the DLSPPs waveguide with a very thick dielectric_1 layer, it can be speculated that the DLSPPs mode is actually the SPPs mode propagating along the single dielectric_1-metal interface. As *d* decreases, the field of the DLSPPs mode will be progressively squeezed inside

the dielectric_1 region, indicating an enhanced mode confinement compared to that for the case of a very thick dielectric_1 layer. However a further decrease in d gives rise to a rapid increase in the field outside the dielectric_1, corresponding to a weaker mode confinement. This implies that there is an optimal value of d, at which the DLSPPs mode achieves the strongest mode confinement. It has been demonstrated that a DLSPPs waveguide can provide a modest mode confinement ($A \sim 0.16\lambda^2$) [19] as well as a relatively long propagation length ($L_p \sim 100$ μm) [19].

2.4.3 Hybrid SPPs (HSPPs) waveguide

The schematic diagram of a typical HSPPs waveguide is shown in Fig. 2.8. Compared to a DLSPPs waveguide, a lower permittivity dielectric_2 (ε_3, with a thickness of d) is sandwiched between the metal substrate and the higher permittivity dielectric_1 (ε_2, with a thickness of h).

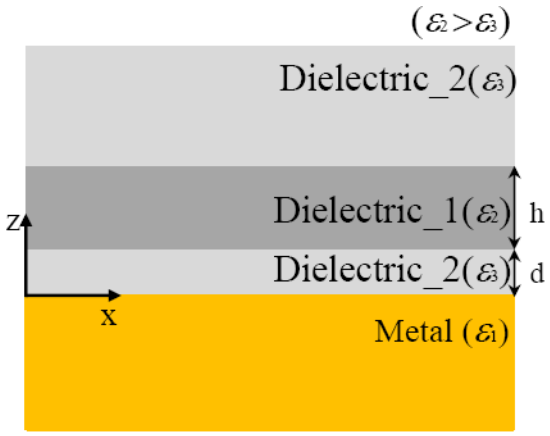

Fig. 2.8. Geometry of the HSPPs waveguide with no permittivity variation along the y-direction.

To investigate the properties of the HSPPs waveguide, it is assumed that SPPs propagate along the x-direction and there is no spatial variation along the y-direction. Then the magnetic field H_y can be expressed as follows [27]:

$$H_y(z) = Ae^{k_1 z}e^{i\beta x},\ z < 0 \qquad (2.31a)$$

$$H_y(z) = Be^{i\beta x}e^{k_2(z-d)} + Ce^{i\beta x}e^{-k_2 z},\ 0 < z < d \qquad (2.31b)$$

$$H_y(z) = De^{i\beta x}e^{k_3(z-d-h)} + Ee^{i\beta x}e^{-k_3(z-d)},\ d < z < (d+h) \qquad (2.31c)$$

$$H_y(z) = Fe^{i\beta x}e^{k_2(z-d-h)},\ z > (d+h) \qquad (2.31d)$$

and $E_x(z)$ and $E_z(z)$ are given by eq. (2.22a) and eq. (2.22b), respectively, in which

$$k_i^2 = \beta^2 - k_0^2\varepsilon_i \quad (i = 1, 2, 3) \qquad (2.32)$$

By applying the boundary conditions i.e. the continuity of H_y and E_x at the boundary $z = 0$, $z = d$, and $z = (d+h)$, the dispersion relation of the HSPPs mode can be expressed as [27]:

$$\frac{k_1}{\varepsilon_1}m_{11} + \frac{k_2}{\varepsilon_2}m_{22} - m_{21} - \frac{k_1 k_2}{\varepsilon_1\varepsilon_2}m_{12} = 0 \qquad (2.33)$$

where m_{11}, m_{12}, m_{21} and m_{22} are given by

$$\begin{bmatrix} m_{11} & m_{12} \\ m_{21} & m_{22} \end{bmatrix} = \begin{bmatrix} \cos(k_2 d) & -\frac{\varepsilon_2}{k_2}\sin(k_2 d) \\ \frac{k_2}{\varepsilon_2}\sin(k_2 d) & \cos(k_2 d) \end{bmatrix} \times \begin{bmatrix} \cos(k_3 h) & -\frac{\varepsilon_3}{k_3}\sin(k_3 h) \\ \frac{k_3}{\varepsilon_3}\sin(k_3 h) & \cos(k_3 h) \end{bmatrix} \qquad (2.34)$$

Eq. (2.33) can offer accurate solutions for the HSPPs mode; however, the physical explanation of the HSPPs mode from eq. (2.33) is not straightforward. The physical explanation can be provided by so-called coupled mode theory [20]. In this theory, it is believed that HSPPs mode is generated due to the coupling between the photonic waveguide mode (supported by the dielectric_1 layer) and the SPPs mode (excited at the single dielectric_2-metal interface). In other words, the dielectric_1 surrounded by the dielectric_2 can support a dielectric waveguide mode, and the dielectric_2-metal interface can support a SPPs mode. When the two modes with similar effective refractive indices are brought close

to each other, the dielectric waveguide mode will couple with the SPPs mode and form a HSPPs mode. Recently the HSPPs waveguide has attracted significant interest because it possesses a confinement capability beyond the diffraction limit ($A \sim \lambda^2/400$ [20]) while retaining a relatively long propagation length ($L_p \sim 150$ μm [20]).

Overall then, as discussed in the sub-sections above, a variety of SPPs waveguide types have been developed. Each has own strength and weakness, and still retains the fundamental tradeoff between the mode confinement and propagation length. The choice of SPPs guiding scheme should be selected by the requirements of specific applications.

2.5 SPPs sensing

In the last section 2.4 the potential applications of SPPs for waveguiding have been discussed. SPPs are highly confined to a metal surface, indicating they are very sensitive to a surrounding refractive index change near the metal surface. This property can be utilized to implement highly sensitive sensors. In this section sensing based on SPPs is discussed, starting with a brief review of SPPs sensing research developments over recent years.

SPPs based sensing was first performed experimentally by C. Nylander et al. in 1983 [28]. In that work the sensor is based on the Kretschmann configuration (Fig. 2.3 (a)). Later prism coupled SPPs for label-free[1] and real-time biosensing applications in medical diagnosis [29], life science diagnostics [30], and food industry detection [31] were proposed over the period up to early 2000s. However, these sensors inherently have the disadvantages of a bulky size, which means they are not suitable for miniaturization and integration. Nanoplasmonic biosensors did not flourish until recent dramatic progress in micro- and nano-fabrication techniques [32] occurred, starting in 2004. Various metal nanostructures such as

[1] Label free bio-sensing is a form of sensing that does not require the use of a molecular label (e.g. a fluorophore chemically attached to an analyte) as a means to aid in the detection of a target analyte.

subwavelength gratings [33], nanohole arrays [34], and nanoparticles [35] have been applied in plasmonic sensing. Compared to prism coupled plasmonic biosensors, nanoplasmonic biosensors offer the potential to construct highly integrated on-chip sensing platforms, for example the nanoplasmonic biosensor that reported recently in [36].

Fig. 2.9 (a) shows a typical configuration for a SPPs biosensor, which is based on the Kretschmann configuration, operating via either angular interrogation (the incident wavelength is fixed while the incident angle is scanned) [37] or wavelength interrogation (the incident angle is fixed while the incident wavelength is scanned) [38]. The TM-polarized light source provides a light beam to excite SPPs, and the reflected light is detected and analyzed by a demodulator.

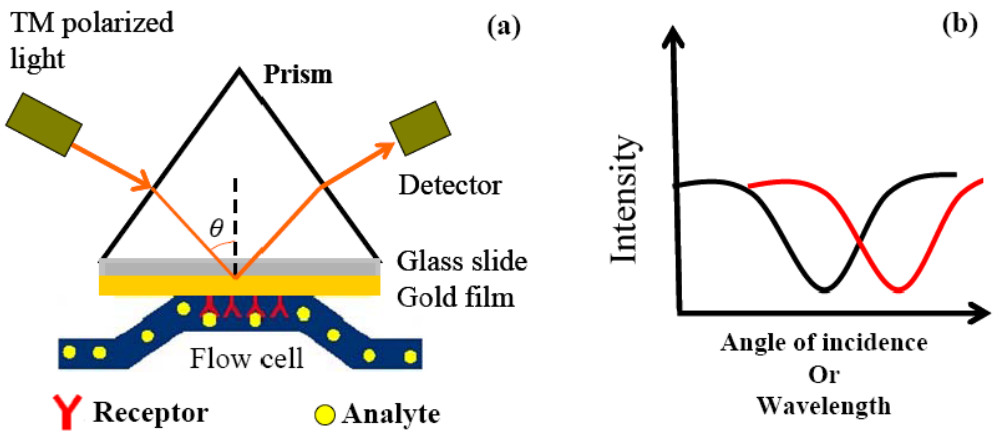

Fig. 2.9. (a) Typical setup for a SPPs based biosensor. (b) Reflected spectra of the biosensor, in which, the black line represents the spectrum before the analyte is attached to the receptor, while the red line is the spectrum after the analyte is attached.

As shown in Fig. 2.9 (a), the binding receptors are immobilized on the metal surface, and the biological analytes solution is allowed to flow through the flow cell which is in contact with the metal surface. When the analytes are captured by the receptors, the refractive index in proximity to the metal surface will change, causing a change in the effective refractive index

of the SPPs mode, which in turn will change the position of the reflection dip as shown in Fig. 2.9 (b). This binding event can be detected by measuring the dip spectrum shift or reflection intensity variation.

In general, two parameters are introduced to evaluate a biosensor's performance: the sensitivity (*S*) and quality factor (*Q*) of the dip. As an example the use of wavelength interrogation is considered here to illustrate the definition of *S* and *Q*.

The sensitivity largely depends on the plasmonic structure, thus an appropriate design for the structure results in a high value of *S*, which can be related to the observed shift of in the resonance wavelength ($\delta\lambda_R$) per refractive index unit (RIU):

$$S = \frac{\delta\lambda_R}{\delta n} \qquad (2.35)$$

where δn is the refractive index variation of the sensing sample.

Another parameter is the quality factor (Q factor), which is determined by the 3 dB bandwidth of the resonance dip ($\Delta\lambda$). As the Q factor also depends on the resonant wavelength (λ_R), the Q factor is defined by the ratio of the resonant wavelength and 3dB bandwidth:

$$Q = \frac{\lambda_R}{\Delta\lambda} \qquad (2.36)$$

High *Q* values are desirable because in the presence of inevitable detector noise, a sharper dip (higher Q) will allow for the measurement of smaller spectral shifts with increased accuracy.

In later chapters of this thesis, sensing using SPPs will be considered in more detail.

2.6 Modeling techniques

Although the basics for SPPs are well established, SPPs based structures in reality are complex. As a result it is frequently not possible to achieve analytical solutions that characterize the operation of a device; therefore the numerical modeling becomes an essential tool to analyze and gain insights into the operation of such structures. Many numerical methods have been developed, such as Finite-Difference Time-Domain (FDTD) [39], Finite Element Method (FEM) [40], Method of Moment (MoM) [41], Beam propagation method (BPM) [42] etc. Due to the known limitations in accuracy achievable using MoM and BPM [41-42], when modeling discrete structures such as gratings with sharp structural transitions, in this thesis the numerical models have been primarily based on FDTD and FEM.

2.6.1 Finite-Difference Time-Domain Method

The FDTD method was firstly developed by Kane Yee in 1996 [39] to solve electromagnetic problems. It can be explained based on the Yee cell, as shown in Fig. 2.10, which is in the shape of a cubic cell in a Cartesian system.

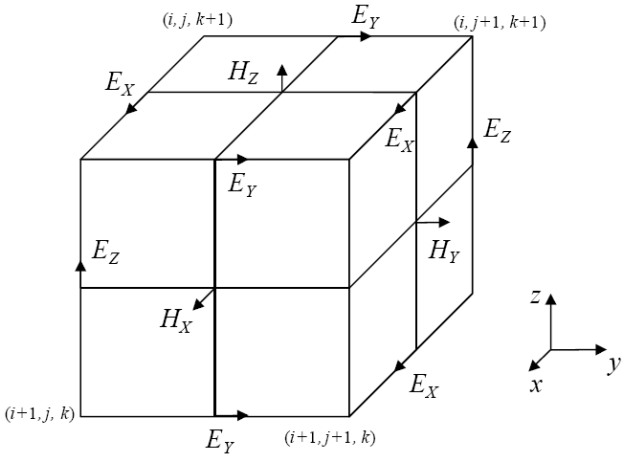

Fig. 2.10. Distribution of electric and magnetic field components in a Yee cell [39].

During the simulation, the whole space of interest will be divided into multiple Yee cells, and each cell is neighbored to 6 other similar cells. Based on the Yee cell, a central difference approximation can be used to discretize Maxwell's equations ((2.1c) and (2.1d)) both in space ($\triangle x$, $\triangle y$ and$\triangle z$) and time ($\triangle t$) [39]. As an example, consider the point (i, j, k) in space and t in time, electric filed E_x takes the following form

$$E_x|_{i,j,k}^{t+1/2} = \frac{\Delta t}{\varepsilon_{i,j,k}}\left[\frac{H_z|_{i,j+1/2,k}^{t} - H_z|_{i,j-1/2,k}^{t}}{\Delta y} - \frac{H_y|_{i,j,k+1/2}^{t} - H_y|_{i,j,k-1/2}^{t}}{\Delta z}\right] + E_x|_{i,j,k}^{t-1/2} \qquad (2.37)$$

The same method is then applied to the equations for other field components. Using these discretized equations, the field distribution in the entire calculation space can be determined for every point in time.

To avoid divergence in the simulation, the space and time intervals must satisfy the following so called "courant condition" [39]

$$\Delta t\sqrt{\left(\frac{1}{\Delta x}\right)^2 + \left(\frac{1}{\Delta y}\right)^2 + \left(\frac{1}{\Delta z}\right)^2} \leq \frac{1}{c} \qquad (2.38)$$

2.6.2 Finite Element Method

Another commonly used numerical method is FEM, which is fundamentally different from FDTD [40]. Instead of finding the solution that satisfies Maxwell's equations in FDTD, the simulation domain in FEM is partitioned into a number of subdomains called elements, the solution in each element is approximated as the basis function [40], and the final result can be obtained by summarizing the results from each elements.

As an example here take a two-dimensional Poisson problem with the function u (x, y) to introduce the principles of FEM. The function u (x, y) satisfies that

$$\begin{cases} -\nabla^2 u(x,y) = f(x,y) & \text{in } \Omega \\ u(x,y) = 0 & \text{in } \partial\Omega \end{cases} \qquad (2.39)$$

where Ω is the simulation domain, and $\partial\Omega$ is the boundary of Ω. By introducing a function *v* (*x*, *y*) which satisfies the boundary condition, we then have integral equation as follows:

$$\int_\Omega -(\nabla^2 u - f)v ds = \int_\Omega \nabla u \cdot \nabla v ds + \int_\Omega f v ds - \oint_{\partial\Omega} \nabla u \cdot v ds = 0 \qquad (2.40)$$

As *v*= 0 at $\partial\Omega$, then eq. (2.40) can be deduced to

$$\int_\Omega f v ds = -\int_\Omega \nabla u \cdot \nabla v ds = -\emptyset(u,v) \qquad (2.41)$$

which is the weak form of eq. (2.39).

In addition, the function *u* (*x*, *y*) can be expressed in the discretized form

$$u(x,y) = \sum_{i=1}^{n} u_i(x,y) v_i(x,y) \qquad (2.42)$$

where *n* is the total number of the elements. Then eq. (2.41) becomes

$$-\sum_{i=1}^{n} u_i \emptyset(v_{i,} v_j) = \int_\Omega f v_j ds\,, \quad j = 1,2,\dots,n \qquad (2.43)$$

which can be expressed in a matrix form by

$$-\mathbf{K}\vec{u} = \vec{f} \qquad (2.44)$$

where $\vec{u} = (u_1, u_{2,} \dots, u_n)^T$, $\vec{f} = (f_{1,} f_2, \dots, f_n)^T$ and **K** = [$K_{i,j}$] with $K_{i,j} = \emptyset(v_{i,} v_j)$.

Compared to FDTD, one of the main merits of FEM is that there are no restrictions on the shape of the elements, which can have arbitrary shapes such as triangles, tetrahedral, and polygons. Due to the better element flexibility to match the geometry, FEM outperforms FDTD for the analysis of complex structures [40].

2.7 Summary

This chapter has discussed the theoretical background and applications of SPPs. Section 2.2 has described Maxwell's equations and wave propagation; Section 2.3 has presented the dispersion relation and excitation methods for SPPs. In sections 2.4 and 2.5, plasmonic applications have been discussed, such as waveguiding and sensing. Finally the numerical modeling methods (FDTD and FEM) used in this work have been presented in section 2.6.

2.8 References

1. D. J. Griffiths, Introduction to electrodynamics, (Prentice Hall, New Jersey, 1999).
2. S. A. Maier, Plasmonics: Fundamentals and Applications, (Springer, 2007).
3. E. D. Palik, Handbook of optical constants, (Academic New York, 1985).
4. N. W. Ashcroft, and N. D. Mermin, Solid State Physics, (Brooks Cole, 1976).
5. L. Novotny, and B. Hecht, Principles of nano-optics, (Cambridge University Press, 2006).
6. I. R. Hooper, and J. R. Sambles, Dispersion of surface Plasmon polaritons on short-pitch metal gratings, *Phys. Rev. B*, 65, pp. 165432, (2002).
7. B. Hecht, H. Bielefeldt, L. Novotny, Y. Inouye, and D. W. Pohl, Local excitation, scattering, and interference of surface plasmons, *Phys. Rev. Lett.*, 77, pp. 1889, (1996).
8. H. Kano, S. Mizuguchi, and S. Kawata, Excitation of surface-plasmon polaritons by a focused laser beam, *JOSA. B*, 15, pp. 1381-1386, (1998).
9. S. Park, G. Lee, S. H. Song, C. H. Oh, and P. S. Kim, Resonant coupling of surface plasmons to radiation modes by use of dielectric gratings, *Opt. Lett.*, 28, pp. 1870-1872, (2003).
10. R. F. Oulton, V. J. Sorger, D. A. Genov, D. F. P. Pile, and X. Zhang, A hybrid plasmonic waveguide for subwavelength confinement and long-range propagation, *Nat.Photonics*, 2

(8), pp. 496-500, (2008).

11. E. N. Economou, Surface plasmons in thin films, *Phys. Rev.*, 182, pp. 539-554, (1969).

12. J. J. Burke, G. I. Stegeman, and T. Tamir, Surface-polariton-like waves guided by thin, lossy metal films, *Phys. Rev. B*, 33, pp. 5186-5201, (1986).

13. J. Takahara, S. Yamagishi, H. Taki, A. Morimoto, and T. Kobayashi, Guiding of a one-dimensional optical beam with nanometer diameter, *Opt. Lett.*, 22, pp. 475-477, (1997).

14. F. Forstmann, and R. R. Gerhardts, Metal optics near the plasma frequency, Springer Tracts in Modern Physics, 109Springer-verlag, pp. 132, New York (1986).

15. G. Veronis, and S. Fan, Guided subwavelength plasmonic mode supported by a slot in a thin metal film, *Opt. Lett.*, 30, pp. 3359-3361, (2005).

16. P. Berini, Plasmon-polariton modes guided by a metal film of finite width bounded by different dielectrics, *Opt. Express*, 7, pp. 329-335, (2000).

17. D. F. P. Pile, T. Ogawa, D. K. Gramotnev, T. Okamoto, M. Haraguchi, M. Fukui, and S. Matsuo, Theoretical and experimental investigation of strongly localized plasmons on triangular metal wedges for subwavelength waveguiding, *Appl. Phys. Lett.*, 87, pp. 061106, (2005).

18. D. K. Gramotnev, and D. F. P. Pile, Single-mode subwavelength waveguide with channel plasmon-polaritons in triangular grooves on a metal surface, *Appl. Phys. Lett.*, 85, pp. 6323, (2004).

19. X. Y. He, Q. J. Wang, and S. F. Yu, Analysis of dielectric loaded surface plasmon waveguide structures: transfer matrix method for plasmonic devices, *J. Appl. Phys.*, 111, pp. 073108, (2012).

20. T. Holmagaard, and S. I. Bozhevolnyi, Theoretical analysis of dielectric-loaded surface plasmon-polariton waveguides, *Phys. Rev. B.*, 75, pp. 245405, (2007).
21. R. F. Oulton, V. J. Sorger, T. Zentgraf, R. M. Ma, C. Gladden, L. Dai, G. Bartal, and X. Zhang, Plasmon lasers at deep subwavelength scale, *Nature*, 461, pp. 629-632, (2009).
22. R. M. Ma, R. F. Oulton, V. J. Sorger, and X. Zhang, Plasmon lasers: coherent light source at molecular scales, *Laser Photon. Rev.*, 7, pp. 1-21, (2013).
23. X. D. Yang, Y. M. Liu, R. F. Oulton, X. B. Yin, and X. Zhang, Optical forces in hybrid plasmonic waveguides, *Nano Lett.*, 11, pp. 321-328, (2011).
24. S. E. Kocabas, G. Veronis, D. A. B. Miller, and S. H. Fan, Modal analysis and coupling in metal-insulator-metal waveguides, *Phys. Rev. B.*, 79, pp. 035120, (2009).
25. J. Dionne, L. Sweatlock, H. Atwater, and A. Polman, Plasmon slot waveguides: Towards chip-scale propagation with subwavelength-sclae localization, Phys. Rev. B., 73, pp. 035407, (2006).
26. G. Veronis, and S. Fan, Guided subwavelength plasmonic mode supported by a slot in a thin metal film, *Opt. Lett.*, 30, pp. 3359-3361, (2005).
27. M. Z. Alam, J. S. Aitchison, and M. Mojahedi, Theoretical analysis of hybrid plasmonic waveguide, IEEE J. Sel. Top. Quantum Electron., 19, pp. 4602008, (2013).
28. C. Nylander, B. Liedberg, and L. Tommy, Gas detection by means of surface plasmon resonance, *Sens. Actuat*., 3, pp. 79-88, (1983).
29. J. Homola, Present and future of surface plasmon resonance biosensors, *Anal. Bioanal. Chem.*, 377, pp. 528-539, (2003).
30. R. Karlsson, SPR for molecular interaction analysis: a review of emerging application areas, *J. Mol. Recogn*., 17, pp. 151-161, (2004).
31. L. D. Mello, and L. T. Kubota, Review of the use of biosensors as analytical tools in the food and drink industries, *Food Chem*., 77, pp. 237-256, (2002).

32. T. Vo-Dinh, Biosensors, nanosensors and biochips: frontiers in environmental and medical diagnositics, *in Proceedings of the 1st International Symposium on Micro & Nano Technology*, pp. 14-17, (2004).
33. K. L. Lee, W. S. Wang, and P. K. Wei, Sensitive lable-free biosensors by using gap plasmons in gold nanoslits, *Biosens and Bioelectron*., 24, pp. 201-215, (2008).
34. T. Sannomiya, C. Hafner, and J. Voros, In situ sensing of single binding events by localized surface plasmon resonance, *Nano Lett*., 8, pp. 3450-3455, (2008).
35. F. Eftekhari, C. Escobedo, J. Ferreira, X. Duan, E. M. Girotto, A. G. Brolo, R. Gordon, and D. Sinton, Nanoholes as nanochennels: flow-through plasmonic sensing, *Anal. Chem*., 81, pp. 4308-4311, (2009).
36. A. G. Brolo, Plasmonic for future biosensors, *Nature Photon.*, 6, pp. 709-713, (2012).
37. J. Dostalek, A. Kasry, and W. G. Knoll, Long range surface plasmons for observation of biomolecular binding events at metallic surfaces, Plasmonic, 2, pp. 97-106, (2007).
38. A. Shalabney, and I. Abdulhalim, Figure-of-merit enhancement of surface plasmon resonance sensors in the spectral interrogation, *Opt. Lett.*, 37, pp. 1175-1177, (2012).
39. K. Yee, Numerical solution of initial boundary value problems involving Maxwell's equations in isotropic media, *Antennas and Propagation, IEEE Trans. on*, 14, pp. 302-307, (1966).
40. J. Jing, The Finite Element Method in Electromagnetics, (2nd Ed. New York: Wiley, 2002).
41. M. M. Ney. Method of moments as applied to electromagnetic problems. IEEE Trans. Microwave theory Tech., 33, pp. 972–980, (1985).
42. J. V. Roey, J. V. D. Donk, and P. E. Lagasse, Beam-propagation method: analysis and assessment, *J. Opt. Soc. Am*., 71, pp. 803-810, (1981).

Chapter 3: MIM/IMI plasmonic heterostructure based waveguide devices

3.1 Introduction

In Chapter 2 it was shown that the SPPs mode supported by an MIM configuration (SPPs_MIM) could provide mode confinement in the order of a subwavelength. In general, this enhanced confinement is achieved primarily by decreasing the SPPs spatial extent into the dielectric, thereby increasing the portion of SPPs power being absorbed by the metal. Therefore the propagation length for SPPs_MIM is relatively short, in the order of a few micrometers. On the other hand, in Chapter 2 another sandwiched heterostructure was also introduced, the IMI configuration, which supports the well-known LRSPPs mode. The LRSPPs mode has a relatively long propagation length, but it is not as useful for the purpose of subwavelength mode confinement.

This chapter presents a more detailed treatment of the theory of SPPs_MIM and LRSPPs modes. Based on this, two novel MIM and IMI based waveguide structures are considered along with their applications as an optical filter and polarization beam splitter (PBS).

3.2 Plasmonic MIM waveguide filters with nanocavity resonators

Optical filters have attracted tremendous interest in optical communication systems. With the exponential growth of information technology, highly integrated optical filters are required to address the twin challenges of miniaturization and high bit rate data communications. Traditional optical filters are based on dielectric only waveguides, which have dimensions comparable to the optical wavelength due to the inevitable diffraction limit. The resultant

large device sizes limit their applications in photonic integrated circuits. However, a MIM based structure is capable of overcoming such a diffraction limit and thus provides a potential solution. Recently several MIM based band pass or band stop filters have been proposed, such as Bragg reflectors [1], disk resonator filters [2], and multi-disk-shaped nanocavity filters [3]. Most of these structures provide a satisfactory performance, but they suffer from relatively large size and high transmission loss.

To overcome these disadvantages, a novel design for a compact optical filter based on strip nanocavity resonators embedded within a MIM waveguide is proposed. A schematic diagram of the filter is shown in Fig. 3.1. All the parameters of the structure are depicted in the figure. For the proposed filter, the refractive index of the insulator is assumed to be 1.45, and the frequency-dependent complex permittivity of gold $\varepsilon_m(\omega)$ is characterized by the Drude model. A TM-polarized light source is assumed to illuminate the structure, in a direction normal to the MIM waveguide.

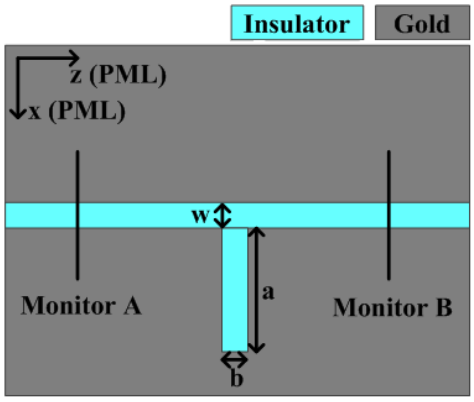

Fig. 3.1. Schematic structure of a cavity filter based on an MIM waveguide with one nanocavity resonator.

A two dimensional FDTD method is utilized with a perfect matched layer (PML) absorbing boundary condition. Based on this model, a combination of FORTRAN programming code and MATLAB is employed to investigate the transmission spectra of the proposed structure. This software combination is used as it allows the device simulation to run very efficiently and quickly in FORTRAN but with the data extraction and visualization strengths of

MATLAB. Two time monitors are located at A and B in Fig. 3.1 to detect the incident power and transmitted power, respectively, and a fast Fourier transformation (FFT) is used to obtain their frequency domain version. The spatial step sizes of the FDTD cell in the x- and z-directions are set as $\delta x = \delta z =$ 1 nm and the time step is chosen to be $\delta t = \delta x/2c$.

3.2.1 Design of a single-dip filter

Firstly, an MIM waveguide with only one nanocavity, as shown in Fig. 3.1, is investigated to realize the function of a single dip filter. In the simulation, the structural parameters of the nanocavity are set as w=100 nm, a=500 nm and b=50 nm. The nanocavity is positioned 1000 nm from both the input and output waveguide ports. The calculated transmission spectrum of the filter is shown in Fig. 3.2 (a). From Fig. 3.2 (a) one can see that a strong resonance appears at a wavelength around 877.2 nm with a high transmission dip, which is a typical characteristic of a notch filter. The quality factor (Q) of the SPPs nanocavity can be approximately calculated as a ratio between the central wavelength and the full width at half maximum at the resonance wavelength, so in this case the Q value is equal to 24.4. The quality factor is modest due to the fast decay of the power coupled from the nanocavity to the MIM waveguide, as well as the intrinsic absorption in the metal nanocavity. To further verify the above result, the normalized electromagnetic two dimensional (2D) field H_y patterns of the structure at wavelengths of 1100 nm and 877.2 nm are investigated in the whole FDTD space and summarized in Fig. 3.2 (b) and (c), respectively. From Fig. 3.2 (b) we can see that if the incident wavelength is far from the resonant wavelength, the light is mainly guided through the MIM waveguide and is weakly affected by the presence of the nanocavity. However, when the incident wavelength is equal to the resonant wavelength of 877.2 nm as shown in Fig. 3.2 (c), the light is trapped by the nanocavity and hence cannot be transmitted

to the output port. The results are consistent with the nature of the transmission spectrum shown in Fig. 3.2 (a).

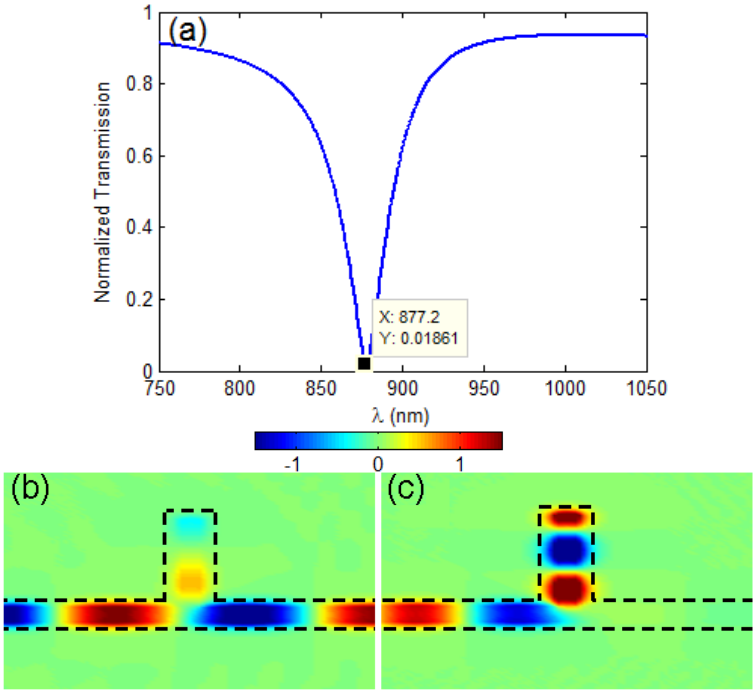

Fig. 3.2. (a) Transmission spectrum of the proposed structure with one nanocavity. Contour profiles of the average field H_y at different wavelengths of (b) λ=1100 *nm* and (c) λ=877.2 *nm*.

As is clearly shown in Fig. 3.2 (c), the nanocavity functions as a rectangular cavity resonator, with standing waves formed and trapped in the nanocavity under the resonance conditions which cause the near zero transmission to the output of the MIM waveguide. In order to better understand the physical mechanisms behind the operation of the wavelength filter based on the proposed structure, the characteristics of SPPs propagating in the structure are examined. When SPPs propagating along the MIM waveguide reach the nanocavity, they will be coupled into the nanocavity and converted into the forward and backward standing waves due to the multiple reflections at the air-metal interface. The phase delay of one round-trip in the nanocavity $\Delta\phi$ can be defined as [4]: $\Delta\phi=4\pi n_{eff}a/\lambda+\phi_{del}$, where n_{eff} is the real part of the effective refractive index of the waveguide mode in the nanocavity and ϕ_{del} is the total phase

shift of SPPs in reflection at the air-metal interface, which can be neglected when b/λ is very small [5]. The stable standing waves will only be formed inside the nanocavity for phase delay values corresponding to odd integer multiples of π, which can be expressed as: $\Delta\phi=(2m-1)\pi$. Here m is the positive integer which corresponds to the number of the antinodes of the standing wave in the nanocavity. In this way we can obtain the destructive resonance wavelength as:

$$\lambda=4n_{eff}a/[(2m-1)] \qquad (3.1)$$

Here we consider only the symmetric fundamental TM waveguide mode since the width b of the insulator waveguide in the nanocavity is much smaller than the incident wavelength, whose dispersion relation in the 2D-MIM waveguide is given by [4]

$$\varepsilon_d k_m + \varepsilon_m k_d \coth(-2ibk_d/2) = 0 \qquad (3.2)$$

$$k_d = k_0\sqrt{\varepsilon_d - n_{eff}^2} \text{ and } k_m = k_0\sqrt{\varepsilon_m - n_{eff}^2} \qquad (3.3)$$

where ε_d and ε_m represent the dielectric constants of the insulator and metal, respectively, and $k_0=2\pi/\lambda$ is the free space wavevector. Fig. 3.3 (a-b) shows the contour plots of the real/imaginary part of the effective refractive indices (Real(n_{eff})/Imag(n_{eff})) vs. the wavelength and width b. From Fig. 3.3 (a), it is found that at a particular wavelength, as b increases the Real(n_{eff}) decreases. However there is no significant influence on Real(n_{eff}) from wavelength at a particular width b, which is similar to the results found for structures in the terahertz regime [6]. This could possibly be due to the fact that when λ >800 nm, the penetration depth of SPPs in the metal [7] is only slightly influenced by the wavelength. Fig. 3.3 (b) shows that at all wavelengths ranging from 500 nm to 1800 nm, as b increases, the Imag(n_{eff}) decreases and hence transmission loss within the metal decreases. By solving Eqs. (3.1) to (3.3) directly, the destructive resonance wavelength is calculated to be 868.9 nm, which is close to the value

of 877.2 nm obtained by the FDTD algorithms. The small deviation can be partly attributed to neglecting the total phase shift of SPPs in reflection at the air-metal interface ϕ_{del}.

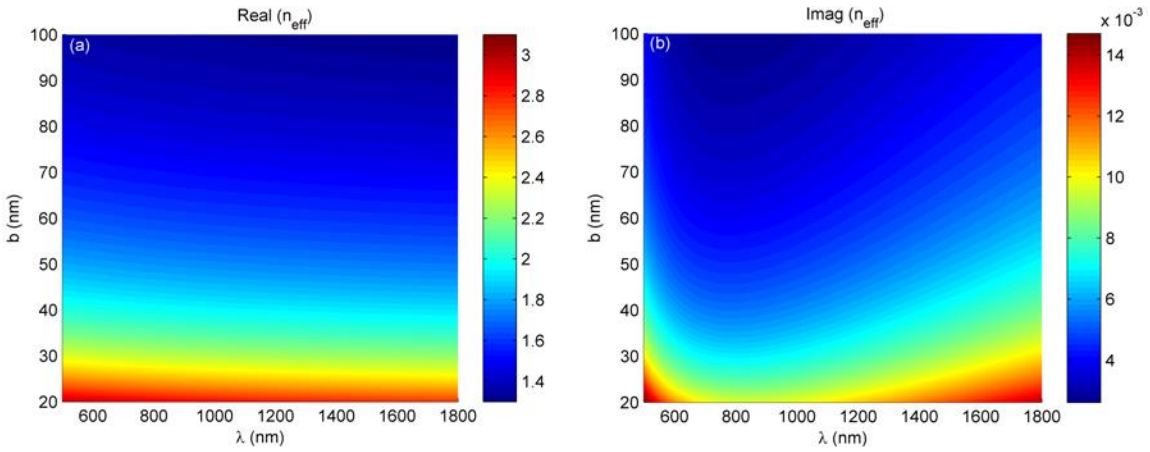

Fig. 3.3. Surface plot of the (a) real and (b) imaginary parts of effective refractive indices versus the width of the nanocavity at different wavelengths.

Based on the theoretical results above, it is obvious that the length *a* and width *b* of the nanocavity have a significant influence on the spectral response of the structure. Fig. 3.4 (a) and (b) show the resonance wavelength as a function of nanocavity length *a* and width *b*, respectively.

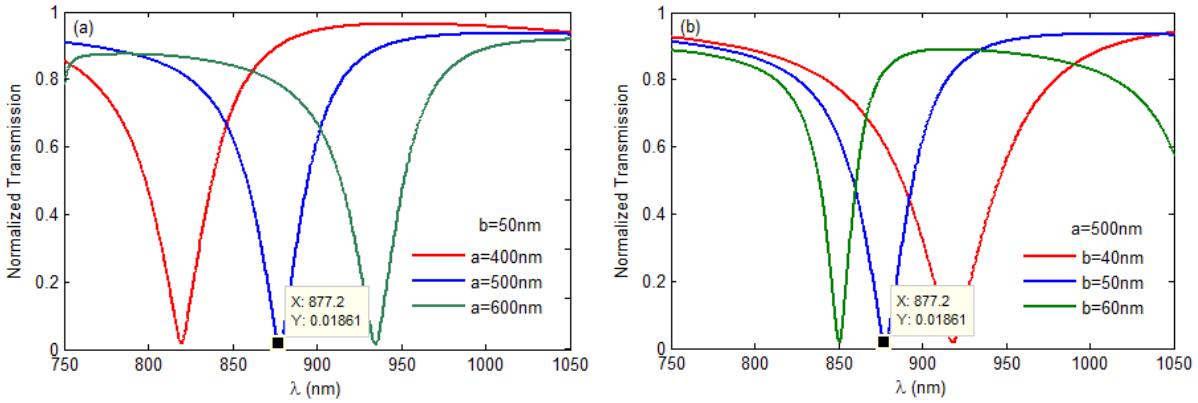

Fig. 3.4. (a) Transmission spectra of the proposed structure with single nanocavity versus nanocavity lengths of *a* at a fixed nanocavity width of *b* = 50 nm. (b) Transmission spectra of the proposed structure with single nanocavity versus nanocavity widths of *b* at a fixed nanocavity length of *a* = 500 nm.

From Fig. 3.4 (a), it is clear that the wavelength dip exhibits a red-shift with an increase in the nanocavity length. This is because as the nanocavity length *a* increases, the destructive resonance wavelength must be increased to satisfy the phase matching condition according to the Eq. (3.1). Also as shown in Fig. 3.4 (b), the destructive resonance wavelength experiences a blue-shift with an increase in the magnitude *b*. As the width *b* increases, n_{eff} decreases (as shown in Fig. 3.3 (a)), so the destructive resonance wavelength will be reduced to satisfy the phase matching condition in accordance with Eq. (3.1).

Fig. 3.5 illustrates the change of resonant wavelength with changes in the nanocavity length *a* and width *b*. As shown in Fig. 3.5, the resonant wavelength has a linear ($\delta a/\delta\lambda$=1.742) and a non-linear relationship with *a* and *b*, respectively.

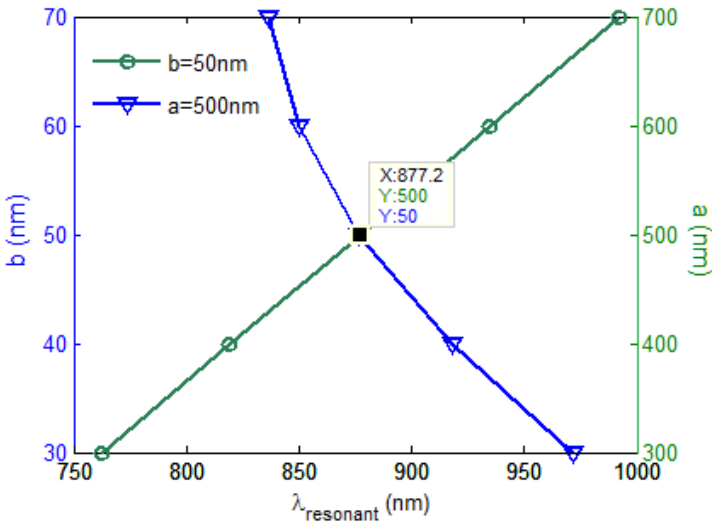

Fig. 3.5. Resonant wavelength versus the nanocavity length *a* (with fixed *b*=50 *nm*) and width *b* (with fixed *a*=500 *nm*).

From the above it is clear that it is possible to design a filter based on the MIM waveguide with a nanocavity resonator, where the dip wavelength can be changed by altering the parameters of the nanocavity.

3.2.2 Design of a dual-dip filter

In some situations there may be a need for filters with a two or more distinct dip wavelengths, where each individual dip wavelength can be separately determined. From the previous analysis it is clear that a simple combination in series of two single nanocavity based filters could meet this need but would require the space occupied by the two nanocavities. In order to maintain the benefit of very compact dimensions, a key question is how close together it is possible to place the two filters and their nanocavities.

For this analysis a dual-dip waveguide filter utilizing a combination of two different nanocavities is used, for example nanocavity 1 and 2 shown in Fig. 3.6. The nanocavity separation is a new parameter *r*.

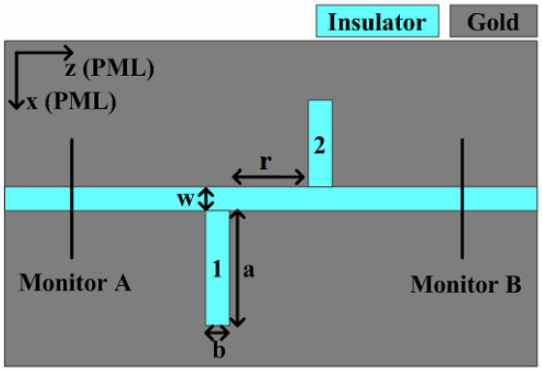

Fig. 3.6. Schematic structure of a dual-coupled cavity filter based on an MIM waveguide. The distance between two nanocavities is denoted as *r*.

For simplicity, the width of the two nanocavities *b* is fixed to be 50 *nm*, while the lengths of the two nanocavities *a* are different. Firstly, the effect of the relative position of the two nanocavities is investigated. The insets in Fig. 3.7 (b) and (c), show two possible arrangements of the nanocavities (located at different or same side of the waveguide) for realizing the dual-dip filter function. The lengths of the two nanocavities are $a_{(1,\,2)}$ = (800, 500) *nm*.

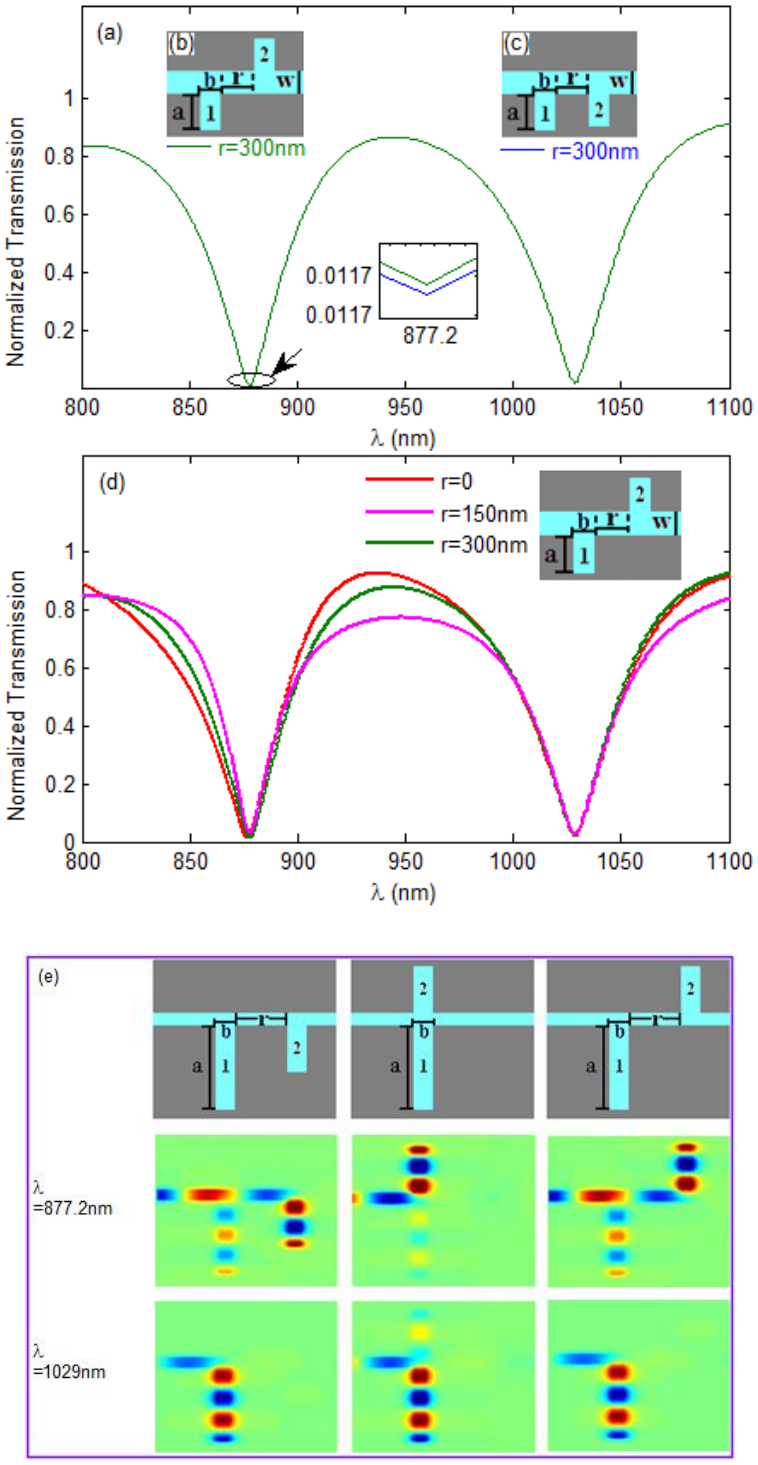

Fig. 3.7. (a) Transmission spectra of two types of a dual-dip filter. Insets: The schematic diagram of the structure with different arrangement of two nanocavities. The nanocavities are located at different sides of the waveguide (b) and at same side of the waveguide (c). (d) Transmission spectra of the structure with two nanocavities located at different sides of the waveguide with different interval *r*. (e) The contour profiles of the average field H_y at different fixed wavelengths for three structure types.

As shown in Fig. 3.7 (a), the transmission spectra for both arrangements are almost the same, which means that the relative positioning of the nanocavities along the waveguide has a negligible effect on the performance of the dual-dip SPPs filter. In addition, the influence of the interval parameter *r* on the transmission properties for the structure in Fig. 3.7 (b) was also analyzed and shown in Fig. 3.7 (d). From Fig. 3.7 (d) it is observed that the dip wavelengths are almost the same for different values of *r* varying from 0 to 300 nm. This result is significant as it suggests that it is possible to minimize the overall physical dimensions of the structure, but while still retaining the double dip response. The structure and the related normalized field distributions of *Hy* at different resonant wavelengths are shown in Fig. 3.7 (e). The stop-band wavelengths are 877.2 *nm* and 1029 *nm*, corresponding to those of the nanocavities 1 and 2, respectively. From the normalized field distributions we can see that the incident light at these wavelengths is effectively captured by the two nanocavities which forms the dual-dip filter, as well as the resonant modes excited in corresponding nanocavity.

The analysis of dual-dip filter suggests that the individual dip wavelength can be separately determined by selecting the desired parameters of the nanocavities.

3.3 Polarization beam splitter using an IMI waveguide

A PBS is an essential building block for integrated photonic circuits (IPCs), especially for components operating with one single polarization [8]. In order to develop next generation IPCs, it is essential to make the PBSs ultra-compact. To date most PBSs were based either on the principle of mode coupling [9-10] or adiabatic mode evolution [11] which suffer from the disadvantage of needing relatively large dimensions, for example, a device based on mode evolution, requires a length of more than 100 μm to achieve a sufficient extinction ratio [11].

In order to reduce the size, a promising approach is to design the PBS waveguides with an inherent high birefringence to realize a compact PBS [12]. The techniques used include silicon-based interferometers [13], photonic crystals [14] and asymmetric waveguide couplers [15], respectively with a typical size length of 40 μm, 20 μm and 10 μm. In comparison with these techniques, SPPs waveguides exhibit large birefringence and have been proposed for use as PBSs [16-17]. Recently a PBS with a compact size length ($\sim$ 2 μm) offering better mode confinement has been studied, which utilizes the evanescent field coupling between a hybrid plasmonic waveguide and a silicon nanowire [18]. The disadvantage of such a PBS is that it has a relatively small extinction ratio: 14 dB and 13 dB for TE and TM polarizations at a wavelength of 1550 nm, respectively. More recently, an ultra-compact PBS was designed based on the excitation of the localized SPPs (LSPPs) in Ref. [19]. The structure has relatively high extinction ratio and low insertion loss, but suffers from a complex fabrication due to the need for a nanoscale silver cylinder array.

To overcome these disadvantages, a novel PBS offering a high extinction ratio and low insertion loss is proposed here and investigated numerically by using FEM. The PBS is based on a three-core plasmonic directional coupler, which uses a LRSPPs based waveguide as the middle waveguide to achieve polarization selective coupling.

3.3.1 Two dimensional model PBS

Fig. 3.8 shows a schematic diagram of the proposed 2D-PBS based on a directional coupler which consists of two silicon waveguides (abbreviated as Si WG), each with a width of *w* and one plasmonic WG (PWG) which is composed of a thin metal film with a width of *t* sandwiched between two Si WGs with widths of *e* to support the LRSPPs mode. All these WGs are embedded in the SiO_2 substrate where *d* is the distance between the Si WG and the PWG. All the structural symbols and coordinates are also depicted in Fig. 3.8.

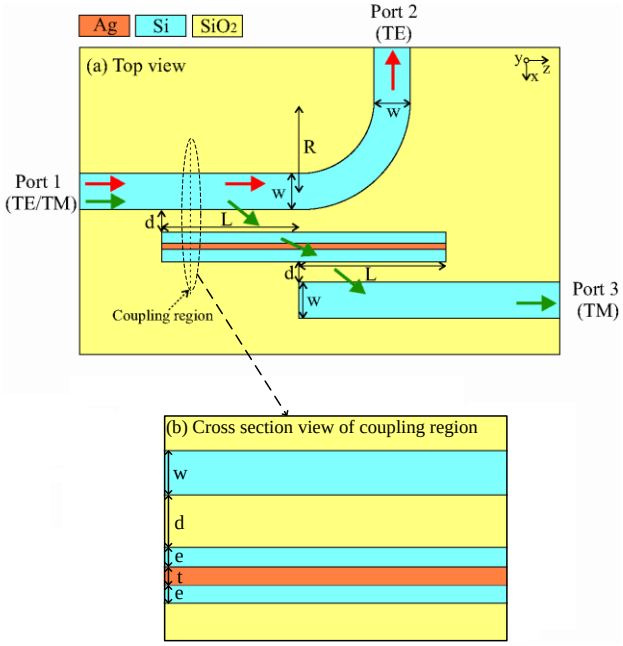

Fig. 3.8. (a) Top view of the proposed 2D-PBS based on a directional coupler. (b) Cross section of the coupling region of the PBS.

The coupling between the Si WG and PWG (namely the WG mode and LRSPPs mode) is polarization dependent. In other words, only the TM mode (an electric field perpendicular to the metal surface) can be coupled to LRSPPs mode while the TE mode cannot. Thus if the TM mode transmitted within the Si WG is fully coupled to the LRSPPs mode, this device can act as a PBS.

According to coupled mode theory (CMT) [20], in order to excite mode coupling, an effective refractive index matching condition (ERIMC) between these modes must be satisfied. To investigate the mode coupling for the proposed polarization beam splitter, a two-dimensional (2D) Finite Element Method (2D-FEM) is utilized.

Firstly, the effective refractive indices for the individual PWG and Si WG as functions of *e* and *w* are calculated and shown in Fig. 3.9. In these simulations the width of the metal film was assumed to be t = 20 nm; the wavelength was set as λ = 1550 nm and the metal used is silver, with the appropriate dielectric constants of silver selected from Ref. [21].

As shown in Fig. 3.9 (a), for an individual PWG, only two TM polarized modes are supported: LRSPPs and SRSPPs modes. Here the propagation length is calculated as $L_p = \lambda/[4\pi \mathrm{Im}(n_{eff})]$, where $\mathrm{Im}(n_{eff})$ is the imaginary part of the complex effective refractive index n_{eff} [22]. As shown in the inset of Fig. 3.9 (a), due to the high propagation loss of the SRSPPs mode, the propagation length of the SRSPPs mode is very short i.e. less than 3 μm, which is not sufficient for implementation of devices that require an inherently longer propagation length to function. For this reason only the LRSPPs mode was considered in this section. In addition, for an individual Si WG, both TM and TE modes will be supported as shown in Fig. 3.9 (b) where the cutoff widths for TE_1 and TM_1 polarized modes are 260.8 nm and 271.2 nm, respectively. In the following investigation, we fixed the Si WG width w to be 250 nm in order to support the fundamental mode only. Furthermore, Fig. 3.9 (a) and (b) indicate that for the case where e = 108 nm and w = 250 nm, the ERIMC is satisfied for the LRSPPs and the fundamental Si WG mode (TM_0).

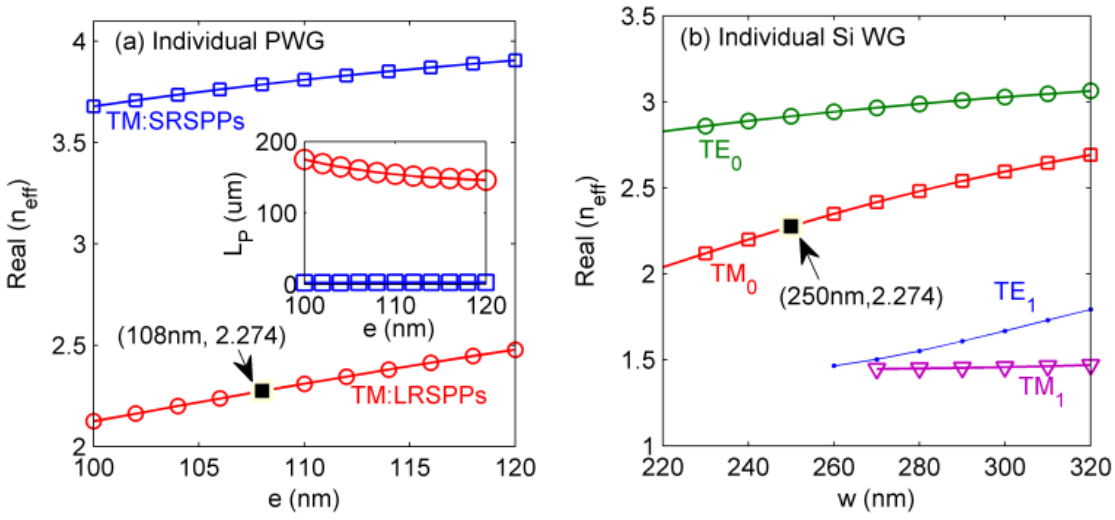

Fig. 3.9. (a) Real parts of effective refractive indices of supported modes for PWG as a function of *e*. The inset shows the associated propagation lengths. (b) Real parts of effective refractive indices of supported modes for Si WG as a function of *w*.

Given the ERIMC is satisfied, if the PWG and Si WG were placed in parallel and close to each other as shown in Fig. 3.8 (b), then coupling between LRSPPs and TM_0 WG takes place. However there is no power transfer between LRSPPs and TE_0 WG modes due to the fact that TE polarized light cannot excite SPPs modes. Based on CMT, there are two eigenmodes at the coupling region, an even mode and an odd eigenmode, as shown in Fig. 3.10. In this simulation, e = 108 nm, w = 250 nm as expected, and the value of d is chosen to be = 200 nm, which it will be shown later is an optimal value. Given the complex propagation constants $\beta_S = \beta_e + i\beta_e'$ and $\beta_a = \beta_o + i\beta_o'$ for even and odd modes, respectively, the coupling length L_C can be calculated as [20]:

$$L_C = \frac{\pi}{\beta_e - \beta_o} = \frac{\lambda}{2(n_{effe} - n_{effo})} \qquad (3.4)$$

where n_{effe} and n_{effo} are the real parts of the effective refractive indices for even and odd eigenmodes, respectively. For example, the calculated L_C for this case is L_C = 4.1 μm (n_{effe} = 2.365, and n_{effo} = 2.176).

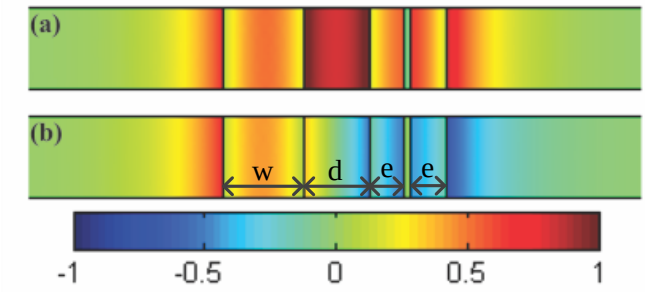

Fig. 3.10. E_x field distributions of two eigenmodes supported by the coupled waveguides (a) even mode, and (b) odd mode. In this simulation, e = 108 nm, w = 250 nm, t = 20 nm, λ = 1550 nm, and d = 200 nm.

Based on the above analysis, simulations were carried out with the proposed structure. Fig. 3.11 (a) shows the power output at ports 2 and 3 for different values of L in the structure as shown in Fig. 3.8. In this calculation, the parameters are d = 200 nm, w = 250 nm, and e = 108 nm. As expected for the TE polarized mode, nearly all the light power from port 1 is transmitted to port 2 and the light

coupling loss to port 3 is higher than 20 dB, while for TM polarized light, the transmitted powers for ports 2 and 3 do not change monotonically with the length of the coupling region because of the energy coupling between Si WGs and PWG. Due to this coupling, the transmitted powers to ports 3 and 2 reach their maximum/minimum values at some specific length *L*. For example, on the assumption that *d* = 200 nm, then at a coupling length of *L* = 4.1 μm (as noted by black dashed line), all of the TM polarized light will be coupled from port 1 to port 3. Fig. 3.11 (b) shows the associated light power intensity distributions for the proposed polarization splitter when TM and TE polarized light is injected into port 1 at a wavelength of 1550 nm.

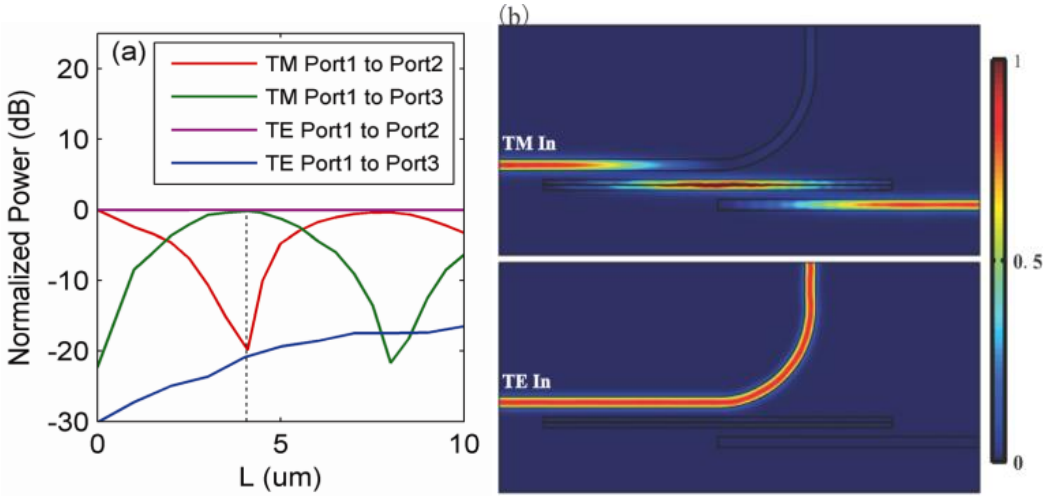

Fig. 3.11. (a) Plot showing the energy transfer between Si WGs and PWG as a function of *L*. The input port is Port 1. (b) Light power distribution in the designed PBS for TM and TE inputs at a wavelength of 1550 nm.

It is noted that for the TE polarized light in Fig. 3.11 (a), as the coupling length increases, the power variation from port 1 to port 2 is very small, but the power from port 1 to port 3 increases significantly. This could be possibly explained as follows: for TE polarization mode, there is very weak TE WG mode coupling from Port 1 to Port 3. As coupling length increases from 0 to 10 μm, there is significant increase (more than 10 dB) of power coupled from Port 1 to Port 3. However the absolute power coupled from Port 1 to Port 3 is very low, which

reflected the fact that there is almost no change for the power transmission from Port 1 to Port 2.

To characterize the performance of a PBS, three key factors need to be considered: bandwidth, insertion loss (IL), and extinction ratio (ER). Fig. 3.12 shows the spectral responses of the associated IL and ER for our proposed PBS. In the simulation the parameters are set as follows: d = 200 nm, w = 250 nm, L = 4.1 μm and e = 108 nm. It can be seen from Fig. 3.12 that in the C-band ranging from 1530 nm to 1565 nm, the PBS exhibits low ILs (lower than 0.5 dB) and high ERs (higher than 14 dB) for both TE and TM polarizations. At a wavelength of 1550 nm, the simulated ERs are 20.17 dB and 19.83 dB for TE and TM polarized light, respectively, and the corresponding ILs are as low as 0.17 dB and 0.25 dB, respectively.

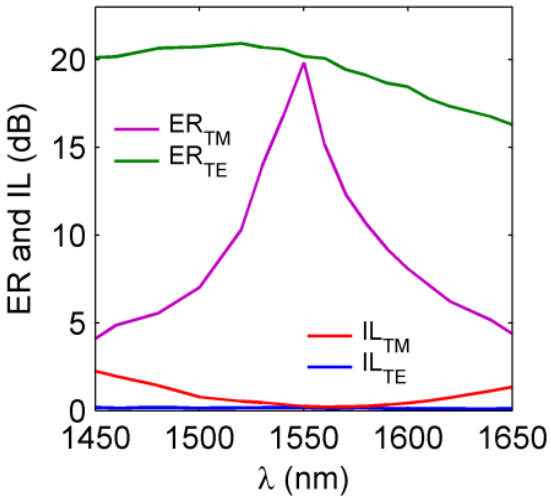

Fig. 3.12. Plot showing ERs and ILs as a function of wavelength for both TE and TM cases.

The effects of L on the IL and ER were also investigated as shown in Fig. 3.13 (a). In this simulation the parameters are d =200 nm, w = 250 nm, λ = 1550 nm and e = 108 nm. From Fig. 3.13 (a) it is easy to see that for TE polarized light, the associated IL and ER are affected only slightly by the variations in L; however for TM polarized light, as expected, the coupling length L has a significant influence on the ER and IL, and the maximum/minimum values are achieved for ER/IL at the lengths

of $L = n * L_C$, (where n = 1, 3, 5…). Fig. 3.13 (b) shows the effects of d on the IL and ER. In this simulation the parameters are L = 4.1 μm, w = 250 nm, λ = 1550 nm and e = 108 nm. Fig. 3.13 (b) shows that for TM polarized light, a maximum ER value of 19.83 dB and a minimum IL value of 0.25 dB are obtained for d = 200 nm, confirming the validity of the earlier use of this value of d. For TE polarized light, ER changes significantly when d < 300 nm and it saturates around 25 dB when d > 400 nm.

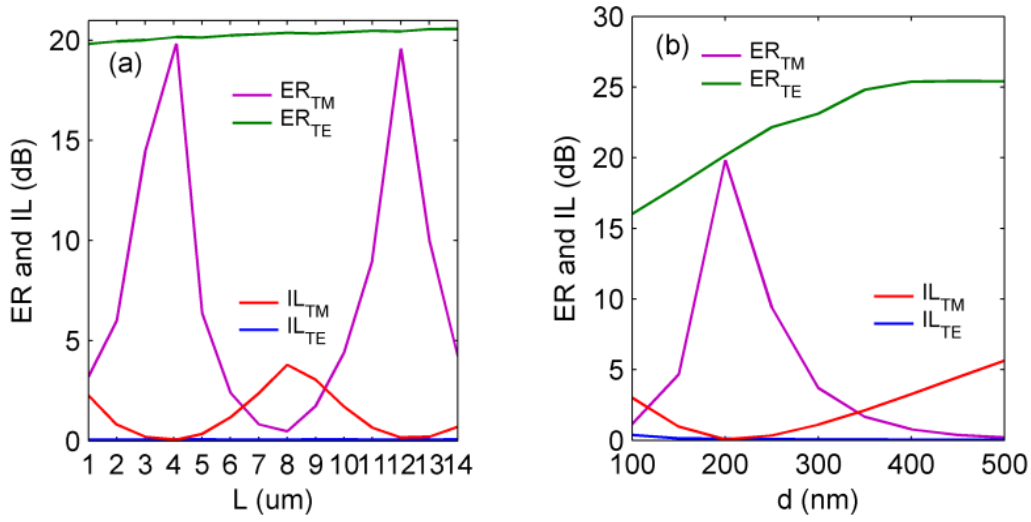

Fig. 3.13. Plot showing ERs and ILs as a function of the coupling length L (a) and separation distance d (b) for both TE and TM cases.

3.3.2 Three dimensional model PBS

The use of a 2D model has the advantage of being fast but clearly the depth of the structure is not accounted for. In this section a three dimensional (3D) analysis is used to determine if there are limitations on the 2D model that might make the increased computing time required for 3D models acceptable.

Therefore a 3D PBS is investigated to compare the results acquired with the 2D model above. The schematic diagram of the 3D model is shown in Fig. 3.14 (a). In the simulation, the values of d, w, t and e parameters were assumed to be the same as those used in the 2D model,

that is: d =200 nm, w = 250 nm, t = 20 nm and e = 108 nm. Fig. 3.14 (b) shows the effective refractive indices for the individual PWG and Si WG modes as functions of waveguide thickness h and g at λ = 1550 nm. As shown in Fig. 3.14 (b), the real parts of the effective refractive indices of LRSPPs and Si WG modes match well at the crossing points when $g = h$, where the ERIMC is satisfied.

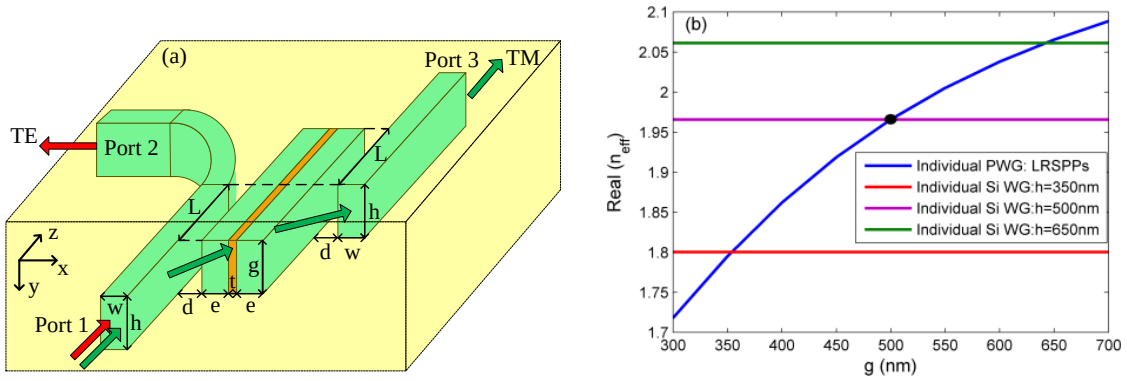

Fig. 3.14. (a) Cross section of the coupling region of the 3D PBS. (b) Real parts of effective indices of supported modes for individual PWG and Si WG.

Fig. 3.15 (a) shows the dependence of height parameters ($g = h$) on the ER and IL with λ = 1550 nm. It is noted that the coupling length will be changed as the height parameters vary. The relationship between the height parameters and the coupling length is shown in the inset (2) of Fig. 3.15 (a). As height g and h change, the IL and ER for TM polarization change insignificantly, whereas the variation for TE polarization is more obvious.

In addition, Fig. 3.15 (b) depicts the broadband spectral response of the IL and ER with L = 3.15 μm, g = 500 nm and h = 500 nm. The estimated extinction ratios for the TE and TM polarizations are 21.45 and 21.19 dB respectively with the corresponding ILs of 0.06 dB and 0.29 dB at λ = 1550 nm. For the whole C-band wavelength range, 3D model PBS exhibits low ILs (lower than 0.5 dB) and high ERs (higher than 16 dB) for both TE and TM polarizations.

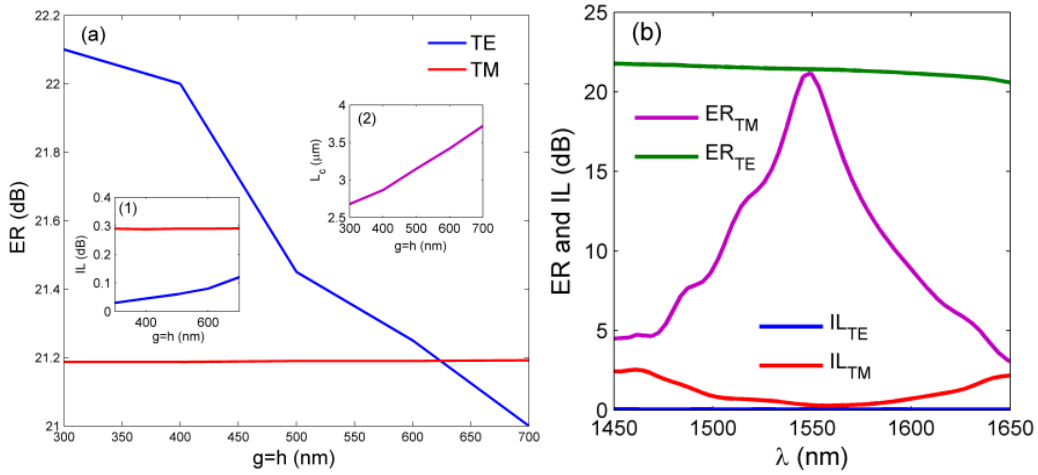

Fig. 3.15. Plot showing ERs and ILs as functions of height (a) *h* and (b) *g* for both TE and TM cases. (c) Plot showing ERs and ILs as a function of wavelength for both TE and TM cases for 3D model PBS.

From the above it is clear that the results obtained for 2D model PBS here are comparable with those for a 3D model PBS, but the 2D model has the significant advantage that the simulation times are several times shorter.

3.4 Summary

In this chapter, novel designs of MIM and IMI waveguide based filter and polarization beam splitter have been presented.

Based on the subwavelength confinement of the SPPs_MIM mode, a detailed study of an ultra-compact Fabry-Perot filter based on the MIM waveguide with nanocavity resonators is provided. The nanocavity can capture a surface plasmon wave (SPW) propagating within the insulator waveguide at a fixed resonance wavelength and thus acts as a plasmonic resonator. It is demonstrated that the transmission spectra were influenced by the characteristics of the nanocavity. The resonance wavelengths show a linear shift with the slope of 1.742 nm/μm with respect to the nanocavity length and a nonlinear shift with respect to the nanocavity width. The design of a dual-dip filter shows that the location of the two nanocavities, (i.e.

same or different side of the waveguide) as well as the interval between the nanocavities has only a marginal effect on the filter wavelengths.

In addition, a compact PBS based on a Si WG-PWG coupler is proposed and numerically investigated. The coupling between the WG mode and LRSPPs mode is polarization dependent. Calculations based on FEM showed that with proper structural parameters the proposed PBS can achieve an insertion loss of lower than 0.5 dB and an extinction ratio of higher than 14 dB across the entire C-band for both TE and TM polarizations. For example at a wavelength of 1550 nm, high extinction ratios of 20.17 dB and 19.83 dB, for TE and TM polarizations are demonstrated, respectively, and further improvement of the extinction ratios is possible by optimizing other parameters. The insertion losses of this PBS are as low as 0.17 dB and 0.25 dB.

3.5 References

1. Y. K. Gong, L. R. Wang, X. H. Hu, X. H. Li, and X. M. Liu, Broad-bandgap and low sidelob surface plasmon polariton reflector with Bragg-Grating-based MIM waveguide, *Opt. Express*, 17 (16), pp. 13727-13736, (2009).

2. H. Lu, X. M. Liu, D. Mao, L. R. Wang, and Y. K. Gong, Tunable band-pass plasmonic waveguide filters with nanodisk resonators, *Opt. Express*, 18 (17), pp. 17922-17927, (2010).

3. H. Lu, and X. M. Liu, Multi-channel plasmonic waveguide filters with disk-shaped nanocavities, *Opt. Commun.*, 284 (10-11), pp. 2613-2616, (2011).

4. Y. K. Gong, X. M. Liu, L. R. Wang, and Y. N. Zhang, Unidirectional manipulation of surface plasmon polariton by dual-nanocavity in a T-shaped waveguide, *Opt. Commun.*, 284 (3), pp. 795-798, (2011).

5. F. Z. Yang, and J. R. Sambles, Resonant Transmission of Microwaves through a Narrow

Metallic Slit, *Phys. Rev. Lett.*, 89 (6), pp. 063901, (2002).

6. Y. S. Chu, C.W. Lin, and W.S. Wang, Surface plasmon resonance sensors using silica-on-silicon optical waveguides, *Microw. Opt. Technol. Lett.*, 48 (5), pp. 955-957, (2006).

7. W. L. Barnes, Surface plasmon–polariton length scales: a route to sub-wavelength optics, J. Opt. A: Pure Appl. Opt., 8 (4), pp. S87-S93, (2006).

8. D. Dai, J. Bauters, and J. E. Bowers, Passive Technologies for Future Large-Scale Photonic Integrated Circuits on Silicon: Polarization Handling, Light Non-Reciprocity, and Loss Reduction, *Light Sci. Appl.*, 1, pp. 1-14, (2012).

9. A. Hosseini, S. Rahimi, X. Xu, D. Kwong, J. Covey, and R. T. Chen, Ultracompact and fabrication-tolerant integrated polarization splitter, *Opt. Lett.*, 36 (20), pp. 4047–4049, (2011).

10. H. Fukuda, K. Yamada, T. Tsuchizawa, T. Watanabe, H. Shinojima, and S. Itabashi, Ultrasmall polarization splitter based on silicon wire waveguides, *Opt. Express*, 14 (25), pp. 12401–12408, (2006).

11. M. R. Watts, H. A. Haus, and E. P. Ippen, Integrated mode-evolution-based polarization splitter, *Opt. Lett.*, 30 (9), pp. 967–969, (2005).

12. D. Dai and J. E. Bowers, Novel ultra-short and ultra-broadband polarization beam splitter based on a bent directional coupler, *Opt. Express*, 19, pp. 18614, (2011).

13. D. Dai, Z. Wang, J. Peters, and J. E. Bowers, Compact polarization beam splitter using an asymmetrical mach–zehnder interferometer based on silicon-on-insulator waveguides, *Photon. Technol. Lett.*, 24, pp. 673, (2012).

14. X. Ao, L. Liu, L. Wosinski, and S. He, Polarization beam splitter based on a two-dimensional photonic crystal of pillar type, *Appl. Phys. Lett.*, 89 (17), pp. 171115, (2006).

15. D. Dai, Z. Wang, and J. E. Bowers, Ultrashort broadband polarization beam splitter based

on an asymmetrical directional coupler, *Opt. Lett*., 36 (13), pp. 2590–2592, (2011).

16. F. Lou, D. X. Dai, and L. Wosinski, Ultracompact polarization beam splitter based on a dielectric–hybrid plasmonic–dielectric coupler, *Opt. Lett.*, 37, pp. 3372-3374, (2012).

17. X. W. Guan, H. Wu, Y. C. Shi, L. Wosinski, and D. X. Dai, Ultracompact and broadband polarization beam splitter utilizing the evanescent coupling between a hybrid plasmonic waveguide and a silicon nanowire, *Opt. Lett.*, 38, pp. 3005-3008, (2013).

18. X. W. Guan, H. Wu, Y. C. Shi, L. Wosinski, and D. X. Dai, Ultracompact and broadband polarization beam splitter utilizing the evanescent coupling between a hybrid plasmonic waveguide and a silicon nanowire, *Opt. Lett.*, 38, pp.3005-3008, (2013).

19. Q. L. Tan, X. G. Huang, W. Zhou, and K. Yang, A plasmonic based ultracompact polarization beam splitter on silicon-on-insulator waveguides, *Scientific Reports*, 3, pp. 2206, (2013).

20. D. Marcuse, Light Transmission Optics, 2nd ed. (Van Nostrand Reinhold, 1982).

21. E. D. Palik, Handbook of optical constants of solids (Academic Press, 1998).

22. J. Zhang, L. K. Cai, W. L. Bai, Y. Xu, and G. F. Song, Hybrid plasmonic waveguide with gain medium for lossless propagation with nanoscale confinement, *Opt. Lett.*, 36, pp. 2312-2314, (2011).

Chapter 4: Dielectric loaded plasmonic waveguide devices

4.1 Introduction

In addition to MIM and IMI waveguides considered in Chapter 3, there is another type of SPPs based waveguide, namely a dielectric-loaded SPPs (DLSPPs) waveguide [1-3], which typically consists of a dielectric ridge waveguide placed on a metal surface. Compared to traditional MIM and IMI waveguides, a DLSPPs waveguide offers a better compromise in the tradeoff between the propagation length and mode confinement. Inspired by the principle of the LRSPPs mode, researchers have proposed a new class of DLSPPs waveguides, called a long-range DLSPPs (LRDLSPPs) waveguide [4-5], which involves basically designing the DLSPPs waveguide to be a symmetrical structure. The LRDLSPPs mode features a propagation length over several hundreds of micrometers, which is significantly longer than that achieved by the DLSPPs mode i.e. several tens of micrometers. However the mode confinement achieved is still weak and therefore there is scope for further improvement of the LRDLSPPs structure.

However to fabricate such a DLSPPs waveguide, advanced and costly nanofabrication techniques are required, such as photolithography, focused ion beam (FIB), electron-beam lithography (EBL), and/or reactive ion etching (RIE). But an alternative method is to use a low cost microfiber as a substitute for the dielectric waveguide in the DLSPPS structure. As a potential candidate for miniaturizing of optical components, microfiber is attracting an increasing interest due to its relatively simple fabrication and unique properties such as a strong evanescent field [6].

In this chapter, two distinct research topics are considered: 1) a theoretical investigation of a LRDLSPPs waveguide with the aim to improve its performance in terms of mode confinement and propagation length and 2) a proposal and investigation of a novel low cost microfiber loaded SPPs (MFLSPPs) structure combined with its experimental verification.

Regarding the first research topic, a novel LRDLSPPs waveguide offering lower loss but with a higher degree of mode confinement is proposed and investigated. Compared to the existing LRDLSPPs waveguide, the waveguide proposed here integrates an altered metallic structure with LRDLSPPs which gives a longer propagation length for the same mode confinement or a tighter mode confinement for the same propagation length.

For the second topic, by combining the advantages of SPPs and microfiber, a novel MFLSPPs based TE-pass polarizer is proposed and investigated both theoretically and experimentally. The proposed TE-pass polarizer is based on an optical microfiber placed on the top of a silver substrate. The simulation results show that the loss in the fundamental TE mode is relatively low while the fundamental TM mode suffers from a large metal dissipation loss due to the excitation of the microfiber-loaded surface plasmonic mode.

4.2 LRDLSPPs waveguide with a better tradeoff between mode confinement and propagation length

Due to its long propagation length, the LRDLSPPs waveguide has been studied intensively, for example, a LRDLSPPs based waveguide-ring resonator (WRR) has been proposed and investigated. The calculation results revealed that the Q factor of the LRDLSPPs based WRR is as high as 1380, which is one order of magnitude greater than that of the DLSPPs based WRR [7]. Recently V. S. Volkov *et. al.* have experimentally demonstrated a low-loss (estimated propagation length of up to $\sim$500 μm) and well-confined (mode width $\sim$1 μm)

LRDSLSPPs mode using a scanning near-field optical microscope (SNOM) [8]. Quite recently a novel LRDLSPPs waveguide consisting of a low refractive index rectangle dielectric waveguide where a thin layer of a metal film embedded in the centre of the rectangular waveguide has been proposed and theoretically analyzed [9], demonstrating a long propagation length (~756 μm) but at the expense of weak mode confinement.

To offer lower propagation loss but with a higher degree of mode confinement, a novel LRDLSPPs waveguide is proposed and investigated here. The waveguide utilizes the configuration of conventional LRDLSPPs but with an enhanced metallic geometry. Fig. 4.1 (a) illustrates a conventional LRDLSPPs waveguide with a uniform metal film (with a thickness of *h*) symmetrically embedded inside a dielectric waveguide with a thickness *H* and a width *G* surrounded by air, while Fig. 4.1 (b) shows a cross-sectional view of the proposed LRDLSPPs waveguide, which consists of a patterned thin metal film (with a thickness *d* and a width *g* in the central region, and a thickness *h* at both sides) Clearly when $d = h$, the two structure have identical geometries. For such a symmetrical configuration, the index matching condition is satisfied so that a LRDLSPPs mode is supported.

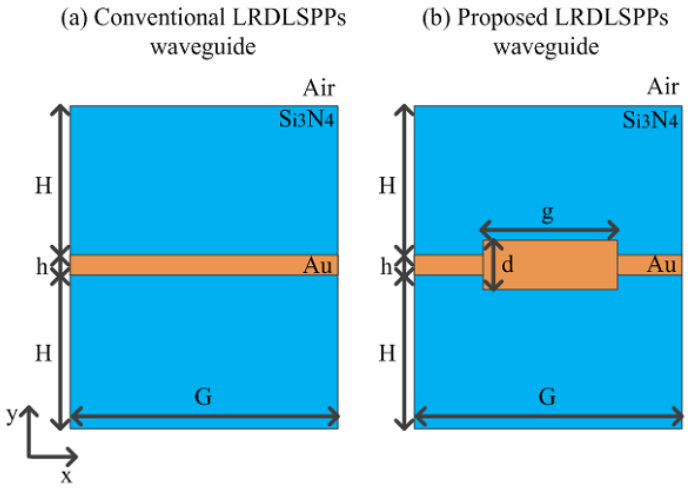

Fig. 4.1. Schematic views of (a) the conventional LRDLSPPs waveguide and (b) the proposed LRDLSPPs waveguide.

In the sub-sections that follow, a comparison is undertaken between a conventional LRDLSPPs structure and that with an enhanced metallic waveguide geometry. For this comparison it is an assumed that the dielectric material for both structures is chosen to be Si_3N_4 which has a refractive index of n_r = 2.0, and that gold is used as the metal with a refractive index of n_m = 0.55+11.5i at the optical communication wavelength of λ_0 = 1550 nm. In the numerical simulations, a FEM is adopted to analyze the characteristics of the LRDLSPPs mode.

4.2.1 Influence of the waveguide geometry of the metal film on mode properties

It is useful at the outset to provide a rationale for why an enhanced waveguide geometry might be useful. A starting point is to consider the relationship between the LRDLSPPs mode and the gold film thickness h for a conventional LRDLSPP plasmonic waveguide, where the value of h is uniform. Fig. 4.2 shows the calculated L_p and A versus gold thickness.

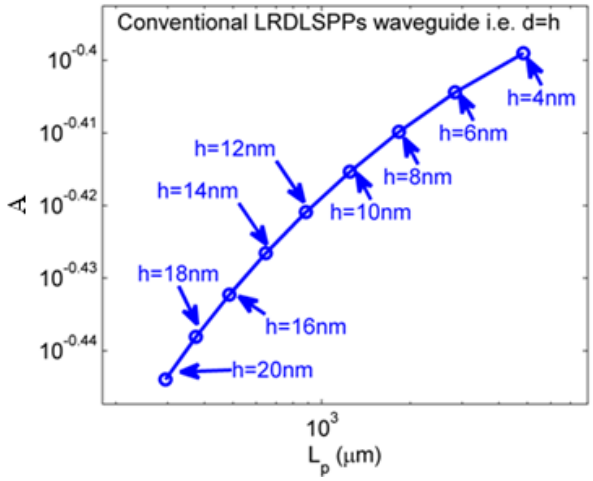

Fig. 4.2. The propagation length and normalized mode area versus h. In this case, H = 400 nm and G = 600 nm.

As shown in Fig. 4.2, both the propagation length L_p and normalized mode area A of the LRDLSPPs mode increases as the thickness of the metal film decreases. As expected, since a larger normalized mode area corresponds to a lower degree of mode confinement, there is a

trade-off between the mode confinement and propagation length. Thus increasing the metal film thickness can result in a better field confinement, but will introduce higher transmission loss. Conversely a decrease in the metal film thickness can enhance the propagation length, but will degrade the mode confinement. To mitigate this tradeoff it is worth considering if a patterned metal film thickness geometry could improve the tradeoff where the waveguide thickness is no longer uniform but now has two values, d and h as shown in Fig. 4.1 (a).

In our simulation two sets of fixed parameters are used for the proposed structure:

Set (I): H = 400 nm, G = 600 nm, h = 4 nm, g = 300 nm

Set (II): H = 400 nm, G = 600 nm, h = 10 nm, g = 300 nm

The dimensions are used to satisfy the requirements of photonic devices needing both tight mode field confinement and long propagation length [7]. Fig. 4.3 shows simulated results of the dependence of L_p and A of the LRDLSPPs mode on the geometric parameter d. The results for the conventional structure ($d = h$) are also provided in Fig. 4.3 for comparison.

From Fig. 4.3 it can be seen that compared to a conventional structure, for a fixed propagation length of L_p, the proposed structure has a smaller value of A (and hence better mode confinement) when $d > h$ (purple curve in Fig. 4.3). However for the simulation with a larger value of h (h = 10 nm, red curve in Fig. 4.3), it is found that the improvement in the proposed structure's mode confinement is lower as h increases, and in fact beyond a value of L_p = 1246 μm, the proposed structure has a higher value of A (and hence worse mode confinement). Alternatively for the same value of A, the value of L_p is higher for the proposed structure as long as $d > h$. For example, for A = 0.36, the value of L_p is 828 μm (purple curve in Fig. 4.3) for the proposed structure, which is far longer than that of 295 μm for the conventional structure. However, for the simulation with a larger value of h (red curve as

shown in Fig. 4.3), it is found that the merit of the proposed structure is reduced as h increases i.e. for h = 10 nm, at A = 0.36, the value of L_p is only marginally higher than that for the conventional structure. Also it can be seen that beyond the value of A = 0.5918, the proposed structure actually has a lower value of propagation length L_p.

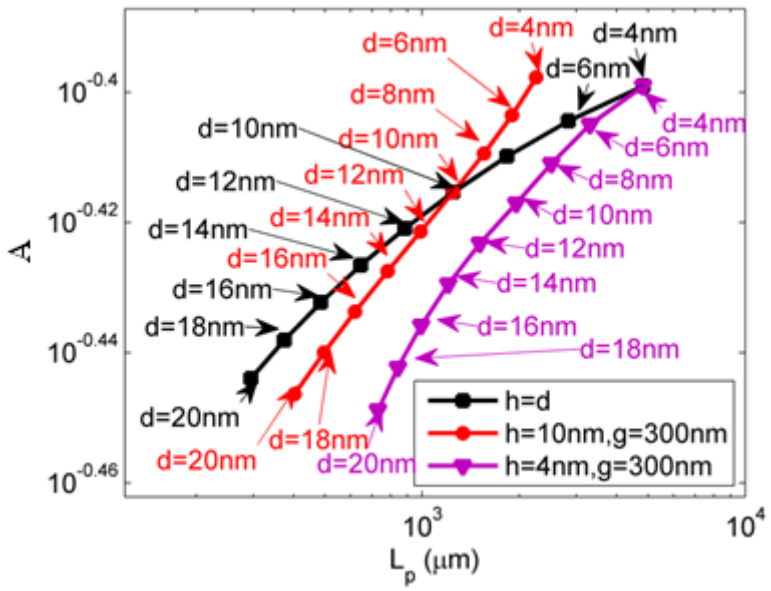

Fig. 4.3. The normalized mode area A as a function of the propagation length L_p for the conventional and proposed LRDLSPPs structure (with a fixed value of g).

In addition, the influence of the dimension g on the proposed structure (L_p and A) was investigated and simulation results are shown in Fig. 4.4. In this simulation, two sets of parameters were again selected:

Set (I): H = 400 nm, G = 600 nm, h = 4 nm, d = 20 nm

Set (II): H = 400 nm, G = 600 nm, h = 10 nm, d = 20 nm

The corresponding results for the conventional structure are also provided in Fig. 4.4 for comparison. As shown in Fig. 4.4, the performance of the proposed structure is highly dependent on the value of g. The tightest mode confinements can be achieved at g = 300 nm

for both selected values of *h*. As shown in Fig. 4.4, a lower value of *h* has better performance than that with higher value of *h*. For example, for the same value of A = 0.36, the structure with h = 4 nm, g = 100 nm and d = 20 nm has a propagation length of L_p = 1753 μm compared to a value of L_p = 689 μm for the structure with h = 10 nm, g = 100 nm and d = 20 nm. It should be noted that both proposed structures have substantially longer propagation lengths than that of 295 μm achieved by the conventional structure.

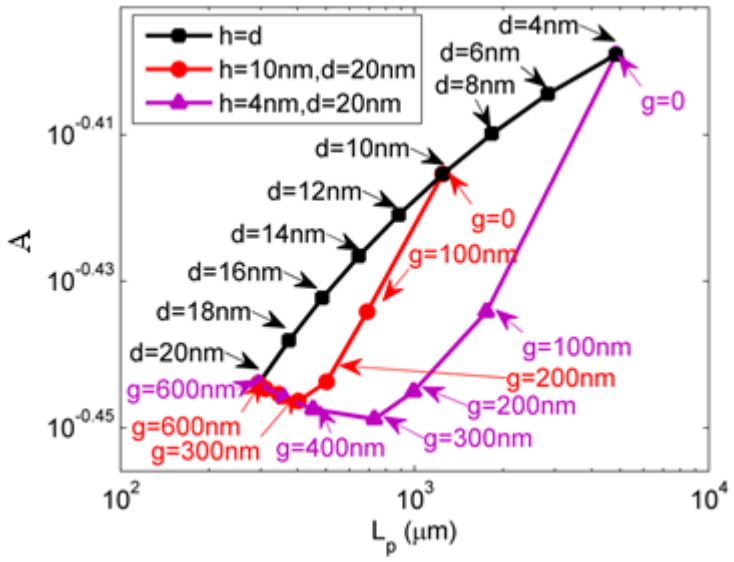

Fig. 4.4. The normalized mode area A versus the propagation length L_p for the conventional and proposed structure, (with a fixed value of *d*).

Based on the results shown in Fig. 4.3 and Fig. 4.4, it can be concluded that the proposed LRDLSPPs waveguide offers flexibility in the design of SPPs that can achieve both a longer propagation length and tighter mode confinement simply by appropriately selecting the parameters *g*, *h* and *d*.

4.2.2 Crosstalk between adjacent waveguides

To illustrate further the benefits of the proposed structure it is useful to consider the implications for crosstalk between waveguides, in situations where several adjacent

waveguides are integrated together in close proximity. The explosive demand for the increase in data communication capacity has stimulated the rapid development of optical communication systems. One of the challenges for next generation optical communication systems is the development of ultra-compact photonic devices and sub-systems. Crosstalk between the adjacent waveguides (related to the coupling length) is one of the key factors that restricts the density of photonic devices. It is hence important to investigate the influence of crosstalk on the proposed structure.

Fig. 4.5 (a) shows the calculated coupling length L_c as a function of separation distance D for two parallel waveguides for different configurations: two horizontally parallel waveguides and two vertically parallel waveguides. For comparison purposes, the coupling lengths for the conventional structures with $d = h = 10$ nm are also provided in Fig. 4.5 (a). As shown in the insets in Fig. 4.5, the parameters in the simulation are set as $H = 400$ nm, $G = 600$ nm, $h = 10$ nm, $d = 20$ nm and $g = 300$ nm). The coupling length is given by $L_c = \pi / (\beta_s - \beta_a)$, where β_s and β_a are the propagation constants of the symmetric and anti-symmetric modes of the two adjacent waveguides, respectively. In effect the coupling length represents the propagation length at which a total transfer of energy from one waveguide to an adjacent waveguide will have taken place. A long coupling length will result in a low level of crosstalk, which allows for tighter integration. Fig. 4.5 (b) and (c) show the amplitude distributions of E_y for symmetric and anti-symmetric modes with $D = 200$ nm between two horizontally parallel waveguides, and the corresponding results for two vertically parallel waveguides are shown in Fig. 4.5 (d) and (e), respectively.

From Fig. 4.5 (a), it can be seen that for both the conventional structure and the proposed structure, the coupling lengths increase significantly for both cases as D increases. However, for the case of vertically parallel waveguides, the coupling length of the proposed structure is

longer than that of conventional structure, which illustrates that the crosstalk of the proposed structure is lower than that of conventional structure, in other words, high-density independent function photonic elements are more easily integrated in the case of the proposed structure, at least where waveguides are stacked vertically.

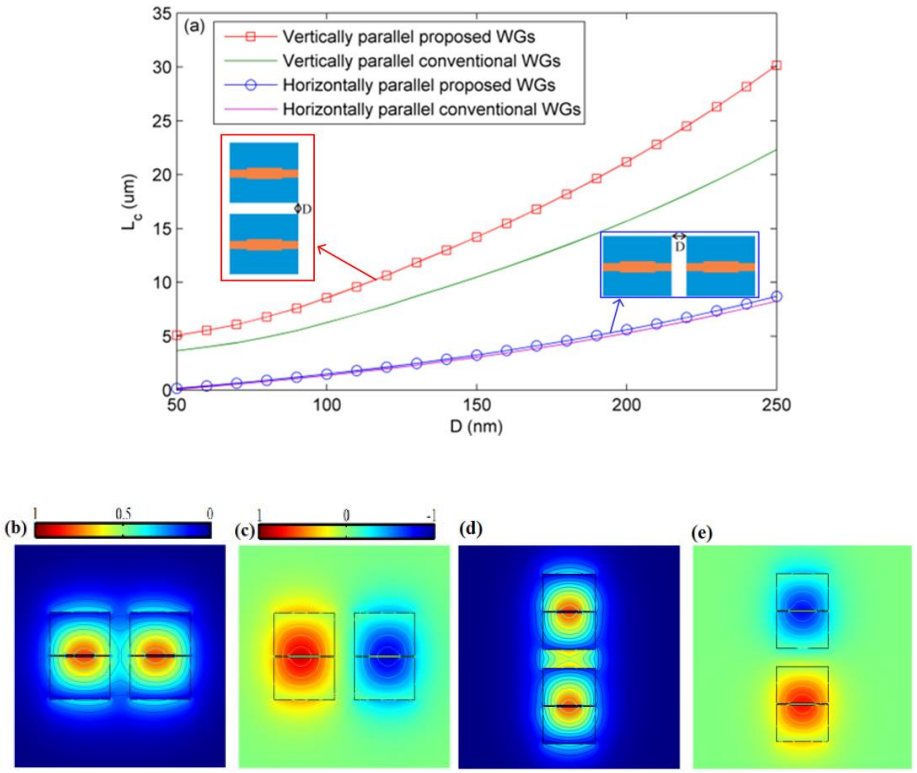

Fig. 4.5. (a) The coupling lengths versus the separation between the two horizontally and vertically parallel waveguides. Amplitudes of E_y for the symmetric mode (b) and the anti-symmetric mode (c) with D = 200 nm between two horizontally parallel waveguides. Amplitudes of E_y for the symmetric mode (d) and the anti-symmetric mode (e) with D = 200 nm between two vertically parallel waveguide.

For the case of horizontally parallel waveguides, the proposed structure has similar coupling lengths compared to that of the conventional structure. The implication is that the proposed structure will only allow for lower crosstalk in cases where vertical integration is used. In fact for the horizontally parallel waveguide case the coupling length is significantly lower than that of DLSPPs waveguide reported in [10], which is typically 10 μm.

4.3 MFLSPPs based TE-pass polarizers

Control of the polarization state of light is of great interest for many photonic circuit applications, especially for systems operating with one single polarization [11]. One way to address this issue is to split light into two orthogonal polarizations utilizing a polarization beam splitter (PBS) [12-13]. While the solution involving a PBS is satisfactory it comes at a price in increased system complexity. Another approach is to use a polarizer to transit the wanted polarization state and extinguish the undesired polarization state by reflection, redirection or absorption [14]. Basically since only the TM polarized light can be coupled to the high-loss SPPs mode while the TE polarized light cannot, this makes SPPs ideal for constructing highly compact polarizers. Based on this principle of polarization-dependent excitation, Y. Wakabayashi proposed a TM-pass/TE-stop polarizer consisting of a silver film sandwiched between dielectric gratings and demonstrated an extinction ratio of more than 17 dB over a wavelength range of 1500 nm to 1750 nm [15]. More recently, X. Sun experimentally illustrated a hybrid plasmonic TE-pass polarizer with an extinction ratio that varies from 23 dB to 28 dB in the 1520 nm-1580 nm wavelength range, utilizing the high-loss characteristic of the SPPs mode to extinguish the TM mode [16]. Although these plasmonic polarizers show a relatively high extinction ratio for the desired polarization state, they suffer from the disadvantage of complex fabrication processes.

To overcome this disadvantage in this thesis, a microfiber with relatively simple fabrication process is utilized in the DLSPPs configuration. Fig. 4.6 (a-b) shows the schematic diagram of the proposed polarizer, which consists of a microfiber with a diameter of *D* directly placed on a silver layer (Ag) coated on a glass substrate with a width of *L*. All the structure symbols and accepted coordinate system are depicted in Fig. 4.6 (a-b). The mode properties and transmission of the proposed polarizer are numerically investigated by utilizing the FEM. In the numerical simulations,

the wavelength dependent permittivities of SiO_2 and Ag are those defined in [17] and [18], respectively.

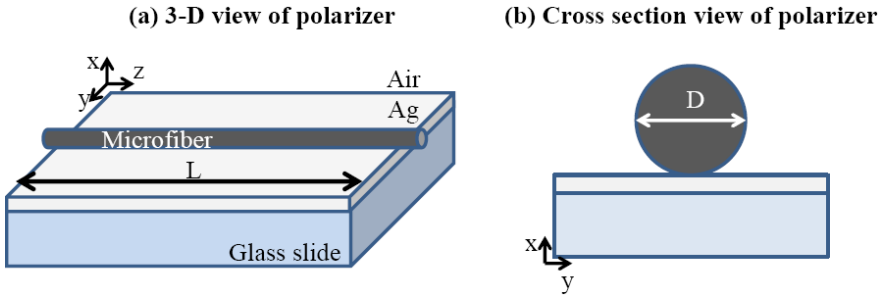

Fig. 4.6. (a) 3-Dimentional view and (b) cross section view of the proposed polarizer. The diameter of the microfiber is *D*, and the length of the polarizer is *L*.

4.3.1 Simulation and design of MFLSPPs based TE-pass polarizers

It is necessary prior to an experimental investigation to carry out simulations of the proposed structures in order to underpin the design process. Fig. 4.7 (a) shows the simulated wavelength dependence of the propagation length of the structure for the TM and TE modes with the microfiber diameters *D* of 3, 4 and 5 μm. This range of microfiber diameters is chosen on the basis that while fibers with diameters less than 3 μm potentially offer a better extinction ratio, fibers with diameters less than 3 μm are difficult to handle mechanically. On the other hand while large fiber diameters are easier to deal with mechanically, the extinction ratios will not be as good. Here the propagation length is calculated as $L_p = \lambda / [4\pi \mathrm{Im}(n_{eff})]$, where $\mathrm{Im}(n_{eff})$ is the imaginary part of the complex effective refractive index n_{eff}. As shown in Fig. 4.7 (a), over the wavelength range from 1500 nm to 1600 nm, the propagation length of the TE mode is much longer than that of the TM mode, or in other words, the TM mode has much higher transmission loss compared to TE mode. For example, when D = 3 μm and λ = 1550 nm, the propagation length of the TE mode ($L_{p(TE)}$ = 63.6 mm) is 20.5 times longer than that of TM mode ($L_{p(TM)}$ = 3.1 mm). When D = 5 μm and λ = 1550 nm, the propagation length difference between TE and TM modes becomes even larger (28.4 times longer for $L_{p(TE)}$ = 252.6 mm compared to $L_{p(TM)}$ = 8.9 mm). Based on these results, the proposed structure can be implemented as a

broadband TE-pass polarizer with a flat response from 1500 to 1600 nm, by properly selecting the structure dimensions.

To explore this loss mechanism, the normalized electric energy distributions at λ = 1550 nm corresponding to the points of *b* (*D* = 3 μm for TM mode), *c* (*D* = 3 μm for TE mode), *d* (*D* = 5 μm for TM mode) and *e* (*D* = 5 μm for TE mode) in Fig. 4.7 (a) are respectively plotted in Figs. 4.7 (b), 4.7 (c), 4.7 (d) and 4.7 (e). From Fig. 4.7 (b-e), it is clear that the TE mode is confined inside the microfiber, resulting in a relatively low propagation loss. On the other hand, the TM mode is coupled to the well-known DLSPPs mode [19] with a portion of electric field confined to the Ag surface, resulting in a relatively high propagation loss due to the large metallic dissipation. Furthermore, from Fig. 4.7 (a) it is also found that the propagation length decreases as the diameter *D* decreases.

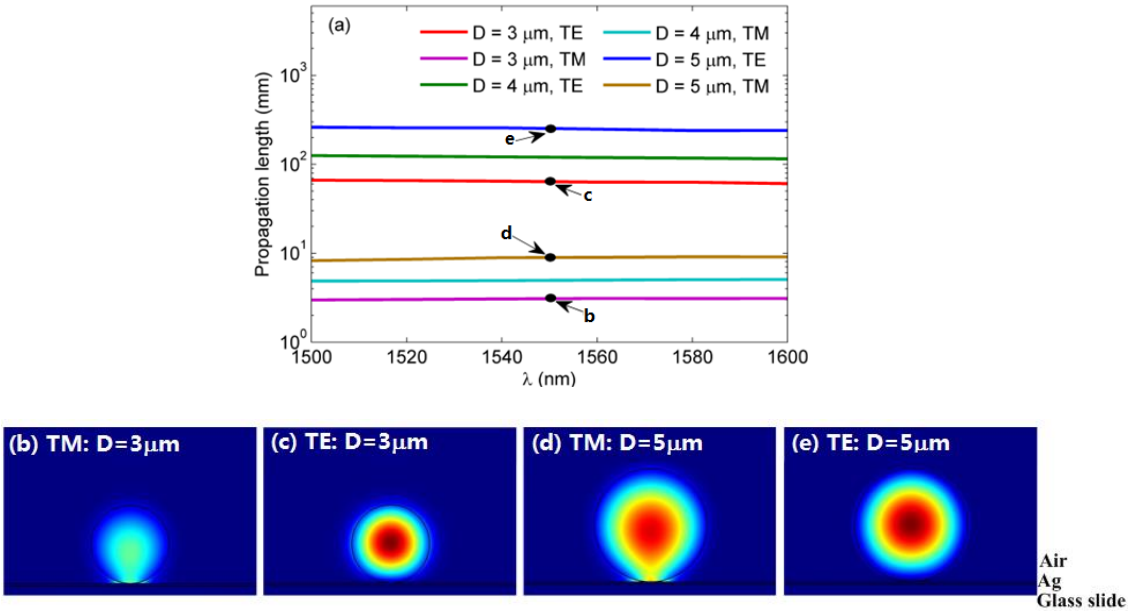

Fig. 4.7. (a) Wavelength dependence of the propagation length for the microfiber with different diameter *D* for the TM and TE modes. Normalized electric energy distributions at the wavelength of 1550 nm: (b) *D* = 3 μm for TM mode, (c) *D* = 3 μm for TE mode, (d) *D* = 5 μm for TM mode and (e) *D* = 5 μm for TE mode.

The propagation length behavior could be explained by considering the percentage of evanescent field with respect to the whole field (P) which is defined as

$$P = 1 - \iint W(\vec{r})\mathrm{dS}_{\mathrm{microfiber}} / \iint W(\vec{r})\mathrm{dS}_{\mathrm{whole}} \qquad (4.1)$$

where the electromagnetic energy density $W(\vec{r})$ is calculated as [20]

$$W(\vec{r}) = \frac{1}{2}\,\mathrm{Re}\left\{\frac{d[\omega\varepsilon(\vec{r})]}{d\omega}\right\}|E(\vec{r})|^2 + \frac{1}{2}\mu_0|H(\vec{r})|^2 \qquad (4.2)$$

where ω is the angular frequency of the incident light, $\varepsilon(\vec{r})$ is the dielectric permittivity, μ_0 is the vacuum magnetic permeability, $|E(\vec{r})|^2$ and $|H(\vec{r})|^2$ are the intensities of the electric and magnetic fields, respectively.

Fig. 4.8 shows the dependence of P on the diameter D at λ = 1550 nm. As shown in Fig. 4.8, for smaller diameters D, the evanescent field of the microfiber is stronger relative to the total field energy; hence a larger portion of power will be in contact with the metal resulting in a larger metal dissipation loss and hence shorter propagation length.

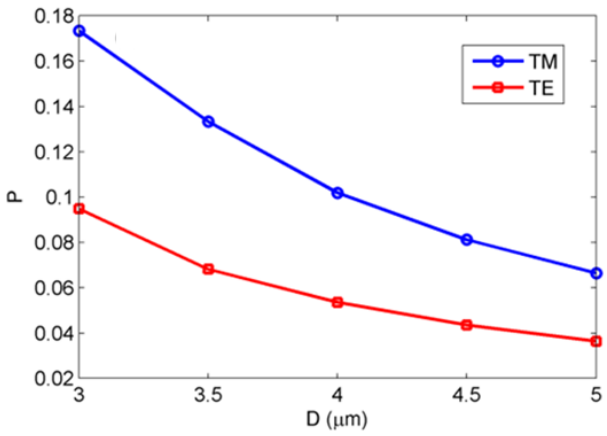

Fig. 4.8. The percentage of level of evanescent field with respect to the level of the whole field versus the diameter D at a wavelength of 1550 nm.

The transmission of the proposed polarizer with D = 4 μm and L = 3 mm was also calculated as shown in Fig. 4.9 (a). For this simulation, the approximate RAM requirement for the

computer is larger than 500 GB due to the large ratio R between the length L of the silver substrate and simulated wavelength. Hence it was proposed to use "transfer" method as follows: the device was divided into 30 sections with the length of each section set at 100 μm. The simulation required RAM for each section was reduced to around 60 GB. The first section was calculated, and then its output boundary mode was exported as the incident boundary mode for the second section and so on. The remaining sections can be processed in the similar manner. To verify the correctness of the "transfer" method, a short section 100 μm long of the device was divided into 10 sections and the results were calculated and compared with calculations from simulating the 100 μm short section as a whole. It was found that both methods have the same results indicating that the "transfer" computational method is correct.

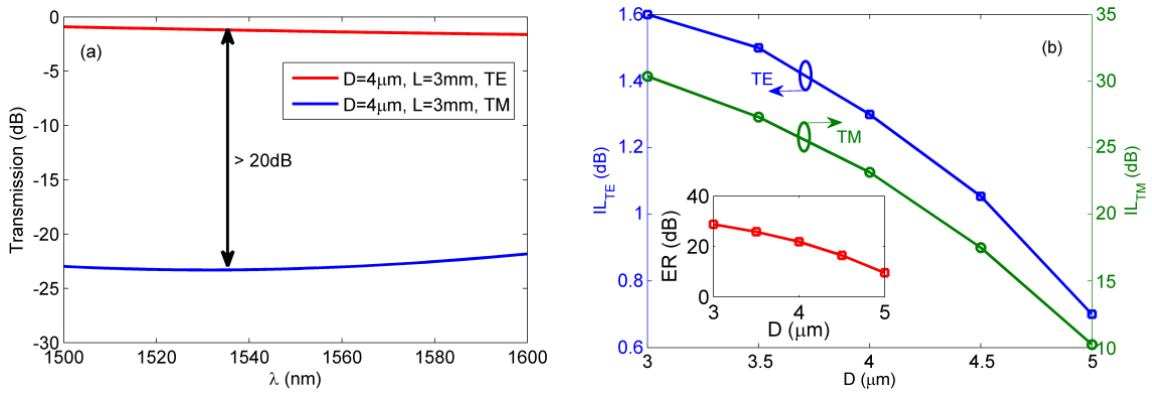

Fig. 4.9. (a) Normalized transmission spectra for TM and TE modes. (b) Plot showing IL_{TE}, IL_{TM} and ER (inset) against microfiber diameter D at the wavelength of 1550 nm.

From Fig. 4.9 (a) it is found that over the considered wavelength range, the TE mode could transit through the polarizer with a relatively low loss (insertion loss IL_{TE} < 1.6 dB) while the transmission for TM mode is suppressed (IL_{TM} > 22 dB), thus a polarization extinction ratio (ER) greater than 20 dB over the whole wavelength range from 1500 nm to 1600 nm is achieved. Fig. 4.9 (b) shows IL_{TE}, IL_{TM} and ER (inset) for various microfiber diameters D at 1550 nm. As expected from Fig. 4.9, IL_{TE}, IL_{TM} and ER decreases as D increases. The larger extinction ratio is achieved at smaller D, but at the cost of the increased insertion loss.

4.3.2 Experimental verification of MFLSPPs based TE-pass polarizers

To verify the theoretical analysis above, experiments were carried out for a TE-pass polarizer with microfiber dimensions of [*D*, *L*] = [4 μm, 3 mm]. The overall structure is a tapered fiber on a substrate (i.e. an Ag coated glass slide), where the length of the tapered fiber is slightly longer than that of the substrate.

Fig. 4.10 shows the microfiber fabrication setup. The standard single mode fiber (SMF) SMF-28 was clamped on two linear motorized motion stages, and its middle section was heated by a ceramic micro-heater (CMH-7019, NTT-AT) to a temperature of up to 1300℃ to soften the fiber for tapering. A customized LabVIEW program was used to precisely control the movement of the motion stages to control the diameter and length of the tapered microfiber.

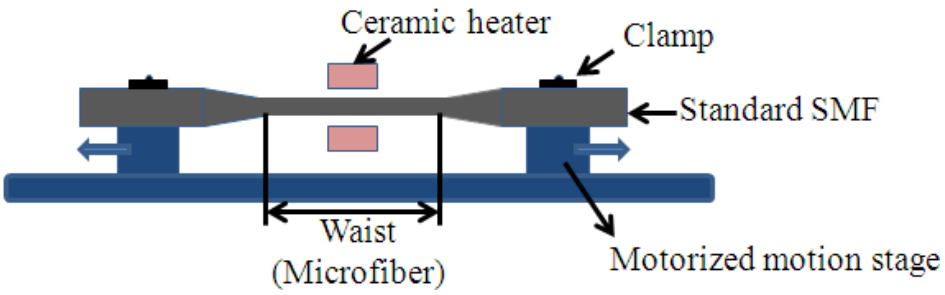

Fig. 4.10. Optical microfiber fabrication setup.

Initially to form the substrate a silver film with an approximate thickness of 50 nm was deposited onto a glass slide with an approximate length of 2.5 mm using a sputter coater (Q150R, Quorum), where the thickness of the Ag film was controlled by setting the deposition rate and time.

Then a tapered microfiber (i.e. with a uniform waist of 4 μm) was carefully cleaved so that it had a length slightly longer than that of the substrate, in effect there was approximately 3 mm

of overhang at each end of the substrate. A tapered fiber probe was temporarily used to position the microfiber on the substrate with the aid of two 800X microscopes for visualisation.

The spectral response of the TE-pass polarizer was then measured using a non-contact end-fiber coupling scheme [21]. Fig. 4.11 (a) and (b) show the measurement setup and a microscope image of the sample (the diameter of the microfiber is 4 μm). An end-fiber coupling scheme was used as shown in Fig 4.11 (c).

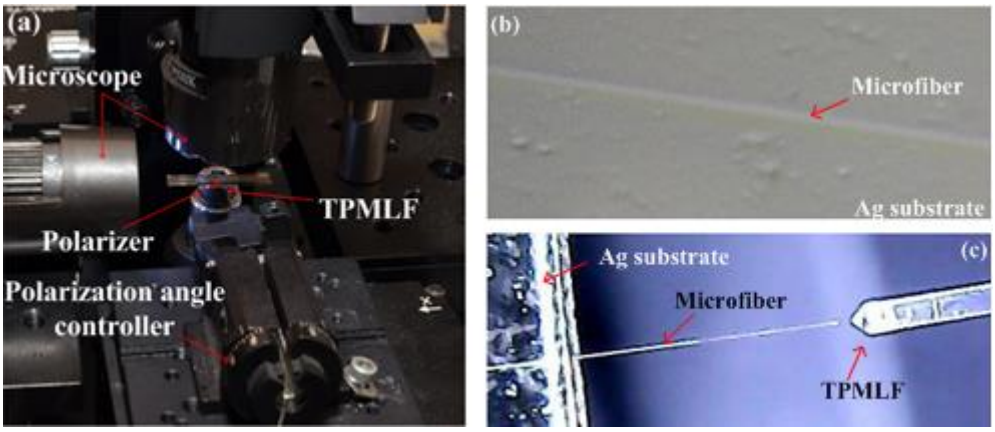

Fig. 4.11. (a) Experiment setup for measurement of transmission. (b) Microscope image of the fabricated microfiber placed on top of an Ag substrate. (c) Microscope image of the end-fiber coupling scheme.

Fig. 4.12 schematically shows the experiment setup. Light from a broadband laser was injected into a polarization controller (PC) (PC-FFB, Thorlabs) through a single mode fiber (SMF), and then coupled to a tapered polarization maintaining lensed fiber (TPMLF) (TPMJ, OZ Optics) with which had a specified focal spot diameter of 6μm. The TPMLF was then aligned to launch light to the fabricated microfiber polarizer sample. Similarly, the output light from the device was coupled into another "receiving" TPMLF, with the same specification as the launch TPMLF, the output of which was connected to an optical spectrum analyzer (OSA) (86142B, Agilent).

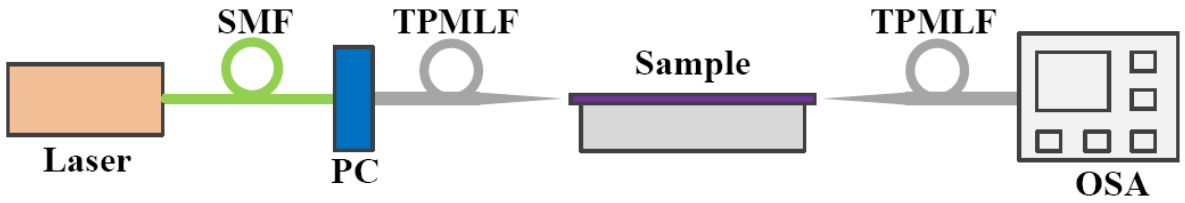

Fig. 4.12. Schematic diagram of the experiment setup. SMF = single mode fiber, PC = polarization controller, TPMLF = tapered polarization maintaining lensed fiber, OSA = optical spectrum analyzer.

Before the Ag substrate plus microfiber taper section structure was characterized, a low refractive index material coated substrate was used temporarily as a substitute for the Ag coated substrate, using the same microfiber to be used later with the Ag coated substrate. With this low RI substrate, a reference was established where no SPPs could exist. In the experiment, the low refractive index coated substrate was made by spin coating a polymer material (PC-363L, Luvantix) which has a low refractive index (~ 1.36 at wavelength 1550 nm) on to a glass slide.

Fig. 4.13 (a) shows the normalized measured spectra of the fabricated TE-pass polarizer. It can be seen that the loss of TM mode is much higher than that of the TE mode i.e. a large extinction ratio (> 20 dB) was achieved, as expected from the calculation results discussed above. By comparing results shown in Fig. 4.13 (a) and Fig. 4.9 (a), it can be found that they agree well. However the measured transmission loss is a few dB higher than the calculated results, which might be due to: 1) the scattering loss induced by roughness of the silver surface; 2) microfiber fabrication error: for example, fabrication of a microfiber with a diameter less than 4 μm could result in a larger insertion loss; 3) non-ideal microfiber's placement as shown in the inset of Fig. 4.13 (a) resulting in the actual length of the polarizer being longer than 3 mm.

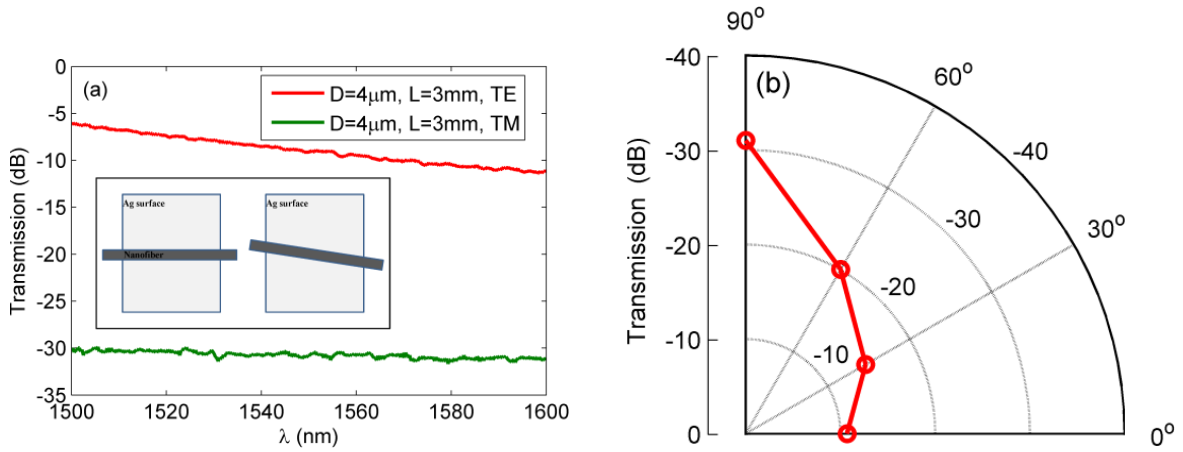

Fig. 4.13. (a) Measured transmission spectra for TM and TE modes with dimensions of *D* and *L*. (b) Polar image of the measured transmission for different polarization angles measured at 1550 nm for *D* = 4 μm and *L* = 3 mm.

Fig. 4.13 (b) exhibits the measured transmission dependence versus polarization angle for the polarizer with *D* = 4 μm and *L* = 3 mm. Here 0^o polarization is defined as the TE mode (i.e. with an electric field parallel to the metal surface). The highest transmission is observed for 0^o polarization (TE mode), and the transmission decreases gradually as the polarization angle increases. This experimental result confirms that the structure can operate successfully as a TE-pass polarizer.

4.4 Summary

In this chapter the design of a novel LRDLSPPs based waveguide structure offering a better trade-off between the propagation length and mode confinement, compared to the conventional LRDLSPPs configuration has been presented. The proposed structure can significantly improve the propagation length for the same mode confinement capacity, or can realize a much tighter field confinement for the same propagation length. The structure offers flexible solutions for the development of compact hybrid plasmonic devices by the appropriate selection of structural parameters.

Furthermore based on the polarization selectivity of the loss characteristics of the SPPs mode, this chapter also demonstrated a novel plasmonic TE-pass polarizer which consists of an optical microfiber placed on a glass substrate coated with a silver layer. For this structure, the TM mode in the microfiber is coupled to the surface plasmon mode with a portion of energy located on the metal surface resulting in a large propagation loss. However the TE mode will not couple to the surface plasmon mode and thus most of the energy will be confined in the microfiber resulting in a relatively low loss. Both the numerical simulation and experimental results have shown that the extinction ratio of a 3 mm-long polarizer is greater than 20 dB over the wavelength range from 1500 nm to 1600 nm.

4.5 References

1. T. Holmgaard, and S. I. Bozhevolnyi, Theoretical analysis of dielectric-loaded surface plasmon-polariton waveguides, *Phys. Rev. B.*, 75, pp. 245405, (2007).
2. T. Holmgaard, Z. Chen, S. I. Bozhevolnyi, L. Markey, A. Dereux, A.V. Krasavin, and A. V. Zayats, Wavelength selection by dielectric-loaded plasmonic components, *Appl. Phys. Lett.*, 94, pp. 051111, (2009).
3. J. Gosciniak, L. Markey, A. Dereux, and S. I. Bozhevolnyi, Thermo-optic control of dielectric-loaded plasmonic Mach-Zehnder interferometers and directional coupler switches, *Nanotechnology*, 23, pp. 444008, (2012).
4. B. F. Yun, G. H. Hu, and Y. P. Cui, Bound modes analysis of symmetric dielectric loaded surface plasmon-polariton waveguides, *Opt. Express*, 17 (5), pp. 3610-3618, (2009).
5. T. Holmgaard, J. Gosciniak, S. I. Bozhevolnyi, Long-range dielectric-loaded surface plasmon polariton waveguides, *Opt. Express*, 18 (22), pp. 23009-23015, (2010).
6. X. Q. Wu, and L. M. Tong, Optical microfibers and nanofibers, *Nanophotonics*, 2, pp.

407-428, (2013).

7. J. J. Chen, Z. Li, S. Yue, and Q. H. Gong, Hybrid long-range surface Plasmon-polariton modes with tight field confinement guided by asymmetrical waveguides, *Opt express*, 17, pp. 23603-23609, (2009).
8. V. S. Volkov, Z. Han, M. G. Nielsen, K. Leosson, H. Keshmiri, J. Gosciniak, O. Albrektsen, S. I. Bozhevolnyi, Long-range dielectric-loaded surface plasmon polariton waveguides operating at telecommunication wavelengths, *Opt. Lett.*, 36, pp. 4278-4280, (2011).
9. X. H, Sun, L. P. Xia, J. L. Du, S. Y. Yin, C. L. Du, A hybrid long-range surface plasmon waveguide comprising a narrow metal stripe surrounded by the low-index dielectric regions, *Opt. Commun.*, 285, pp. 4359–4363, (2012).
10. D. X. Dai, and S. L. He, A silicon-based hybrid plasmonic waveguide with a metal cap for a nano-scale light confinement, *Opt express*, 17, pp. 16646-16653, (2009).
11. D. Dai, J. Bauters, and J. E. Bowers, Passive Technologies for Future Large-Scale Photonic Integrated Circuits on Silicon: Polarization Handling, Light Non-Reciprocity, and Loss Reduction, *Light Sci. Appl.*, 1, pp. 1-14, (2012).
12. Y. Q. Ma, G. Farrell, Y. Semenova, and Q. Wu, Low loss, high extinction ratio and ultra-compact plasmonic polarization beam splitter, *Photon. Technol. Lett.*, 26, pp. 660-663, (2014).
13. J. Chee, S. Y. Zhu, and G. Q. Lo, CMOS compatible polarization splitter using hybrid plasmonic waveguide, *Opt. Express*, 20, pp. 25345-25355, (2012).
14. M. N. Abbs, C. W. Cheng, Y. C. Chang, and M. H. Shih, An omni-directional mid-infrared tunable plasmonic polarization filter, *Nanotechnology*, 23, pp. 444007, (2012).

15. Y. Wakabayashi, J. J. Yamauchi, and H. Nakano, A TM-pass/TE-stop polarizer based on a surface plasmon resonance, *Adv. Optoelectron.*, 2011, pp. 867271, (2011).
16. X. Sun, M. Z. Alam, S. J. Wagner, J. S. Aitchison, and M. Mojahedi, Experimental demonstration of a hybrid plasmonic transverse electric pass polarizer for a silicon-on-insulator platform, *Opt. Lett.*, 37, pp. 4814-4816, (2012).
17. H. Malitson, Interspecimen Comparison of the Refractive Index of Fused Silica, *JOSA.*, 55 (10), pp. 1205-1208, (1965).
18. E. D. Palik, Handbook of Optical Constants of Solids, (Academic, 1998).
19. A. Kumar, J. Gosciniak, V. S. Volkov, S. Papaioannou, D. Kalavrouziotis, K. Vyrsokinos, J. C. Weeber, et. al., Dielectric-loaded plasmonic waveguide components:Going practical, *Laser Photonics Rev.*, 6, pp. 938-951, (2013).
20. R. F. Oulton, V. J. Sorger, D. A. Genov, D. F. P. Pile and X. Zhang, A hybrid plasmonic waveguide for subwavelength confinement and long-range propagation, *Nat. Photon.*, 2, pp. 496-500, (2008).
21. X . Sun, M. Z. Alam, J. S. Aitchison, and M. Mojahedi, Experimnetal demonstration of a hybri plasmonic TE-pass polarizer for silicon-on-insulator platform, *Opt. Lett.*, 37, pp. 4814-4816, (2012).

Chapter 5: Hybrid plasmonic waveguide devices

5.1 Introduction

Due to the potential for guiding light beyond the diffraction limit, SPPs are attractive candidates for applications in highly integrated photonic circuits (IPCs). However, high loss is inherent in the metal optics and it further increases when the mode sizes are downscaled into the subwavelength level. Therefore the critical challenge in practical SPPs based IPC implementations is how to increase the propagation length while achieving a tight mode confinement with at least subwavelength scale, or in other words, effectively balance the tradeoff between the propagation length and mode confinement.

Discussions in the previous chapters have shown that compared to traditional plasmonic waveguides, such as the MIM and IMI configurations, the DLSPPs waveguide could offer a better tradeoff, but the level of its mode confinement is still low with the mode area around $0.16\lambda^2$ [1].

In order to further achieve an optimum tradeoff, in this chapter, two novel hybrid SPPs (HSPPs) waveguides are proposed and investigated: a long range nanowedge HSPPs (LRWHSPPs) waveguide and a long range wedge-to-wedge HSPPs (LRWWHSPPs) waveguide.

5.2 A LRWHSPPs waveguide for low loss propagation with a deep-subwavelength mode confinement

It is a challenge to develop novel plasmonic waveguides which can simultaneously offer both

subwavelength mode confinement and long propagation length. To address this challenge, R. F. Oulton *et. al.* firstly proposed a novel HSPPs waveguide, as shown in Figs. 5.1 (a-b), which was published in *Nature* in 2008 [2].

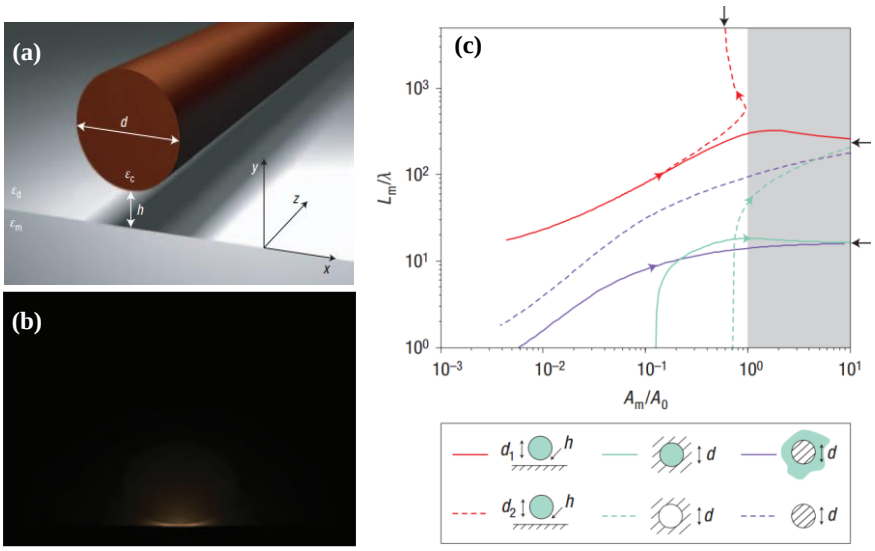

Fig. 5.1. (a) Schematic view of the HSPPs waveguide reported in Ref. 2 which consists of a GaAs cylinder nanowire separated from a silver substrate by a nanoscale SiO_2 gap. (b) Electromagnetic energy density distribution. (c) A plot of normalized mode area versus normalized propagation length enables a comparison of various plasmonic waveguides [2].

As shown in Figs. 5.1 (a), an HSPPs waveguide typically consists of a low refractive index (LRI) dielectric nanoscale gap which separates the metal layer and the high refractive index (HRI) dielectric waveguide. By optimizing the SPPs waveguide structural parameters, a low loss HSPPs mode (propagation length ranges from 40 μm to150 μm) can be excited due to the interference between the dielectric waveguide mode and SPPs mode, and the HSPPs modes will propagate within the LRI dielectric gap with a tight mode confinement (the mode area ranges from $\lambda^2/400$ to $\lambda^2/40$). Because of its superior capacity for guiding light, many HSPPs based devices such as plasmonic nanolasers [3-5], nanotweezers [6-7], ring resonators [8], polarization beam splitters [9] and directional couplers [10] have been proposed and demonstrated.

Although this HSPPs waveguide could offer a subwavelength mode confinement (the mode area ranges from $\lambda^2/400$ to $\lambda^2/40$), it still suffers the disadvantage of a short propagation length which typically ranges from 40 μm to 150 μm.

To further mitigate this tradeoff, researchers have proposed the modification of the structure of the HSPPs waveguide so it becomes symmetrical [11] (as shown in Fig. 5.2 (a)), referred to as a long range HSPPs (LRHSPPs) waveguide, or to combine the HSPPs waveguide with the traditional plasmonic configurations, such as a metal V-groove [12-13] (VGHSPPs, as shown in Fig. 5.2 (b)) and a metal wedge [14-15] (WHSPPs, as shown in Fig. 5.2 (c)). For example, a novel LRHSPPs waveguide consisting of two dielectric nanowires symmetrically placed on each side of a thin metal film has been demonstrated [11], and it was shown that for the same level of mode confinement, the propagation length for the LRHSPPs waveguide is one order of magnitude larger than that of the HSPPs waveguide described above. In addition, a WHSPPs structure utilizing a triangular metal wedge as the substrate has been proposed and investigated. The results illustrate that for the same propagation length, the WHSPPs waveguide shows a much stronger mode confinement compared to the HSPPs waveguide [15] above.

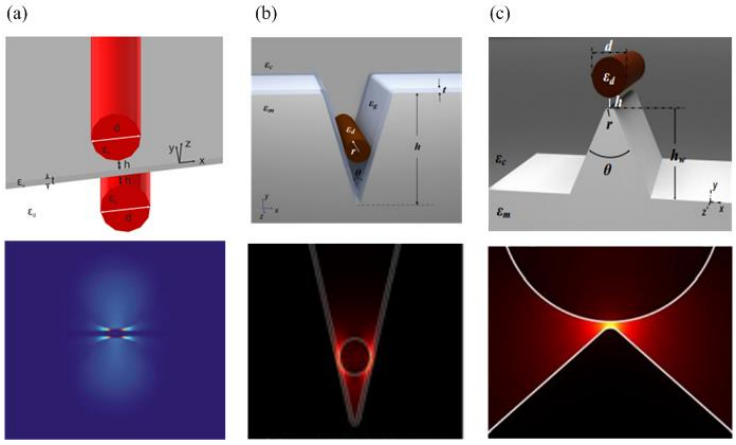

Fig. 5.2. Modified HSPPs based waveguides reported in (a) Ref. 11, (b) Ref. 12 and (c) Ref. 15 with corresponding electromagnetic energy density distributions.

Compared to the HSPPs waveguide, the LRHSPPs waveguide achieves an extended propagation length at the cost of relatively weaker mode confinement, while the WHSPPs waveguide realizes stronger mode confinement accompanied by a shorter propagation length. In order to simultaneously achieve both a longer propagation length and a higher level of mode confinement, a novel SPPs waveguide structure involving the combination of the LRHSPPs and WHSPPs waveguides is proposed and investigated in this chapter, referred to as the LRWHSPPs waveguide, as show in Fig. 5.3. The LRWHSPPs waveguide consists of a thin silver (Ag) film with two identical nanowedges embedded in a low permittivity silica (SiO_2) cladding. The two high permittivity silicon (Si) nanowires are placed symmetrically near the upper and lower Ag nanowedges with a small gap *g*. The diameter of the Si nanowire is *H* and the thickness of the Ag film is *d*. The Ag wedge has a height of *h*, and the wedge tip has an angle of θ.

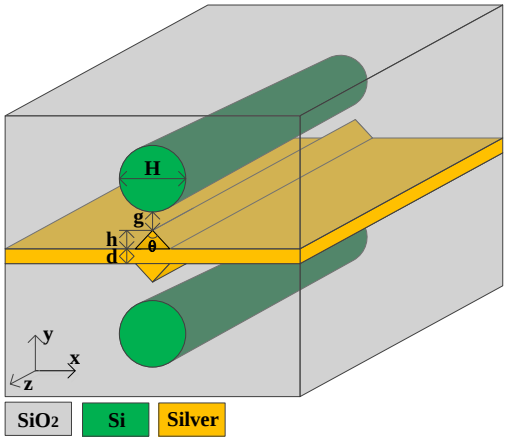

Fig. 5.3. Schematic view of the proposed LRWHSPPs waveguide.

The characteristics of the LRWHSPPs mode, the propagation length L_p (as seen from eq. (2.34) in Chapter 2) and the normalized mode area *A* (as seen from eq. (2.35) in Chapter 2), are investigated at the wavelength λ = 1550 nm by means of an FEM. The corresponding permittivities of Si, SiO_2 and Ag used are 12.25, 2.25 and -129+3.3*i* [16], respectively.

5.2.1 Influence of structural parameters on LRWHSPPs mode characteristics

The influence of the tip angle θ and the gap g on the mode properties of the waveguide is firstly investigated. Fig. 5.4 (a) and (b) shows the dependence of the normalized mode area and the propagation length, respectively, on the tip angle θ with the gap g. In this simulation, the parameters used are d = 10 nm, H = 200 nm and h = 5 nm. As shown in Figs. 5.4 (a-b), with an increase in the tip angle θ, the normalized mode area A increases monotonically, while the propagation length L_p is shown to increase at first and then decrease, exhibiting maximum values at certain tip angles (i.e. around 100°.

The propagation length could be further increased by increasing the gap distance between the Ag nanowedge and upper (lower) waveguides, but at the expense of weaker mode confinement. To examine this in detail the normalized electromagnetic (EM) energy density distributions related to points *c* (g = 2 nm, θ = 100°), *d* (g = 10 nm, θ = 100°), *e* (g = 2 nm, θ = 160°) and *f* (g = 2 nm, θ = 20°) in Fig. 5.4 (b) are plotted in Fig. 5.4 (c), (d), (e) and (f), respectively. From Figs. 5.4 (c-f) it is clear that the light is tightly confined around the Ag nanowedge tip regions. From Figs. 5.4 (c, d) it can be seen that for the same Ag nanowedge tip angle, an increase in the gap distance will lower the mode confinement. Figs. 5.4 (c, e) show that for the same gap distance, there is an optimum Ag nanowedge tip angle of 100 degrees which results in a maximum propagation length. If the Ag nanowedge tip angle is larger than 100 degrees, a greater proportion of the electric field spreads laterally along the metal wedge, leading to a significantly increased mode area, resulting in a larger portion of power distributed in the metal region giving rise to a larger metallic dissipation, and thus a shorter propagation length. For a small Ag nanowedge tip angle (less than 100 degrees), the wedge-like mode will dominate the mode distribution and will result in relatively high loss [17], as shown in Fig. 5.4 (f) where the mode is highly localized around the Ag nanowedge tip. This will also result in a shorter propagation length. In order to explain the propagation length behavior more clearly, the ratio of the

power distribution in the metal region compared to the total power of the waveguide ROP_{metal} (with g = 5 nm) is investigated and shown in Fig. 5.4 (b). As shown in Fig. 5.4 (b) (purple curve), for a tip angle such as 100 degrees, a relatively small portion of the power is distributed in the metal region (hence smaller loss) resulting in a longer propagation length compared to that for other Ag nanowedge tip angles.

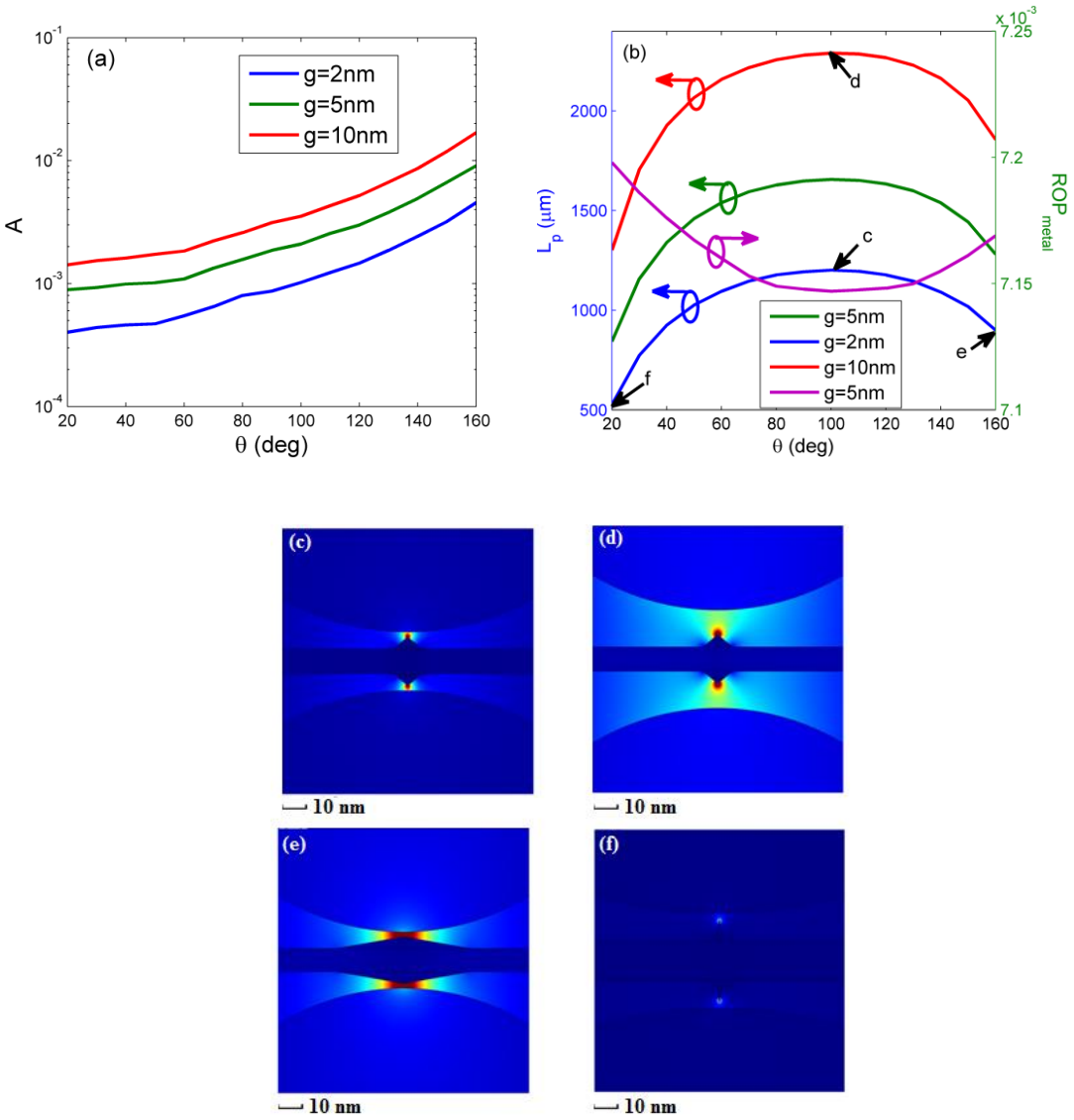

Fig. 5.4. Dependences of the LRWHSPPs mode properties of the proposed structure at the wavelength of 1550 nm. (a) The normalized mode area A; (b) the propagation length L_p and the ratio of power inside the metal region ROP_{metal}. EM density patterns for (c) [g = 2 nm, θ = 100°], (d) [g = 10 nm, θ = 100°], (e) [g = 2 nm, θ = 160°] and (f) [g = 2 nm, θ = 20°].

The LRWHSPPs mode properties are also dependent on the cladding layer material. It is important to investigate this because such a dependency offers the possibility of enabling thermo- or electro-optic control of a device or the use of such a device for sensing applications. Fig. 5.5 shows the simulated propagation length L_p and normalized mode area A versus the refractive index (RI) of the cladding layer material. In this simulation, the waveguide parameters are defined as follows: d = 10 nm, H = 200 nm, h = 5 nm, g = 5 nm and θ = 100°. From Fig. 5.5 it is noted that as the RI of the cladding material increases from 1 to 2.5, the normalized mode area A increases from 0.0015 to 0.006, while the propagation length L_p decreases from 3008 μm to 1339 μm. The result indicates that a lower RI for the cladding material not only extends the propagation length but also results in an improvement of mode confinement.

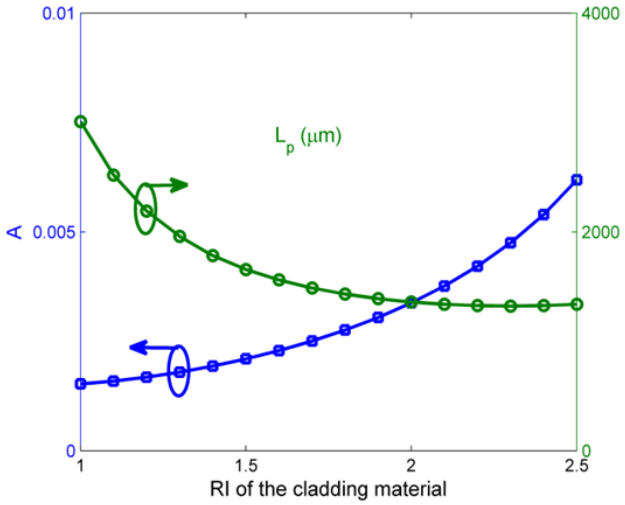

Fig. 5.5. The LRWHSPPs mode properties as a function of the RI of the cladding layer material.

The results discussed above suggest that the LRWHSPPs waveguide could offer a very useful capability for low loss (propagation length ranges from 1200 μm to 3500 μm) and deep-subwavelength (mode area ranges from $\lambda^2/4000$ to $\lambda^2/400$) light guiding with the appropriate structural parameters.

5.2.2 LRWHSPPs performance comparison with existing HSPPs waveguides

To quantitatively demonstrate the advantages of the LRWHSPPs waveguide, Fig. 5.6 (a) shows a comparison of the proposed LRWHSPPs waveguide with the HSPPs waveguide studied in [2], the LRHSPPs waveguide investigated in [11], the WHSPPs waveguide reported in [15], the recently reported bow-tie hybrid SPPs (BTHSPPs) waveguide in [18], and a symmetric version of BTHSPPs (SBTHSPPs). The symmetric version of BTHSPPs is based on a variation of the work published in [18], which considered only an asymmetric waveguide.

Cross-section views of the LRWHSPPs, LRHSPPs, WHSPPs, BTHSPPs, SBTHSPPs and HSPPs waveguides are depicted in Fig. 5.6 (b). The counterpart parameters used in the simulations are: for the LRWHSPPs waveguide, $\theta = \alpha = 100°$, $d = 10$ nm, $h = 5$ nm and $H = 200$ nm; for the LRHSPPs waveguide, $d = 10$ nm, and $H = 200$ nm [11]; for the WHSPPs waveguide, $H = 200$ nm, $h = 5$ nm and $\theta = 130°$ [15]; for the BTHSPPs and SBTHSPPs waveguides, $h = 20$ nm, $H = 40$ nm, $d = 10$ nm, $W = L = 200$ nm, $\theta = \alpha = 60°$ [18]; for the HSPPs waveguide, $H = 200$ nm [2].

From Fig. 5.6 (a) it is clearly seen that the LRWHSPPs waveguide has better performance compared to previously reported LRHSPPs, WHSPPs, BTHSPPs, SBTHSPPs and HSPPs waveguides [2, 11, 15, 18]. In particular, by comparison to the HSPPs waveguide reported in Ref. 2, the mode confinement and the propagation length of the LRWHSPPs waveguide demonstrates at least a 5-fold and 60-fold enhancement respectively. Compared to the WHSPPs reported in Ref. 15, the LRWHSPPs waveguide has relatively worse mode confinement (twice the mode area for the same gap g), but has 40 times longer propagation length. In addition, the propagation lengths for both LRWHSPPs and LRHSPPs waveguides (reported in Ref. 11) are almost the same, but the normalized mode area of the LRWHSPPs waveguide is one order of magnitude smaller than that of LRHSPPs

waveguide, indicating that the LRWHSPPs waveguide has a much better mode confinement. Finally, compared to the BTHSPPs (SBTHSPPs) waveguide in [18], the rectangular slot between the Si waveguide and Ag substrate is eliminated for the LRWHSPPs waveguide, which effectively provides a smaller mode area and longer propagation length (a smaller portion of energy contacts with Ag). The mode confinement and propagation length of the LRWHSPPs waveguide respectively demonstrates at least a 3-fold (6-fold) and 30-fold (1.5-fold) enhancement compared to that of the BTHSPPs (SBTHSPPs) waveguide.

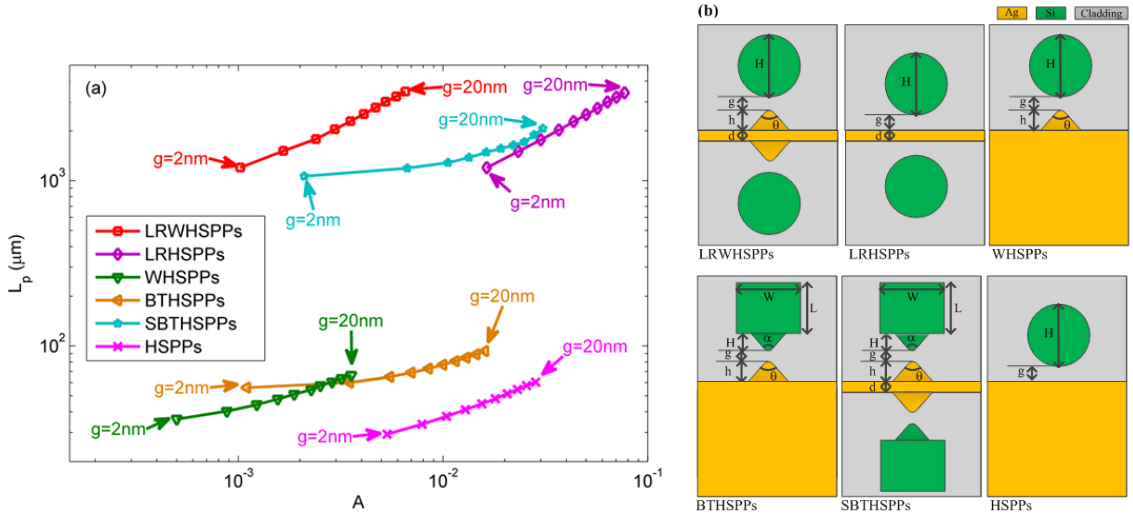

Fig. 5.6. (a) Plot of the normalized mode area versus the propagation length for the LRWHSPPs, LRHSPPs, WHSPPs, BTHSPPs, SBTHSPPs and HSPPs waveguides with different structure parameters. (b) Cross-section views of the LRWHSPPs, LRHSPPs, WHSPPs, BTHSPPs, SBTHSPPs and HSPPs waveguides.

5.2.3 Proposed fabrication

Any future device requires fabrication, and fabrication tolerance plays a major part in preparing for fabrication. Thus in this section, the likely practical fabrication process is discussed with the objective of considering the fabrication tolerance required.

5.2.3.1 Fabrication process

It is useful to consider the fabrication steps that would be needed for the preparation of actual devices, with the objective of using the model developed to examine the tolerance of the design to fabrication errors. The likely fabrication steps for the LRWHSPPs waveguide are shown schematically in Fig. 5.7.

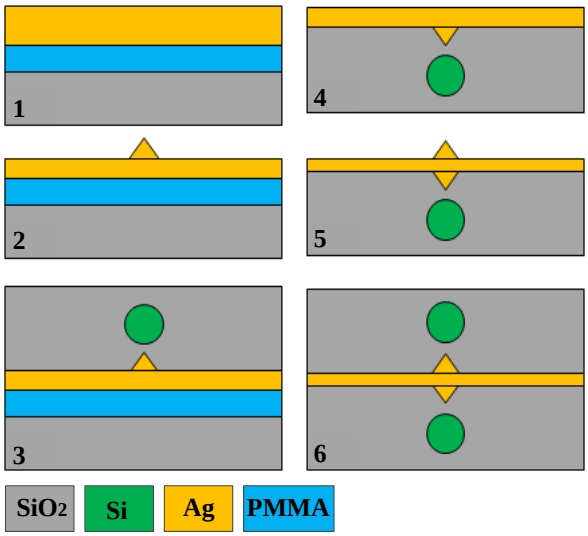

Fig. 5.7. Schematic diagram of the proposed sequence of the fabrication.

The process involves: (1) Fabrication of a three-layer structure, i.e. PMMA and silver layers successively coated on a silica substrate; (2) The nanowedge could then be formed by the focused ion beam (FIB) technique [19]; (3) The Si nanowire could be produced by the "vapor-liquid-solid" method and covered by a silica cladding [20]; (4) The PMMA layer could be dissolved in acetone leaving the exposed silver film [21]; (5-6) Repeating the steps (2) and (3) would complete the proposed structure.

5.2.3.2 Fabrication tolerances

During fabrication, it is a challenge to achieve precise alignment between the nanowire and nanowedge. Therefore it is important to investigate the influence of the misalignment

between the nanowedges and waveguides as a result of fabrication errors on the mode properties of the structure. Fig. 5.8 (a) depicts two possible fabrication misalignment cases labelled (1) and (2) with misalignment distances *S*. The details are:

Case 1: both nanowedges are aligned with each other but are off-center relative to the nanowires.

Case 2: the nanowires are not aligned with each other and also not aligned to the nanowedges.

The results of this study are presented in Fig. 5.8 (b). The waveguide parameters used in the simulations are given as follows: d = 10 nm, H = 200 nm, h = 5 nm, g = 5 nm and θ = 100°. From Fig. 5.8 (b) it can be seen that both the propagation length and the normalized mode area increase as the misalignment distance *S* increases. This could possibly be due to the fact that the misalignment alters the longitudinal mode confinement, i.e. the mode area will be increased, or in other words, more mode energy will spread out of the gap region, which leads to a smaller portion of the mode energy concentrating around the metal wedge, thereby increasing the propagation length. But these increases are modest, for example if the value of *S* varies within 10 nm, the propagation length and the normalized mode area experience less than a 2% and 7% variation, respectively. The corresponding normalized electromagnetic energy density distributions are also shown in the insets of Fig. 5.8 (b). It is observed that the modifications to the mode profile are negligible. The results indicate that the proposed LRWHSPPs waveguide has a good tolerance to fabrication errors involving misalignment.

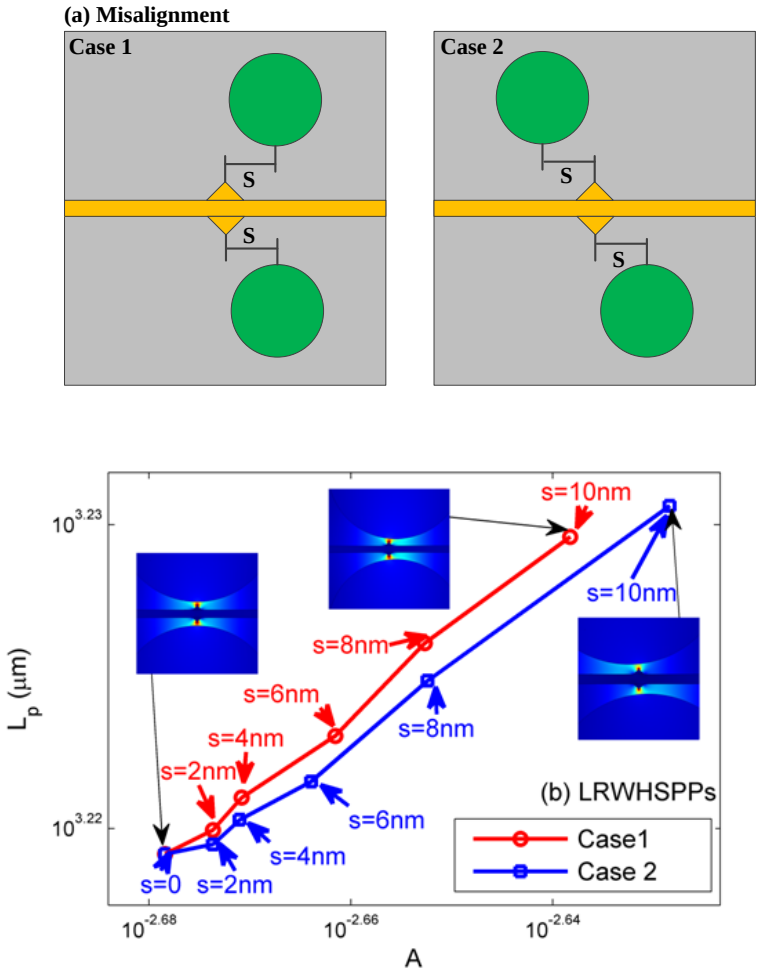

Fig. 5.8. (a) Schematic views of two types of misalignment cases considered. (b) The influence of the alignment perturbation on the LRWHSPPs mode properties. Insets: the normalized EM density distributions.

There are other fabrication constraints, for example in practice it is very difficult to fabricate an ideal sharp tip nanowedge, therefore in reality the fabricated nanowedge has a marginally round tip (as shown in the inset of Fig. 5.9). It is important therefore to investigate the influence of the radius of curvature of the nanowedge tip on its mode properties and the simulation results are shown in Figure 5.9. The waveguide parameters used in the simulation are given as follows: d = 10 nm, H = 200 nm, h = 5 nm, g = 5 nm and θ = 100°. The calculations shown in Fig 5.9 reveal that the normalized mode area increases by 11% when the tip curvature increases from 0 nm to 30 nm, while the propagation length decreases by 2% compared to that for an ideally sharp tip.

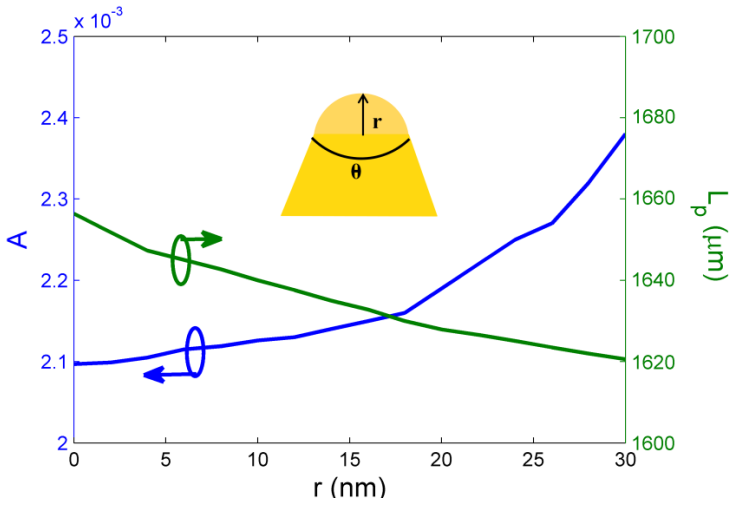

Fig. 5.9. LRWHSPPs mode properties versus the curvature radius of the nanowedge rounded tip.

The results discussed above demonstrate that the proposed LRWHSPPs waveguide not only possesses a remarkable guiding performance (it is capable of confining light in a deep-subwavelength region ranging from $\lambda^2/4000$ to $\lambda^2/400$ with a long propagation length ranging from 1200 to 3500 μm), but also show an acceptable tolerance to fabrication errors and other constraints.

5.3 A LRWWHSPPs waveguide with low loss propagation and ultra-deep-subwavelength mode confinement

Considering the fact that for a wedge dielectric waveguide, the light energy is strongly localized near the apex of the wedge due to the tip field enhancement [22], it is expected that improvements in enhanced mode confinement can be achieved if the nanowires in the LRWHSPPs waveguide are replaced by nanowedges. Therefore based on the LRWHSPPs waveguide, a novel LRWWHSPPs waveguide is proposed and shown in Fig. 5.10. Compared to the LRWHSPPs waveguide, two identical Si wedge waveguides are introduced for the LRWWHSPPs waveguide. The Si wedge has a height of *H*, and the wedge tip has an angle of

α. Considering the practical fabrication constraints, the wedge tip of both Ag nanowedge and Si wedge are assumed to have a curvature radius of r = 10 nm.

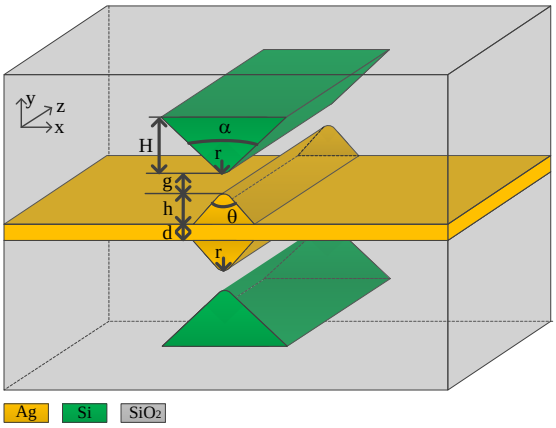

Fig. 5.10. Schematic view of the LRWWHSPPs waveguide.

5.3.1 Influence of structural parameters on LRWWHSPPs mode characteristics

Before studying the influence of the structural parameters on the LRWWHSPPs mode properties, it is useful to define the so-called mode character (*MC*) defined as follows [2]:

$$MC = \frac{n_{\text{eff}} - n_{\text{eff:LRSPPs}}}{(n_{\text{eff}} - n_{\text{eff:LRSPPs}}) + (n_{\text{eff}} - n_{\text{eff:SiWG}})} \qquad (5.1)$$

where n_{eff}, $n_{\text{eff:SiWG}}$ and $n_{\text{eff:LRSPPs}}$ are the effective refractive indices of the LRWWHSPPs mode, Si waveguide (SiWG) mode and LRSPPs mode (supported by the structures without the Si waveguides), respectively. The *MC* parameter can be used to evaluate the mode hybridization character, or in other words, the degree to which the LRWWHSPPs mode is SiWG-like (i.e. $n_{\text{eff:SiWG}} > n_{\text{eff:LRSPPs}}$ i.e. $MC > 0.5$) or LRSPPs-like (i.e. $n_{\text{eff:LRSPPs}} > n_{\text{eff:SiWG}}$ i.e. $MC < 0.5$).

Fig. 5.11 (a) and (b) respectively show the dependence of the propagation length L_p and the normalized mode area A on the Si wedge height H (which determines the value of $n_{\text{eff:SiWG}}$) with the gap g. The parameters used in this simulation are d = 10 nm, h = 5 nm and θ = 100°,

which are the optimized values presented for the above LRWHSPPs waveguide. In addition α is set to be 100°. As shown in Fig. 5.11 (a) and (b), both L_p and A decrease with an increase in H at first but then increase, which illustrates that there is a minimum value for both L_p and A at certain H values (i.e. around 200 nm). For smaller Si wedges (H < 200 nm), the hybrid mode is dominated by the LRSPPs mode (MC < 0.5, shown in Fig. 5.11 (c)). Hence, the LRWWHSPPs mode, which is the LRSPPs-like mode (the related normalized energy density distributions are shown in Figs. 5.11 (d, e)), realizes a longer propagation length but at a cost of a weaker mode confinement due to the nature of LRSPPs mode. When the size of the Si wedges increases to a certain level (that is for H > 200 nm), the LRWWHSPPs mode behaves as a low loss SiWG mode (MC > 0.5), or in other words, most of the mode energy tends to be confined inside the Si dielectric wedge cores (Figs. 5.11 (h, i)) resulting in a larger mode area and relatively low propagation loss. At the minimum value of L_p or A ($H \sim$ 200 nm) it is found that MC = 0.5 (Fig. 5.11 (c)) indicates $n_{\text{eff:SiWG}} = n_{\text{eff:LRSPPs}}$. In this case neither the SiWG nor LRSPPs mode dominate – resulting in a novel hybrid plasmonic mode that features the characteristics of both the SiWG and LRSPPs modes (Figs. 5.11 (f)). More interestingly, as the gap decreases to a few nanometers, a large portion of the mode energy becomes strongly confined within the SiO_2 gap region only (Fig. 5.11 (g)). For example, when H = 200 nm and g varies from 2 nm to 25 nm, both a deep-subwavelength mode confinement (ranging from λ^2/10604 to λ^2/972) and a long propagation length (ranging from 1680 μm to 4724 μm) can be achieved. It is clear that the LRWWHSPPs waveguide offers a better tradeoff compared to the LRWHSPPs waveguide discussed above.

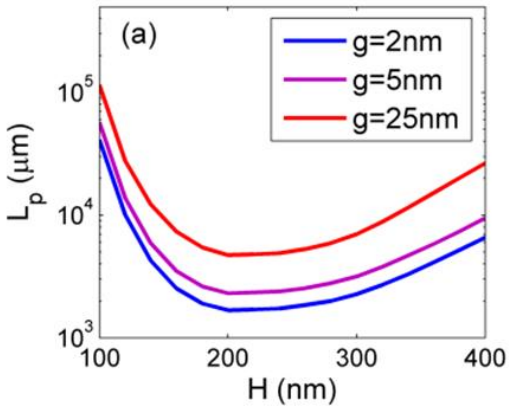
(a)
g=2nm
g=5nm
g=25nm
L_p (μm)
H (nm)

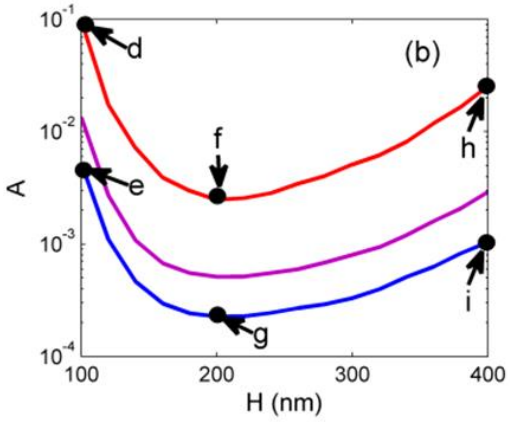
(b)
d
e
f
g
h
i
A
H (nm)

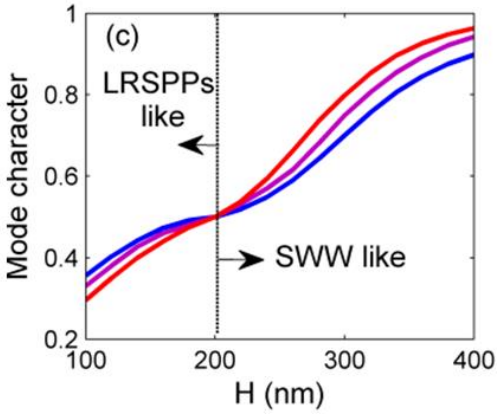
(c)
LRSPPs like
SWW like
Mode character
H (nm)

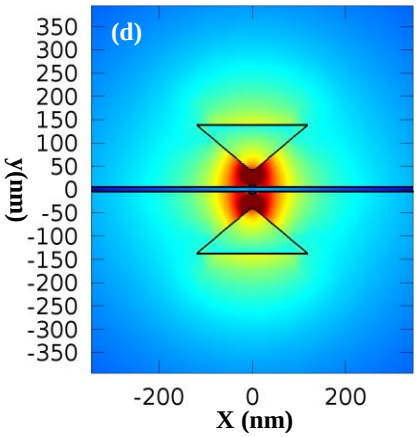
(d)
y(nm)
X (nm)

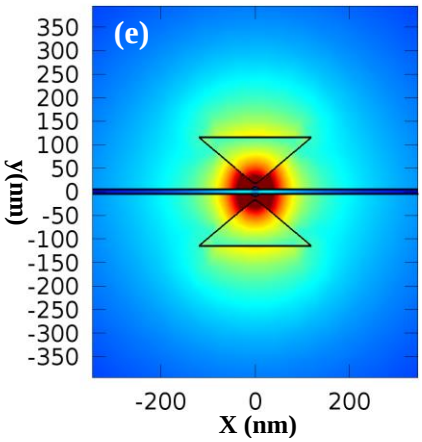
(e)
y(nm)
X (nm)

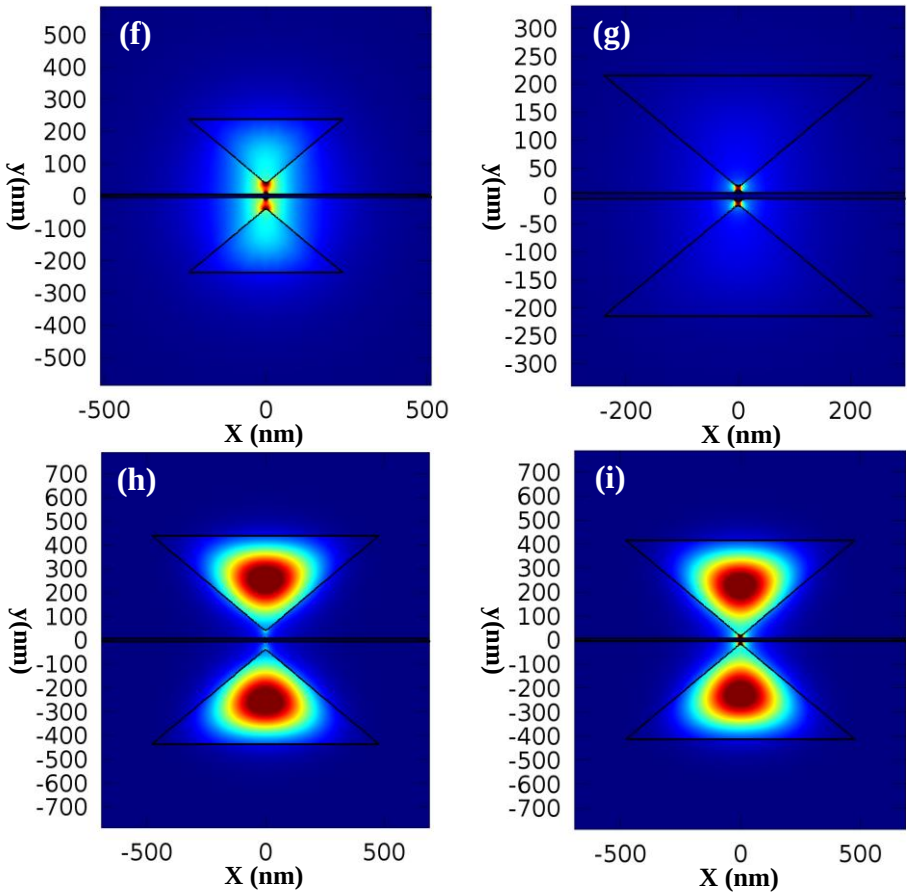

Fig. 5.11. (a) The propagation length L_p, (b) the normalized mode area A and (c) the mode character MC versus the height of Si wedge H with different gap g. (d-i) Normalized EM density distributions: (d) [H, g] = [100, 25] nm, (e) [H, g] = [100, 2] nm, (f) [H, g] = [200, 25] nm, (g) [H, g] = [200, 2] nm, (h) [H, g] = [400, 25] nm, and (i) [H, g] = [400, 2] nm.

The LRWWHSPPs mode characteristics are also dependent on the Si and Ag wedge tip angles of α and θ. Fig. 5.12 (a) and (b) respectively show the simulation results for the propagation length L_p and the normalized mode area A vs. different values of α and θ. The parameters used in this simulation are r = 10 nm, d = 10 nm, H = 200 nm, g = 5 nm and h = 5 nm. From Figs. 5.12 (a-b) it is known that as α increases, the propagation length decreases monotonically, while the normalized mode area is shown to decrease firstly and then increase, exhibiting a minimum value at around $\alpha = 100°$ for all the considered θ values. This could possibly be due to the fact that the varied Si wedge tip angle α gives rise to a different value of $n_{\text{eff:SiWG}}$, which will finally determine the character of the hybrid mode.

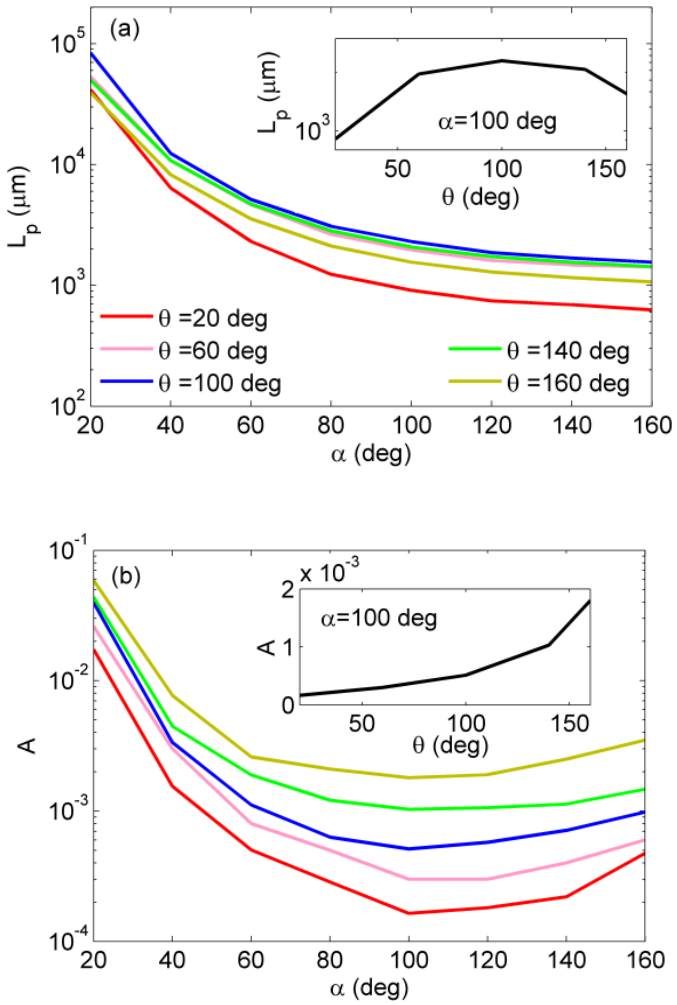

Fig. 5.12. (a) The propagation length L_p and (b) the normalized mode area A versus the Si wedge tip angle α with different Ag nanowedge tip angle θ. Inset in (a): the propagation length L_p versus the Ag nanowedge tip angle θ with fixed α at 100 deg. Inset in (b): the normalized mode area A versus the Ag nanowedge tip angle θ with fixed α at 100 deg

The calculated mode hybridization character is also shown in Fig. 5.13. From Fig. 5.13 it is easy to see that when α is smaller than 100°, the LRWWHSPPs mode is dominated by the LRSPPs mode corresponding to a long propagation length as well as the large mode area. When α is larger than 100°, the SiWG-like mode will dominate the mode hybridization and will result in relatively larger mode area.

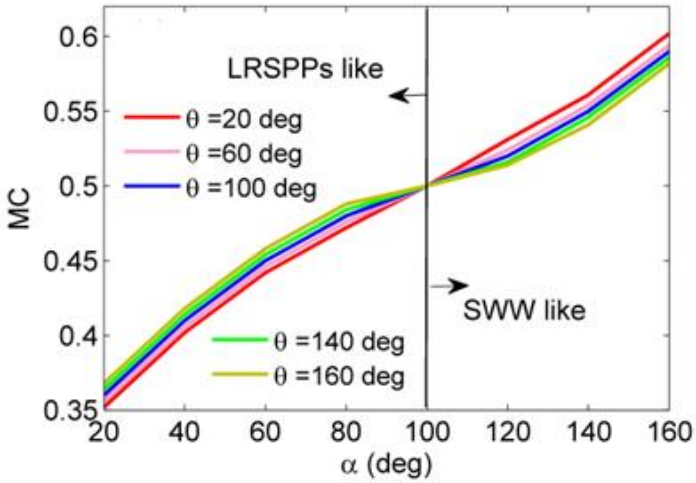

Fig. 5.13. The mode character *MC* versus the Si wedge tip angle α with different Ag nanowedge tip angle θ.

However from Fig. 5.12 (a) it can be found that as α increases beyond 100°, the propagation length of the SiWG-like mode still decreases, which is different from the result shown in Fig. 5.11 (a) (as increasing *H* from 200 nm). To better understand this physical mechanism, the normalized energy density distributions of the proposed LRWWHSPPs waveguide with different feature sizes are investigated and summarized in Fig. 5.14 (a). From Fig. 5.14 (a) it is easy to see that with the same value of α and larger value of *H* (i.e. *H* = 400 nm), the energy is better confined inside the dielectric Si wedge core, hence the propagation loss will accordingly decrease as shown in Fig. 5.11 (a). However with the same value of *H* and larger value of α (i.e. α = 160°), more energy spreads out of the dielectric Si wedge core, and hence a larger portion of power will be in contact with the metal resulting in a larger metal dissipation loss, thus the propagation length will accordingly become shorter as shown in Fig. 5.12 (a). Moreover, through the further observation in Figs. 5.12 (a-b), for all the considered α, it is found that the normalized mode area monotonically increases as θ increases, while the propagation length demonstrates a non-monotonic dependence on θ, indicating maximum values at certain tip angles (i.e., around $\theta = 100°$, as shown in the inset of Fig. 5.12 (a) for

$\alpha = 100°$). The normalized EM energy density distributions of the LRWWHSPPs waveguide with different value of θ are shown in Fig. 5.14 (b). The influence of the Ag wedge tip angle θ on the LRWWHSPPs mode properties and the energy density distributions are similar as that for the LRWHSPPs waveguide studied above, which contains detailed interpretations.

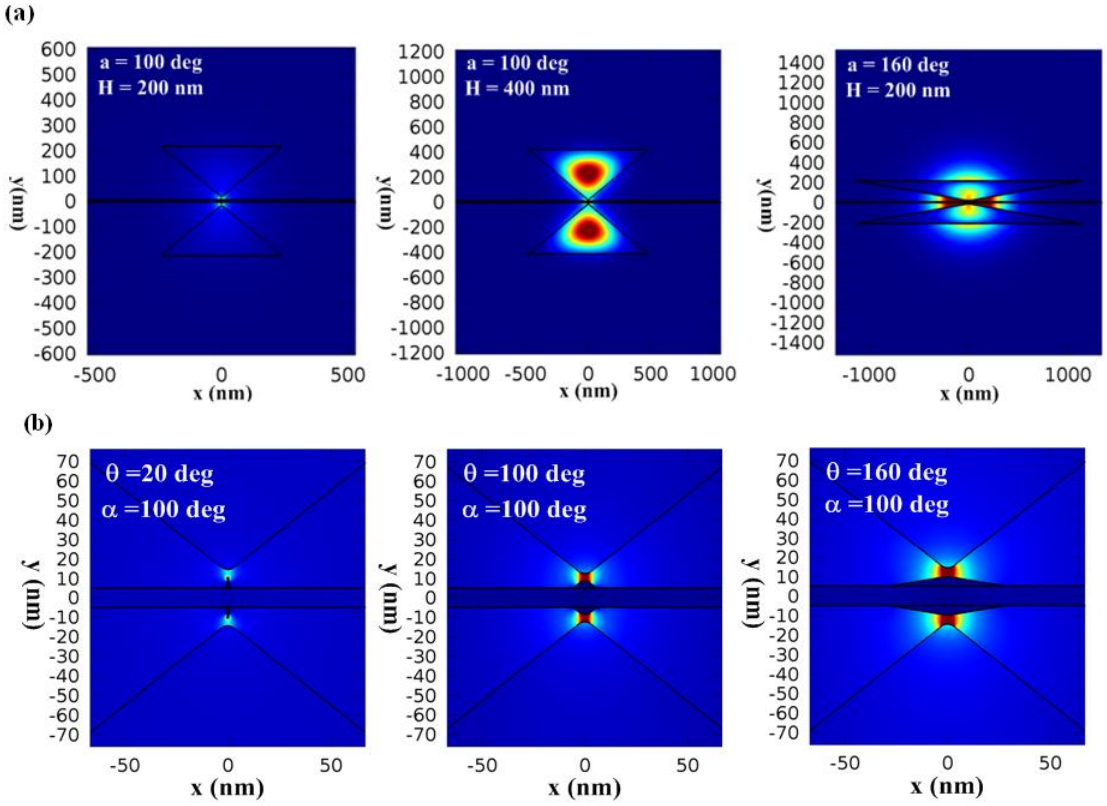

Fig. 5.14. (a) Normalized EM energy density distributions corresponding to different characteristic parameters. (b) Normalized EM energy density distributions for different θ.

Additional parameters which need to be considered for the waveguide are the thickness of the Ag film (d) and Ag nanowedge (h). Figs. 5.15 (a-b) show the dependence of the mode properties on d and h. In this simulation, the parameters are r = 10 nm, H = 200 nm, g = 5 nm, $\theta = 100°$ and $\alpha = 100°$. From Fig. 5.15 (a) it can be observed that the propagation length decreases as d increases, which is similar to that of the well-known LRSPPs mode [23]. In addition, as h increases, the size of the Ag nanowedge increases resulting in an increased power dissipation in the metal region, and hence a shorter propagation length [17]. From Fig.

5.15 (b) it can be seen that the normalized mode area slightly decreases as *d* increases, and the normalized mode area for *h* = 0 is distinctly larger than that for *h* = 5 nm and *h* = 10 nm, indicating that the waveguide with the Ag nanowedges offers a better mode confinement capability. In these calculations, the gap distance *g* is fixed, indicating that the longitudinal confinement (along the y direction) will only be slightly affected, and hence the improved mode confinement must originate from the strengthened lateral confinement (along the *x* direction).

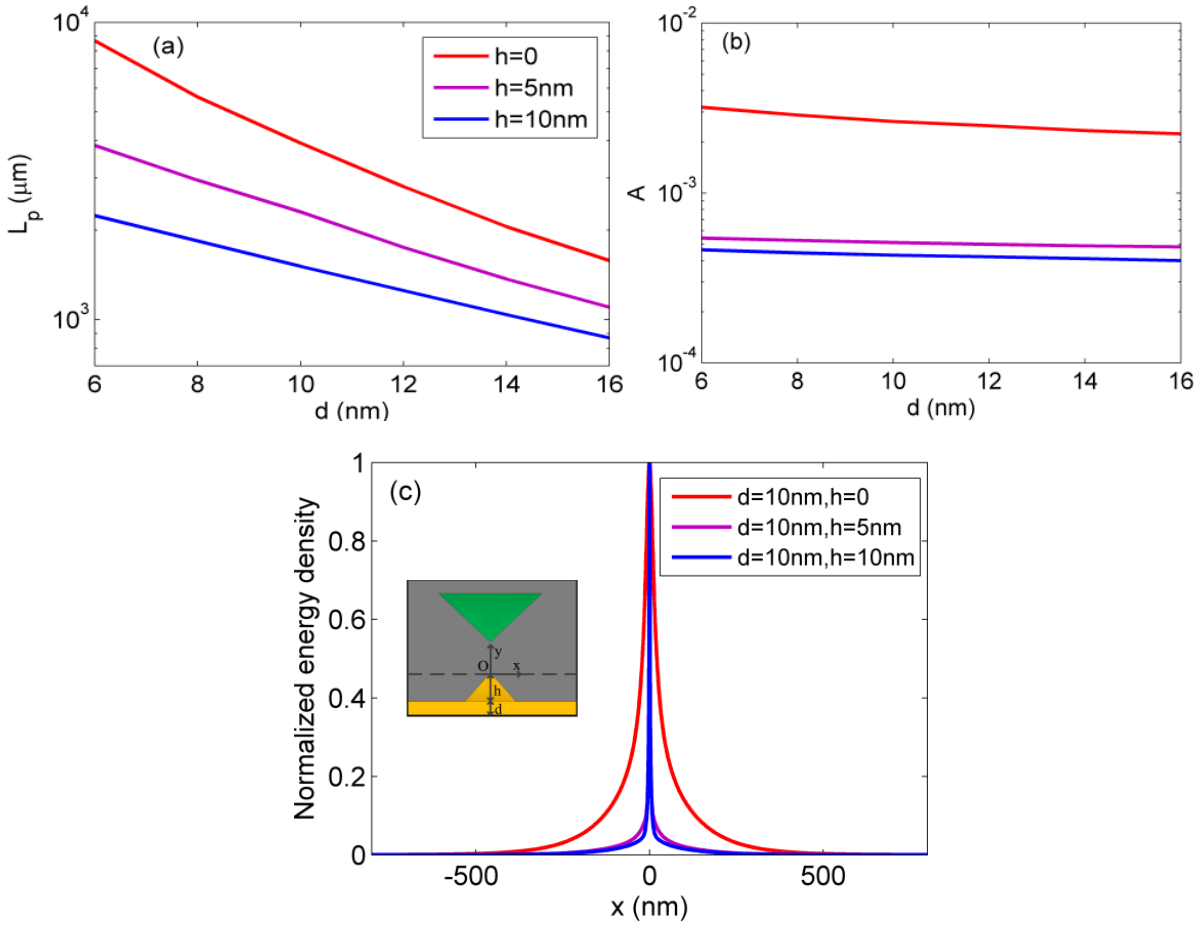

Fig. 5.15. (a) The propagation length L_p and (b) the normalized mode area *A* versus the Ag film thickness *d* with different Ag nanowedge height *h*. (c) Normalized electromagnetic energy density plots along the *x* direction with a fixed *d* and different *h*.

Fig. 5.15 (c) depicts the normalized EM energy density plots of LRWWHSPPs waveguide along the dashed line shown in the inset of Fig. 5.15 (c). Clearly the field is strongly confined

within an ultra-deep-subwavelength area when $h \neq 0$, and the mode profile difference for the Ag nanowedge with h = 5 nm and h = 10 nm is negligible. For example, the lateral mode width (W, which is defined as the full width where the energy density decays to 1/e of its peak value) of LRWWHSPPs waveguide for h = 5 nm is extremely as small as W = 3.35 nm, which is approximately 19 times smaller than that of W = 64 nm for h = 0.

The results discussed above reveal that the superior guiding capacity of the LRWWHSPPs waveguide could be realized by optimizing the structure parameters.

5.3.2 Performance comparison of the with LRWWHSPPs waveguide with a LRWHSPPs waveguide

In section 5.2 it was demonstrated that the LRWHSPPs waveguide outperforms several conventional HSPPs waveguide types in Refs. [2, 11, 15, 18]. Hence it is valid to draw a comparison between the LRWWHSPPs and LRWHSPPs waveguides to determine if the LRWWHSPPs waveguide is superior in performance. Fig. 5.16 shows the comparison of the LRWWHSPPs waveguide with the LRWHSPPs waveguide. The corresponding parameters used in the simulations are: $\theta = \alpha$ = 100°, d = 10 nm, h = 5 nm and H = 200 nm.

From Fig. 5.16 it is clear that the LRWWHSPPs waveguide has a better performance than the LRWHSPPs waveguide, or in other words, compared to LRWHSPPs waveguide, for the same propagation length, the LRWWHSPPs waveguide has better mode confinement; and for the same mode confinement, the LRWWHSPPs waveguide has longer propagation length. For example, for the same propagation length L_p = 1680 μm, the mode confinement for the LRWWHSPPs waveguide shows at least a nine fold improvement compared to that of the LRWHSPPs waveguide ($A_m = \lambda^2/10604$ for the LRWWHSPPs waveguide and $A_m = \lambda^2/1152$ for the LRWHSPPs waveguide). For the same mode confinement $A_m = \lambda^2/2353$, the

propagation length of the LRWWHSPPs waveguide (L_p = 2902μm) is 2.4 times longer than that of the LRWHSPPs waveguide (L_p = 1196 μm).

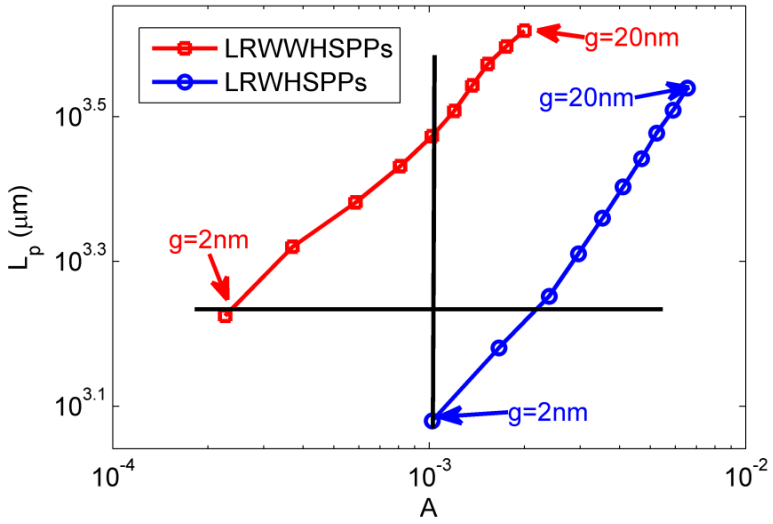

Fig. 5.16. Plot of the normalized mode area versus the propagation length for the LRWWHSPPs and LRWHSPPs waveguides.

From Fig. 5.16 it is clear that the LRWWHSPPs waveguide has a better performance than the LRWHSPPs waveguide, or in other words, compared to LRWHSPPs waveguide, for the same propagation length, the LRWWHSPPs waveguide has better mode confinement; and for the same mode confinement, the LRWWHSPPs waveguide has a longer propagation length. For example, for the same propagation length L_p = 1680 μm, the mode confinement for the LRWWHSPPs waveguide shows at least a nine fold improvement compared to that of the LRWHSPPs waveguide (A_m = λ^2/10604 for the LRWWHSPPs waveguide and A_m = λ^2/1152 for the LRWHSPPs waveguide). For the same mode confinement A_m = λ^2/2353, the propagation length of the LRWWHSPPs waveguide (L_p = 2902μm) is 2.4 times longer than that of the LRWHSPPs waveguide (L_p = 1196 μm).

Furthermore Fig. 5.17 shows the calculated coupling length L_c as a function of the center-to-center separation distance D for the LRWWHSPPs and LRWHSPPs waveguides. The coupling length is used to evaluate the crosstalk between the adjacent waveguides, which

is a critical parameter and ultimately limits the integration density of photonics devices. The crosstalk is dependent on the level of the field confinement, in other words, assuming the coupling condition is satisfied for two closely placed waveguides, strong field confinement (for an individual waveguide) will give rise to a long coupling length which is consistent with low crosstalk. In this simulation the comparison parameters are set as d = 10 nm, h = 5 nm, θ = α = 100° and H = 200 nm. As an example, the insets of Fig. 5.17 show the normalized energy density distributions for symmetric and antisymmetric modes with D = 600 nm and g = 5 nm for the LRWWHSPPs waveguide.

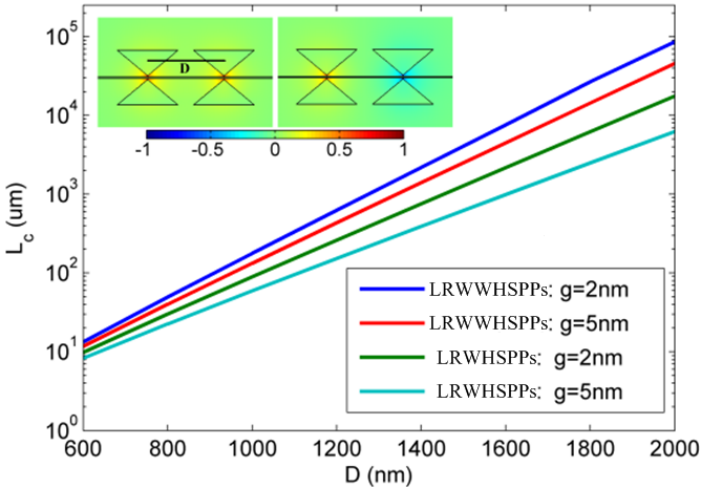

Fig. 5.17. The calculated coupling length versus the separation between the two plasmonic waveguides. Insets: the normalized electromagnetic density distributions for the symmetric mode and the antisymmetric mode for the LRWWHSPPs waveguide with D = 600 nm and g = 5 nm.

From Fig. 5.17 it is clear that the coupling length of the LRWWHSPPs waveguide is higher than that of the LRWHSPPs waveguide, this difference becomes more pronounced as D increases. For example, when D = 1000 nm and g = 5 nm, the coupling length of the LRWWHSPPs waveguide is 133 μm which is nearly two times that of the LRWHSPPs waveguide, which has an equivalent coupling length of 59.4 μm with the same values of D and g. For a larger value of D = 2000 nm and g = 5 nm, the coupling length of the LRWWHSPPs waveguide is 45588 μm which is nearly seven

times that of the LRWHSPPs waveguide with an equivalent coupling length of 6250 μm, for the same values of *D* and *g*. This result indicates that with the same coupling length, the LRWWHSPPs waveguide offers a significant reduction in crosstalk compared to the LRWHSPPs waveguide, which is a clear benefit for highly integrated photonics devices.

5.3.3 Discussion of the proposed fabrication steps and tolerances

As outlined in section 5.2.3, the fabrication process and error-tolerance of the LRWWHSPPs waveguides are discussed in this section.

5.3.3.1 Fabrication process

Fig. 5.18 schematically shows the suggested fabrication steps: (1) PMMA and Ag layers are successively deposited on a silica substrate; (2) a FIB technique can be used to form the Ag nanowedge [19]; (3) Silica and photoresist are coated on the wedge-patterned Ag surface, starting with the silica layer; (4-5) the V-groove is formed by FIB technique and then coated with silicon; (6) Lift-off (as a lift-off media, dimethyl sulfoxide is assumed to be used to strip photoresist) and FIB techniques are used to remove the upper spare silicon layer [24]; (7) A half-structure could be realized by coating silica and dissolving the PMMA in acetone [21]; (8) Finally, the structure can be fabricated through repeating steps (2-7) as required.

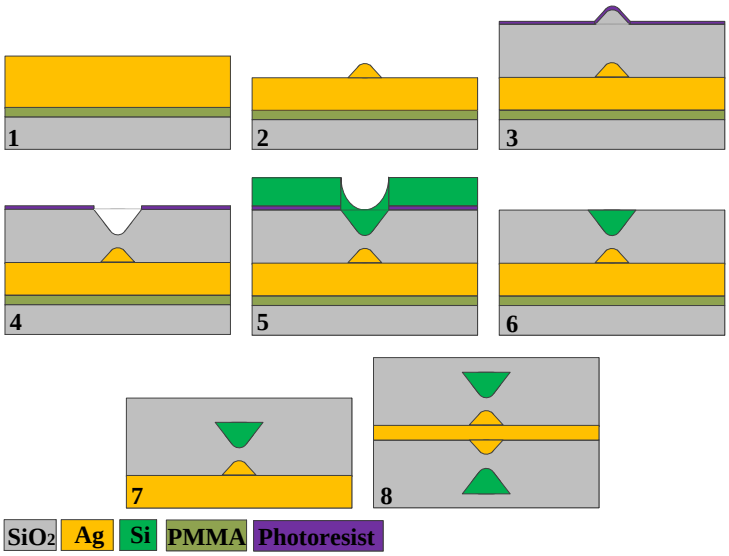

Fig. 5.18. Schematic diagram of the suggested fabrication steps for the LRWWHSPPs waveguide.

5.3.3.2 Fabrication error-tolerance

In practice, it is very difficult to realize an ideal fabrication process. It is important therefore to analyze the fabrication tolerances, including the misalignment between the Ag nanowedges (with the misalignment distance of *S*) and SiWGs as shown in Fig. 5.19 (a), and the uneven SiWG surface (the unevenness is described for the purpose of illustration by a sine function with the peak value of *G*) as depicted in Fig. 5.19 (b).

Two possible fabrication misalignments case labeled (1) and (2) with misalignment distances *S* are considered. The details are:

Case 1: both SiWGs tips are aligned to each other but deviate by a distance *S* relative to the tip of the Ag nanowedges.

Case 2: the SiWGs tips are not aligned to each other and are not aligned to the tips of the Ag nanowedges.

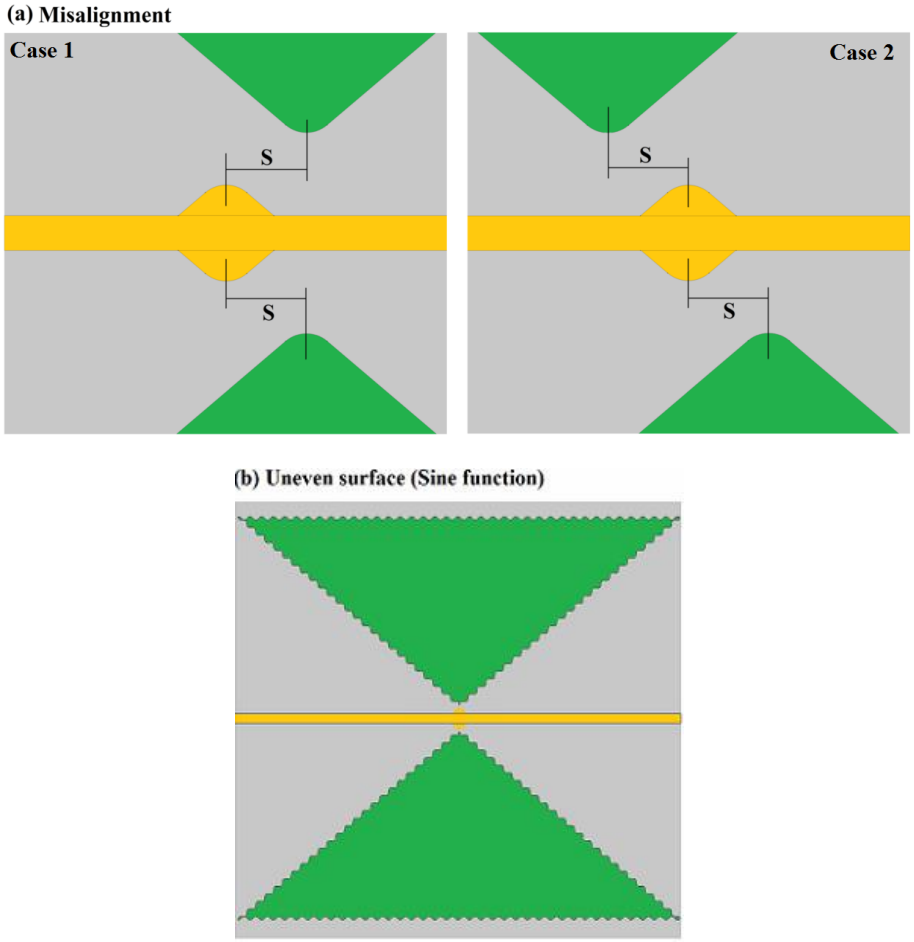

Fig. 5.19. Schematic views of (a) two types of misalignment and (b) uneven surface described by sine function.

Fig. 5. 20 (a) and (b) respectively depict the influence of the misalignment of SiWG and an uneven SiWG surface on the mode properties of the waveguide, where the insets are the corresponding normalized energy distributions. In both simulations, the waveguide parameters are given as follows: d = 10 nm, h = 5 nm, g = 5 nm, $\theta = \alpha$ = 100° and H = 200nm. As shown in Fig. 5. 20 (a), as S varies from 0 to 10 nm, the propagation length and normalized mode area experience variations of only 1% and 7% respectively. Fig. 5. 20 (b) shows that as the magnitude of the unevenness G increases to 5 nm, the propagation length and normalized mode area of the waveguide only experience variations of less than 0.1% and 0.6% respectively. The simulation results confirm that the proposed LRWWHSPPs

waveguide possess very good fabrication tolerance to both Ag nanowedge misalignment and unevenness on the SiWG surface.

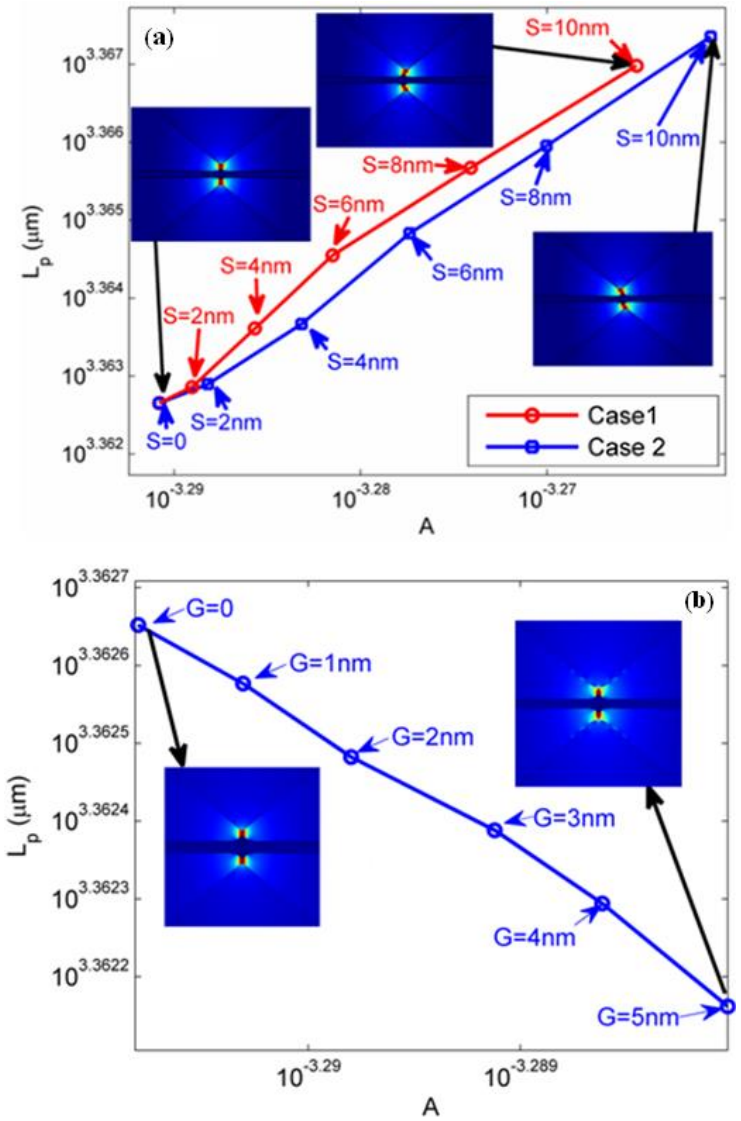

Fig. 5.20. The influence of (a) the alignment perturbation and (b) the uneven SWW surface on the mode properties. Insets: the normalized EM energy density distributions.

5.4 Summary

This chapter has addressed the challenge of achieving both a long propagation length and tight mode confinement for a plasmonic waveguide. In doing so two novel plasmonic waveguides based on hybrid SPPs (HSPPs) are proposed and analyzed: 1) One waveguide

consists of two dielectric nanowires placed on both sides of a nanowedge patterned metal film named LRWHSPPs waveguide; and 2) another waveguide consists of two dielectric wedge waveguides placed on each side of a nanowedge patterned metal film named LRWWHSPPs waveguide.

By optimizing the SPPs waveguide structure parameters, subwavelength confinement and relatively long propagation length could be simultaneously achieved. For example, the LRWHSPPs waveguide can confine light at a subwavelength scale (ranging from $\lambda^2/4000$ to $\lambda^2/400$) with a long propagation length (ranging from 1200 μm to 3500 μm), which is superior to other hybrid plasmonic waveguides previously reported in [2], [11], [15] and [18]. Moreover, further investigations have shown that the LRWWHSPPs waveguide outperforms the LRWHSPPs waveguide, indicating the LRWWHSPPs waveguide would achieve the best tradeoff compared to the recently published structures (to the best of my knowledge). For the LRWWHSPPs waveguide, the light can be confined to approximate three-thousandth of the diffraction spot size (ranging from $\lambda^2/10604$ to $\lambda^2/972$) without sacrificing the propagation length (ranging from 1680 μm to 4724 μm). The optimized results for the LRWWHSPPs waveguide demonstrate a 9-fold enhancement in mode confinement for the same propagation length or a 2.4-fold extended propagation length for the same mode confinement compared to the LRWHSPPs waveguide.

5.5 References

1. T. Holmgaard, and S. I. Bozhevolnyi, Theoretical analysis of dielectric-loaded surface plasmon-polariton waveguides, *Phys. Rev. B.*, 75, pp. 245405, (2007).
2. R. F. Oulton, V. J. Sorger, D. A. Genov, D. F. P. Pile, and X. Zhang, A hybrid plasmonic waveguide for subwavelength confinement and long-range propagation, *Nat.Photonics*, 2

(8), pp. 496-500, (2008).

3. R. F. Oulton, V. J. Sorger, T. Zentgraf, R. M. Ma, C. Gladden, L. Dai, G. Bartal, and X. Zhang, Plasmon lasers at deep subwavelength scale, *Nature*, 461, pp. 629-632, (2009).

4. T. P. H. Sidiropoulos, R. Roder, S. Geburt, O. Hess, S. A. Maier, C. Ronning and R. F. Oulton, Ultrafast plasmonic nanowire lasers near the surface plasmon frequency, *Nat. Physics*, 10, pp. 870-876, (2014).

5. X. Q. Wu, Y. Xiao, C. Meng, X. Zhang, S. L. Yu, Y. P. Wang, C. X. Yang, X. Guo, C. Z. Ning, and L. M. Tong, Hybrid photon-plasmon nanowire lasers, *Nano Lett.*, 13, pp. 5654-5659, (2013).

6. X. D. Yang, Y. M. Liu, R. F. Oulton, X. B. Yin, and X. Zhang, Optical forces in hybrid plasmonic waveguides, *Nano Lett.*, 11 (2), pp. 321-328, (2011).

7. L. Chen, T. Zhang, and X. Li, Enhanced optical forces by hybrid long-range plasmonic waveguides, *J. Lightwave Technol.*, 31, pp. 3432-3438, (2013).

8. S. Y. Zhu, G. Q. Lo, and D. L. Kwong, Theoretical investigation of ultracompact and athermal Si electro-optic modulator based on Cu-TiO_2-Si hybrid plasmonic donut resonator, *Opt. Express*, 21, pp. 12699-12712, (2013).

9. X. W. Gan, H. Wu, Y. C. Shi, L. Wosinski, and D. X. Dai, Ultracompact and broadband polarization beam splitter utilizing the evanescent coupling between a hybrid plasmonic waveguide and a silicon nanowire, *Opt. Lett.*, 38, pp. 3005-3008, (2013).

10. M. Z. Alam, J. N. Caspers, J. S. Aitchison, and M. Mojahedi, Compact low loss and broadband hybrid plasmonic directional coupler, *Opt. Express*, 21, pp. 16029-16034, (2013).

11. L. Chen, T. Zhang, X. Li, and W. P. Huang, Novel hybrid plasmonic waveguide consisting of two identical dielectric nanowires symmetrically placed on each side of a thin metal

film, *Opt. Express*, 20, pp. 20535-20544, (2012).

12. Y. S. Bian, X. Zhao, Y. L. Su, L. Liu, J. S. Liu, J. S. Zhu, and T. Zhou, Highly confined hybrid plasmonic modes guided by nanowire-embedded-metal grooves for low-loss propagation at 1550 nm, *IEEE J. Sel. Topics Quantum Electron.*, 19, pp. 4800106, (2013).
13. Y. S. Bian, Z. Zheng, X. Zhao, P. F. Yang, J. Xiao, G. J. Wang, L. Liu, J. S. Liu, J. S. Zhu, and T. Zhou, Silicon-Slot-Mediated guiding of plasmonic modes: the realization of subwavelength optical confinement with low propagation loss, *IEEE J. Sel. Topics Quantum Electron.*, 20, pp. 8100108, (2014).
14. J. W. Mu, L. Chen, X. Li, W. P. Huang, L. C. Kimerling, and J. Michel, Hybrid nano ridge plasmonic polaritons waveguides, *Appl. Phys. Lett.*, 103, pp. 131107, (2013).
15. Y. S. Bian, Z. Zheng, Y. Liu, J. S. Liu, J. S. Zhu, and T. Zhou, Hybrid wedge plasmon polariton waveguide with good fabrication-error-tolerance for ultra-deep-subwavelength mode confinement, *Opt. Express*, 19, pp. 22417-22422, (2011).
16. Z. H. Han, S. I. Bozhevolnyi, Radiation guiding with surface plasmon polaritons, *Reg. Prog. Phys.*, 76, pp. 016402, (2013).
17. E. Moreno, S. G. Rodrigo, S. I. Bozhevolnyi, L. M Moreno, and F. J. G-Vidal, Guding and focusing of electromagnetic fields with wedge plasmon polaritons, *Phys. Rev. Lett.*, 100, pp. 023901, (2008).
18. Y. S. Bian, and Q. H. Gong, Bow-tie hybrid plasmonic waveguides, *J. Lightw. Technol.*, 32, pp. 3902-3907, (2014).
19. T. Ogawa, D. F. P. Pile, T. Okamoto, M. Haraguchi, M. Kukui, and D. K. Gramotnev, Numerical and experimental investigation of wedge tip radius effect on wedge plasmons, *J. Appl. Phys*., 104, pp. 033102, (2008)

20. T. Kuykendall, P. J. Pauzauskie, Y. Zhang, J. Goldberger, D. Sirbuly, J. Denlinger, and P. Yang, Crystallographic alignment of high-density gallium nitride nanowire arrays, *Nat. Mater*, 3, pp. 524-528, (2004).

21. Z. Yan, G. X. Liu, J. M. Khan, A. A. Balandin, Graphene quilts for thermal management of high-power GaN transistors, *Nat. Commun*., 3, pp. 827, (2012).

22. J. B. Andersen, and V. V. Solodukhov, Field behavior near a dielectric wedge, *J. Lightw. Technol.*, 26, pp. 598-602, (1978).

23. Berini, Long-rang surface plasmon polaritons, *Adv. Opt. Photonics*, 1, pp. 484-588, (2009).

24. W. S. Yue, Z. H. Wang, Y. Yang, L. Q. Chen, A. Syed, K. C. Wong, and X. B. Wang, Electron-beam lithography of gold nanostructures for surface-enhanced Raman scattering, *J. Micromech. Microeng.*, 22, pp. 125007, (2012).

Chapter 6: Plasmonic sensor

6.1 Introduction

In Chapters from three to five, the SPPs waveguiding mechanism has been investigated and its potential applications in highly integrated photonic circuits were described. Another unique feature of SPPs is that their ultra-tight mode confinement makes them highly sensitive to minor changes in the surrounding local area, thus offering a substantial potential for effective biosensing.

It is well known that the characteristics of SPPs are highly dependent on the dielectric environment in the vicinity of the contact with the metal, which enables the extensive use of SPPs for real time detection of the presence of biochemical analytes [1-2]. Furthermore, the strong confinement of SPPs offers the potential to construct high-density micrometer-sized arrays of independent sensing elements [3].

In this chapter the principle of SPPs based biosensors is investigated and two novel SPPs based biosensors are designed and analyzed: 1) a metal grating structure embedded in a multimode fiber, which offers high sensitivity compared to a conventional multimode fiber sensor coated with uniform metal layer, and 2) a reflection metal grating used for simultaneous detection of refractive index and thickness of the analyte layer.

6.2 A multimode fiber biosensor coated with a subwavelength metal grating layer

Traditional SPPs biosensors are based on the so-called Kretschmann configuration, where a thin metal film is deposited on the surface of a coupling prism [4]. For such prism-based

SPPs sensors, Homola [5] provides a comprehensive overview of developments in the past 20 years and numerous designs for novel SPPs biosensors. For example, various structures based on the Kretschmann configuration have been proposed and explored to sharpen the SPPs dip curve and enhance the sensing resolution, mainly via designing a multilayer stack on the hypotenuse face of the prism, including an Au-Ag bimetallic film [6], insulator-metal-insulator layers [7], and waveguide coupled SPPs (WCSPPs) [8]. Unfortunately a prism-based SPPs configuration suffers from a number of disadvantages, such as bulky size, complex operation and a lack of potential for remote sensing.

An alternative fiber based sensing configuration allows for a compact sensing element and sample volume, the capacity for remote sensing and the potential for disposable miniaturized sensing devices, which has attracted significant research interest worldwide [9-12]. In the past decade, various fiber based SPPs biosensors have been proposed and demonstrated, including the use of either single mode fibers [13] or multimode fibers [14].

Recently, several fiber based SPPs biosensors have been presented such as a multimode fiber coated with bimetallic layers (silver and gold, with gold as the outer layer), and a hetero-core fiber with Au/Ta_2O_5/Pd multi-layers, which were both studied theoretically based on the attenuated total reflection (ATR) method and multi-layer model [15-17]. Among these studies, the effects of the parameters and characteristics of the optical fiber and metal layer on the sensor sensitivity have been investigated in detail. For example, recently the relationships between the resonance wavelength and the thickness of the metal layer and sensing layer were investigated in [18].

To further enhance the sensitivity, here a novel multimode fiber based biosensor embedded with a subwavelength metal grating layer is proposed and investigated. As shown in Fig. 6.1 (a), the structure is assumed to be surrounded by the sensing sample with a refractive index

(RI) of n_s, and where the diameter of the multimode core is denoted as D. Fig. 6.1 (b) depicts the subwavelength metal grating layer, with a grating period P, a thickness h, a width of metal d, and a total length L. All the structural parameters are shown in Fig. 6.1.

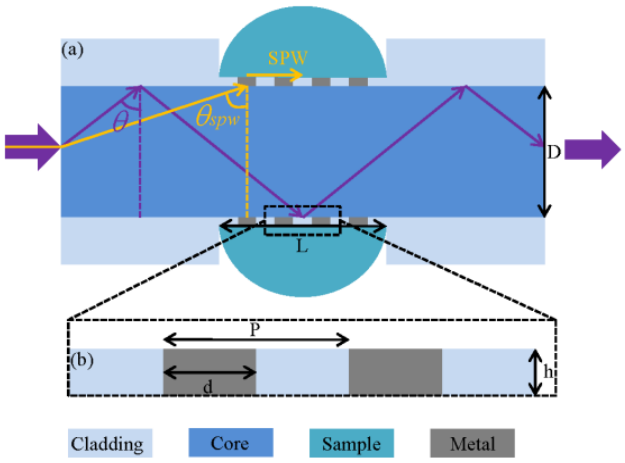

Fig. 6.1. Schematic diagram for (a) Fiber-based SPR biosensor with a sub-wavelength metal grating layer. (b) Illustration of the subwavelength metal grating layer.

6.2.1 Theoretical underpinning

Before studying the proposed structure, it is useful to initially consider the ATR method with a Kretschmann configuration (as shown in Fig. 6.2), as this forms the basis of the theoretical model for the fiber SPPs based sensor. For the Kretschmann configuration, if the resonance condition is satisfied, that is the wave-vector of the incident light matches that of the SPPs, then the output spectrum demonstrates a reflection dip located at the resonance wavelength. As illustrated in ref. [5], the resonance wavelength is highly sensitive to the RI variations in the sensing sample, i.e. the resonance wavelength (λ_R) shifts by $\delta\lambda_R$ when the RI of the sensing sample alters by δn. The change δn may be caused by the deposition or binding of certain molecules on the metal surface.

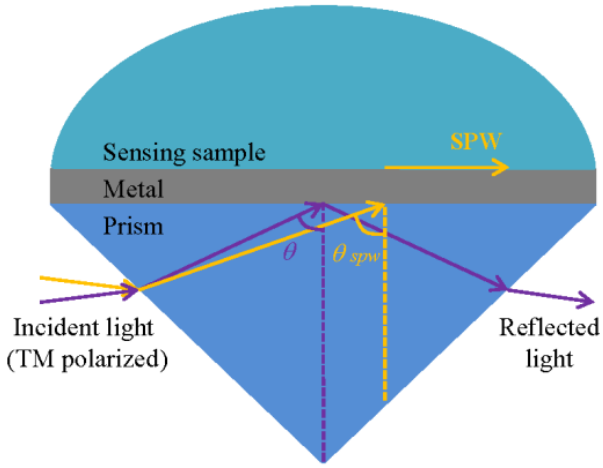

Fig. 6.2. Schematic view of a prism-based SPPs sensor utilizing the Kretschmann configuration.

As shown in Fig. 6.2, the structure typically comprises a three-layer configuration: a coupling prism with a high RI, a thin metal layer and a sensing sample layer. To calculate the reflectivity of the TM-polarized incident light through the Kretschmann configuration, a multilayer (*N*-layer) model (also called as transfer-matrix method) is used [19], as shown in Fig. 6.3. The layers are assumed to be stacked along the z-axis. Each layer is defined by a thickness h_m, permeability μ_m, dielectric constant ε_m and RI n_m, where $m=2, 3, \ldots, N-1$. All the layers are assumed to be uniform, isotropic, and non-magnetic.

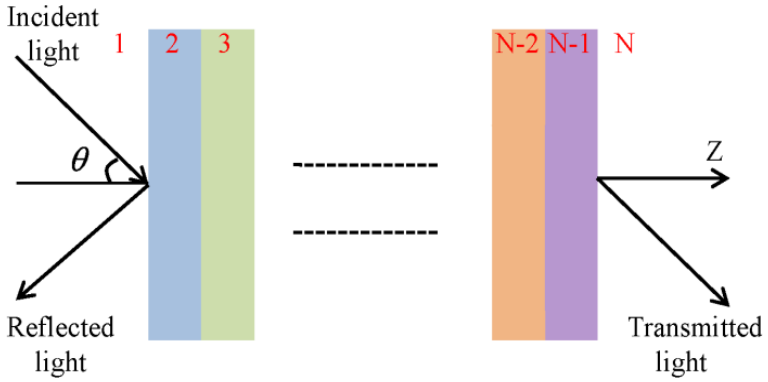

Fig. 6.3. Representation of a multilayer (*N*-layer) model.

The relationship of the tangential components of the electric field $E^{//}$ between the first boundary Z_1 and the final boundary Z_{N-1} is expressed as:

$$\left[E_1^{//}\right] = M\left[E_{N-1}^{//}\right] \qquad (6.1)$$

where *M* is the characteristic matrix and is given by:

$$M = \prod_{m=2}^{N-1} M_m = \begin{bmatrix} M_{11} & M_{12} \\ M_{21} & M_{22} \end{bmatrix} \qquad (6.2)$$

$$M_m = \begin{bmatrix} \cos\beta_m & \frac{-i\sin\beta_m}{q_m} \\ -iq_m\sin\beta_m & \cos\beta_m \end{bmatrix} \qquad (6.3)$$

where

$$\beta_m = \frac{2\pi h_m}{\lambda}\sqrt{\varepsilon_m - (n_1 \sin\theta)^2}, q_m = \frac{\sqrt{\varepsilon_m - (n_1 \sin\theta)^2}}{\varepsilon_m} \qquad (6.4)$$

Then the reflectivity for the *N*-layer stacked structure illuminated by a TM-polarized light is given as [19]:

$$R_{TM} = \left|\frac{(M_{11}+M_{12}q_N)q_1 - (M_{21}+M_{22}q_N)}{(M_{11}+M_{12}q_N)q_1 + (M_{21}+M_{22}q_N)}\right|^2 \qquad (6.5)$$

Consider the fiber based SPPs sensor as shown previously in Fig. 6.1. For this structure, the prism is replaced by the fiber core. Similarly a three-layer configuration (fiber core/subwavelength metal grating layer/sensing sample layer) are considered in this analysis. Particularly for the subwavelength metal grating layer, based on the quasi-static limits (i.e. the grating-period-to-wavelength ratio $P/\lambda \rightarrow 0$), its optical properties are equivalent to a uniaxial homogeneous layer whose effective permittivity can be calculated by the effective medium theory (EMT) [20]. The effective permittivity ε_{eff} can be written as $\varepsilon_{eff} = \varepsilon_D + (\varepsilon_M - \varepsilon_D)d/P$, where ε_D and ε_M are the permittivities of the dielectric and metal, respectively. The frequency-dependent complex relative permittivity of the metal (gold in this case) is characterized by the Drude model.

When the light is launched into one end of the multimode fiber, the proportion of the beam crossing within the numerical aperture of the fiber is guided due to total internal reflection (TIR). Assuming the wavevector matching condition is satisfied, SPPs propagating along the metal-sample interface (named surface plasmon wave (SPW)) will be excited by the evanescent wave due to TIR, thus resulting in a SPPs dip in the corresponding transmission spectrum. The resonance condition can be expressed by the following equation [20]:

$$k_{SPPs} = k_{in} sin\theta \pm \frac{2m\pi}{P} = k_{in}\sqrt{\frac{\varepsilon_{co}\varepsilon_{eff}}{\varepsilon_{co}+\varepsilon_{eff}}} + 2k_{in}\frac{\varepsilon_{eff}\varepsilon_{s}}{\varepsilon_{eff}^{2}-\varepsilon_{s}^{2}}\frac{\varepsilon_{co}-\sqrt{\varepsilon_{co}\varepsilon_{eff}+\varepsilon_{s}(\varepsilon_{co}-\varepsilon_{eff})}}{\varepsilon_{co}+\sqrt{\varepsilon_{co}\varepsilon_{eff}+\varepsilon_{s}(\varepsilon_{co}-\varepsilon_{eff})}}\exp(2ik_{in}h\frac{\varepsilon_{eff}}{\sqrt{\varepsilon_{eff}+\varepsilon_{s}}}) \quad (6.6)$$

where m is an integer indicating the order of diffraction, ε_{co} is the permittivity of the fiber core, and ε_{s} is the permittivity of the sensing sample. The normalized transmitted power detected at the other end of the multimode fiber can then be written as [21]:

$$P_T = \frac{\int_{\theta_{cr}}^{\pi/2} R_{TM}^{K}(n_{co}^2 \sin\theta\cos\theta)/(1-n_{co}^2\cos^2\theta)^2 d\theta}{\int_{\theta_{cr}}^{\pi/2}(n_{co}^2 \sin\theta\cos\theta)/(1-n_{co}^2\cos^2\theta)^2 d\theta} \quad (6.7)$$

where θ is the incident angle of the ray normal to the core-metal interface, n_{co} (n_{co}= 1.457) and n_{cl} (n_{cl}= 1.4395) are the RIs of the fiber core and cladding, respectively. K and θ_{cr} are the number of light reflections in the sensing region and the critical angle of reflection, which can be calculated using the following equations [21]:

$$K = \frac{L}{D\tan\theta}, \ \theta_{cr} = \sin^{-1}(n_{cl}/n_{co}) \quad (6.8)$$

where L and D are the length of the grating length and the fiber core diameter, respectively.

6.2.2 Sensing performance evaluation

Sensitivity is a critical parameter to evaluate the performance of a sensor. Therefore the sensitivity of the proposed sensor is firstly investigated based on the analytical model shown above. Fig. 6.4 (a) firstly depicts the normalized transmission spectra for different values of the refractive index of n_s. In the simulation, the structural parameters are set to be L = 20 *mm*, D = 400 *um*, d = 10 *nm*, P = 20 *nm*, h = 30 *nm* and $\varepsilon_D = n_{cl}^2$. These parameters are chosen based on the optimization procedures discussed in the sub-section which follows this one. From Fig. 6.4 (a) one can see that as n_s increases, the SPPs dip shifts toward a longer wavelength, which shows that RI changes for the sample surrounding the metal grating film can be monitored by measuring the shift of the resonance wavelength. It can be estimated from Fig. 6.4 (a) that the proposed fiber based SPPs sensor has an estimated sensitivity of 13000 nm/RIU in the RI range from 1.395 to 1.40 and 3892 nm/RIU in the RI range from 1.333 to 1.353. For RI range of 1.395-1.40, the sensitivity is far higher than that of previously reported fiber based SPPs sensor of 7500 nm/RIU achieved in [14], and the sensitivity in RI range of 1.333-1.353 is comparable with that of 4262 nm/RIU achieved in [19].

Further investigations were carried out comparing the effect of a metal grating layer (i.e. d = 10 *nm*) with respect to a uniform metal layer (i.e. d =P = 20 *nm*) and the result is shown in Fig. 6.4 (b). This figure shows that as the RI of the sample increases the central resonance wavelengths for both sensors increase monotonically. However it is easy to see that the fiber based SPPs sensor with a subwavelength metal grating layer shows a higher sensitivity (as indicated by the higher slope) compared to that with a uniform metal layer. The sensitivities are calculated for both sensors at three different points across the refractive index range and are shown in a histogram in the inset to Fig. 6.4 (b).

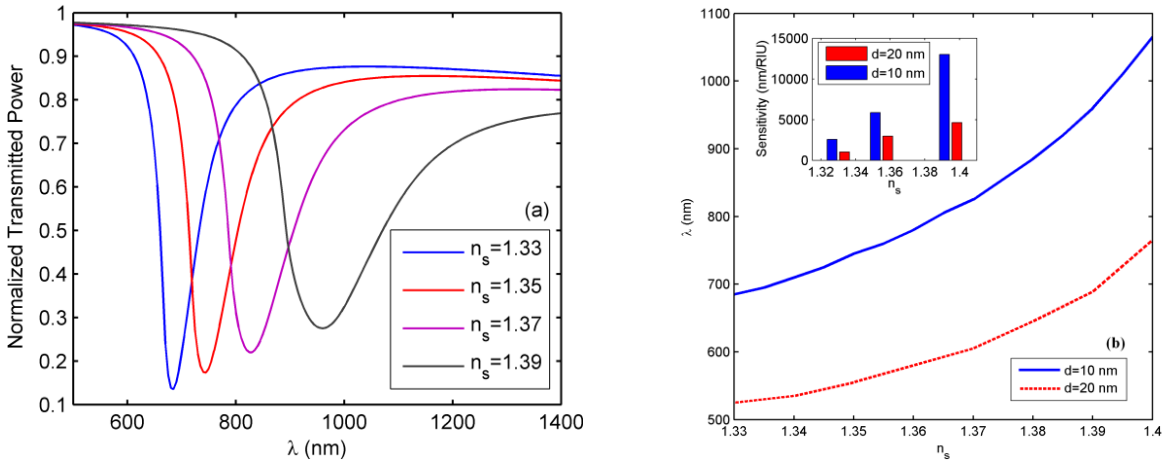

Fig. 6.4. (a) Numerical simulation of the normalized transmission versus wavelength for different refractive indices of the sensing sample. (b) Calculated central wavelength vs. the sensing sample refractive index and the sensitivity (inset).

6.2.3 Influence of geometric parameters on sensing performance

In order to better understand the transmission properties of the proposed fiber based SPPs sensor, the spectral response of the structure with various geometric parameters is studied.

According to the resonance condition in Eq. (6.6), it can be shown that the resonance wavelength of the sensor is related to the grating period of P and the grating thickness of h. Fig. 6.5 (a) depicts the normalized transmission spectra of the structure at different values of P. In this simulation, the structural parameters are L = 20 mm, D = 400 um, h = 30 nm, n_s = 1.36, d = 10 nm and $\varepsilon_D = n_{cl}^2$. From Fig. 6.5 (a) one can see that the spectral response is dependent on the metal grating period. The central resonance wavelength increases as P increases. This is reasonable based on Eq. (6.6). Fig. 6.5 (b) shows the corresponding variations in the sensitivity S as well as the Q value vs. P. It can be seen that as the value of P increases, S increases while Q decreases. A physical insight into this is that as P increases, with a fixed width d for the metal in the grating, then the fiber cladding material begins to dominate the effective permittivity ε_{eff} and thus the real part of ε_{eff} decreases, resulting in an

enhanced evanescent field outside of the fiber core. This is turn strengthens the coupling of evanescent field with SPPs and thus an increased sensitivity.

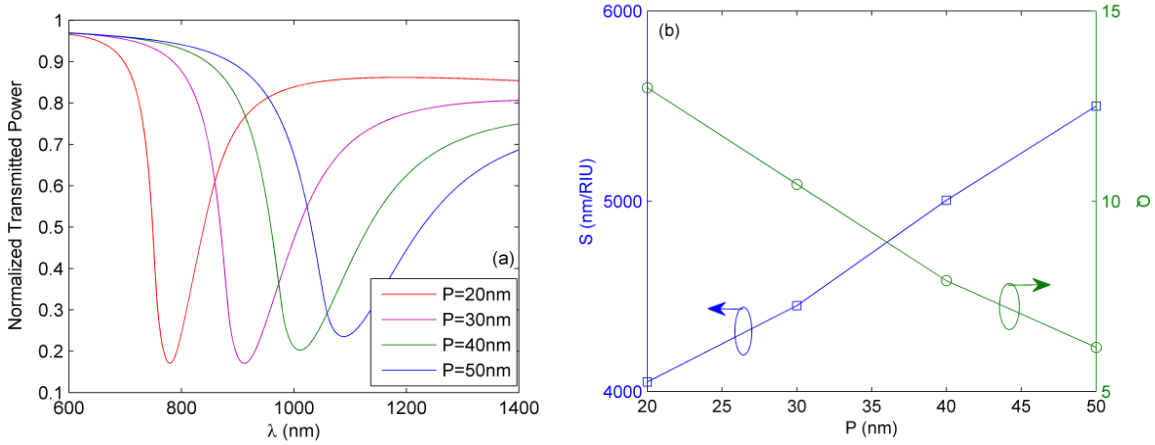

Fig. 6.5. (a) Variation of the normalized transmission with wavelength for the different metal grating period *P* values. (b) Variation of the sensitivity *S* and *Q* at n_s=1.36 vs. the metal grating period *P*.

Fig. 6.6 (a) shows the normalized transmission spectra at different values of the metal grating thickness *h*. In this simulation the structural parameters are $L = 20\ mm$, $D = 400\ \mu m$, $d = 10\ nm$, $P = 20\ nm$, $\varepsilon_D = n_{cl}^2$ and $n_s = 1.36$. The effect of the metal grating thickness on the spectral response can be clearly seen. The central resonance wavelength as well as the transmission value of the dip increases as *h* increases. This is reasonable due to the fact that thicker metal grating layer, smaller the interaction between the SPPs mode and fiber mode. Smaller interaction causes less absorption of light around the resonance wavelength, and hence the SPPs curve narrows and shifts upwards. The narrowing of the SPPs curve results in an increased *Q* value, as shown in Fig. 6.6 (b). Since this up-shift does not change the resonance wavelength appreciably, the sensitivity *S* does not change by a significant amount (Fig. 6.6 (b)).

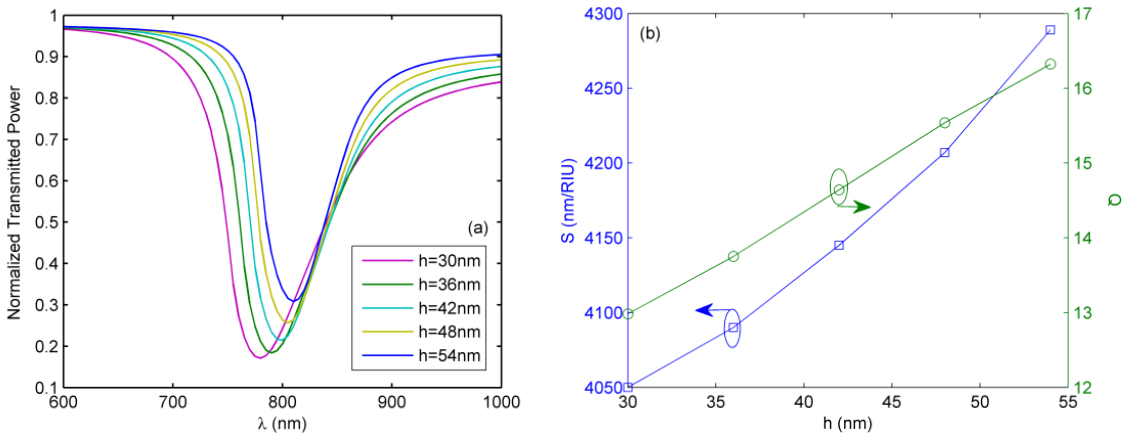

Fig. 6.6. (a) Variation of the normalized transmission with wavelength for the different metal grating layer thickness *h*. (b) Variation of the sensitivity *S* and *Q* at n_s = 1.36 vs. the metal grating layer thickness *h*.

Fig. 6.7 depicts the corresponding variations in the sensitivity *S* as well as *Q* for different values of the grating length *L* and the fiber core diameter *D*. For the results shown in Fig. 6.7 (a), the structural parameters are h = 30 *nm*, D = 400 μm, d = 10 *nm*, P = 20 *nm*, $\varepsilon_D = n_{cl}^2$ and n_s = 1.36, while the structural parameters for the simulation in Fig. 6.7 (b) are h = 30 *nm*, L = *20 mm*, d = 10 *nm*, P = 20 *nm*, $\varepsilon_D = n_{cl}^2$ and n_s = 1.36. From Fig. 7, it can be seen that the values of both *S* and *Q* decrease as *L* increases, while *S* and *Q* values increase as *D* increases. These results could be understood as follows: as *L* increases, the number of reflections in the sensing region increases resulting in higher metal dissipation loss, and hence broadening of the SPPs spectral dip, in turn decreasing the *Q* value. As *D* increases, the number of reflections decreases (i.e. there is less metal dissipation loss) and hence sharpening of the SPPs spectral dip thereby increasing the *Q* value. However this broadening-sharpening effect has a moderate influence on the resonance wavelength, therefore the change of the sensitivity *S* is not that significant.

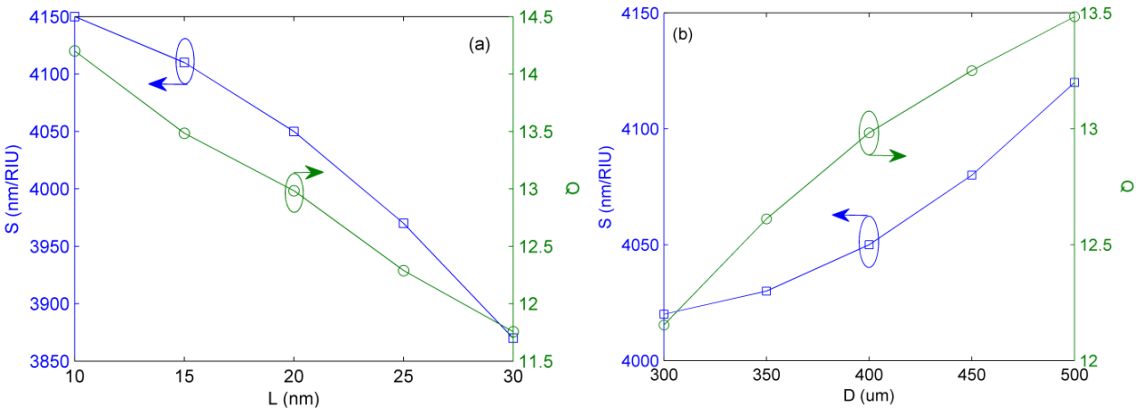

Fig. 6.7. Variations of the sensitivity S and Q at n_s = 1.36 vs. the grating length L (a) and the fiber core diameter D (b).

Based on the results shown above, we find that the quality factor Q of the SPPs dip is affected by the characteristic structural parameters, i.e. the fiber core diameter D, the grating length L, the metal grating period P and the metal grating layer thickness h. However, it can be observed that the influence of the structural parameters of h, D and L on the sensitivity S is moderate. For example, for a change in h from 30 nm to 54 nm the sensitivity S changes by circa 6%, whereas the metal grating period P has a relatively larger effect with a 35.8% variation in the sensitivity S as P varies from 20 nm to 50 nm, as evident in Fig. 6.5 (b).

6.3 Subwavelength plasmonic grating based sensor for simultaneous measurement of both thickness and refractive index

It is known that a prism based SPPs sensor needs precise incident beam angle control and is too bulky for integration. As an alternative, a SPPs sensor based on a subwavelength metal grating (MG) has sparked a lot of research interest [22-23] due to its unique characteristics: (I) a compact volume which makes it suitable for integration into microfluidic components [3], and (II) SPPs can be excited by an illumination at normal incidence, thereby removing any stringent light coupling requirements. Because of these specific advantages, recently various

SPPs based RI sensors utilizing the subwavelength MGs have been proposed and investigated, including a transmission MG (TMG) [24-26] and a reflection MG (RMG) [27-29]. Development of these structures has led to an increase in the RI detecting sensitivity, but for the case of thin layers of analytes the performance of such structures is rather limited [29]. For example, when assembling deoxyribonucleic acid (DNA) layer-by-layer on the surface of a subwavelength MG, the variations of physicochemical property of the layers i.e. the thickness (which is assumed to be smaller than the decay length of SPPs) and the RI (caused due to the bio-reaction) are simultaneously taking place [30]. Both variations will perturb the properties of SPPs. Put another way, it is difficult to distinguish between the variations induced by the changes in the layer thickness from those induced by the RI variations.

To address this challenge, a novel RMG based sensor, which is capable of simultaneously measuring RI and the thickness of the analyte layer, is proposed and analyzed here. The schematic diagram of the investigated structure is shown in Fig. 6.8.

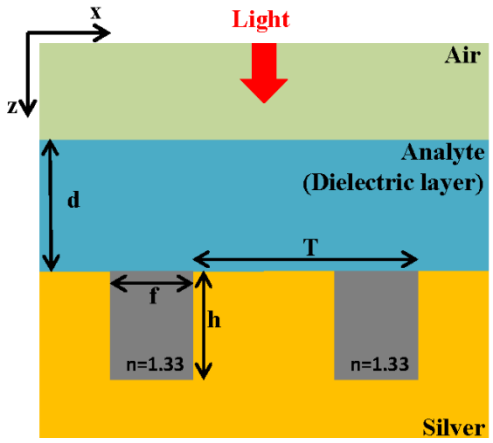

Fig. 6.8. Schematic diagram of the plasmonic grating used as a biosensor illustrating the structural parameters and coordinates. The analyte layer is denoted as the dielectric layer with a thickness of d and RI of n_d.

Fig. 6.8 shows a one-dimensional subwavelength RMG (with the grating period T, the slit width f and height h) coated with a dielectric layer (i.e. analyte, with a thickness d and

refractive index n_d) surrounded by air. For this structure, it is assumed that a TM-polarized source with illuminates the grating with a normal incidence. For the purpose of the simulation, we assume the slit is filled with a dielectric material with a RI (n = 1.33) close to that of the sensing analyte.

6.3.1 Reflection of by the RMG

Before studying the sensing performance of the RMG, it is worthwhile to consider its reflection characteristics. Fig. 6.9 (a) shows the simulated reflection spectra for the structure depicted in Fig. 6.8. The structural parameters in the simulation are as follows: n_d = 1.33, T = 600 *nm*, f = 50 *nm*, h = *300 nm* and d = *600 nm*. As shown in Fig. 6.9 (a) there are basically two reflection dips in the wavelength range from 700 *nm* to 1000 *nm*, positioned at 773.2 *nm* and 930 *nm*, respectively. The width of the reflection dip at 930 *nm* is much larger than that at 773.2 *nm*. The Q value for the dip at 930 *nm* is 33.1, which is less than half of the Q value of 72.8 for the dip at 773.2 *nm*.

It is useful to visualize the field distributions within the structure for different wavelengths and resonance types. Figs. 6.9 (b-c) show the corresponding normalized electromagnetic 2D-field patterns. Fig. 6.9 (b) indicates that the reflection dip at 930 *nm* is excited by the cavity resonance mode (CRM) since the fields are strongly concentrated in the slits with standing wave patterns, and only a small portion of the field leaks outside. However Fig. 6.9 (c) shows that the reflection dip at 773.2 *nm* is excited by the hybrid plasmonic-cavity mode (HPCM) i.e. the mode is of hybrid nature with contribution from both SPPs and CRM.

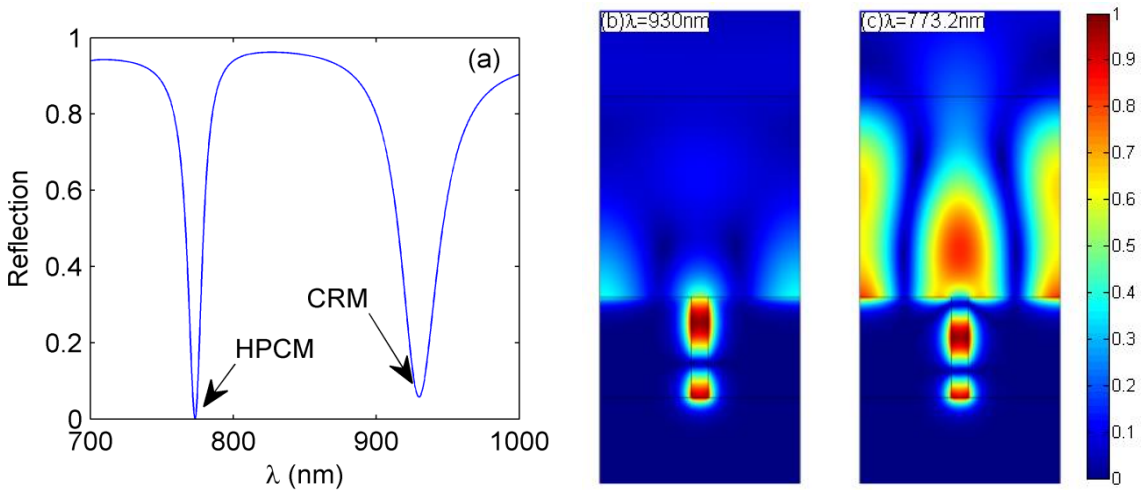

Fig. 6.9. (a) Reflection spectrum of the investigated structure at normal incidence. Two reflection dips occur at 930 *nm* and 773.2 *nm* in the investigated wavelength range. The normalized electromagnetic field distributions of radiation at a wavelength of (b) 930 *nm* and (c) 773.2 *nm* at normal incidence.

6.3.2 Individual measurements of RI and thickness

As shown in Figs. 6.9 (b-c), compared to the CRM, the field distribution of the HPCM offers a larger overlap with the analyte, indicating the HPCM is more likely to be affected by the RI and thickness variations of the analyte. For example, Fig. 6.10 (a) shows a contour plot of the normalized reflected intensity as a function of both wavelength and the value of n_d as n_d varies from 1.33 to 1.38. The red-coloured region indicates a total reflection and the dark blue regions represent reflection dips arising from the excitation of HPCM or CRM. The geometric parameters are T = 600 *nm*, f = 50 *nm*, h = 300 *nm* and d = 600 *nm*. It is clear that the shift in the reflection dip related to HPCM is more sensitive to n_d than that of another dip produced by the CRM, given the differences in slope evident in the contour plots. The reflection dip related to the CRM experiences a linear red shift with a sensitivity ($\triangle\lambda/\triangle n$) of 240 *nm*/RIU (refractive index unit). However the dip associated with the HPCM experiences a red shift with a significantly higher sensitivity of 448 *nm*/RIU. This is due to the fact that the field of CRM is more strongly concentrated within the cavity which is relatively far from

the analyte layer compared to that of HPCM and hence the influence of the analyte layer on HPCM is more significant than that on CRM.

In addition, the influence of the thickness of the analyte layer on the spectral response was also investigated and shown in Fig. 6. 10 (b). The parameters used in the simulation are T = 600 *nm*, f = 50 *nm*, h = 300 *nm* and n_d = 1.35. As expected, as the thickness d varies, the reflection dip related to the CRM remains substantially unchanged, while the dip related to the HPCM experiences a significant linear red-shift with a sensitivity ($\triangle\lambda/\triangle d$) of 75 *nm/um*.

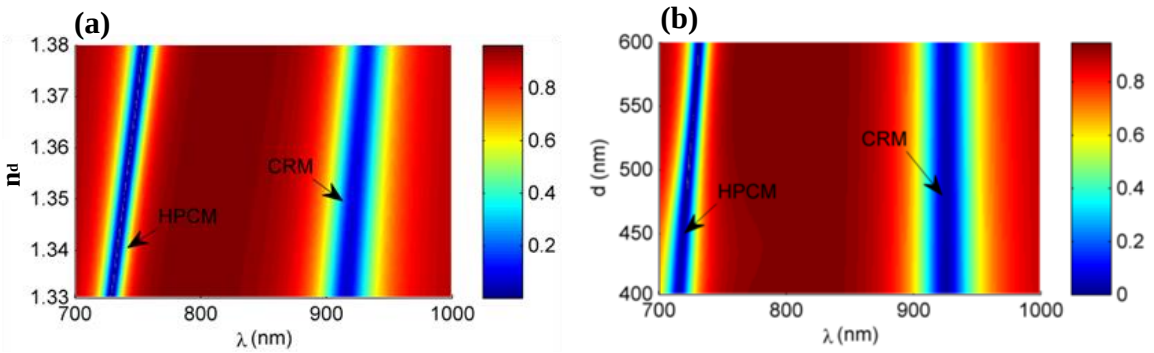

Fig. 6.10. (a) Contour plot of the normalized reflection versus both the wavelength and the refractive index of n_d for the investigated structure. (b) Contour plot of the normalized reflection versus both the wavelength and the thickness of the analyte layer d for the investigated structure.

6.3.3 Simultaneous measurement of RI and thickness

From the above discussions, it is known that the central wavelength of the dip related to HPCM depends on both the thickness and refractive index, but the wavelength shift related to CRM is thickness independent but sensitive to the refractive index change. This opens up a useful possibility that of being able to distinguish and measure both the thickness and RI simultaneously. As an example, in our simulation, the relationship between HPCM-induced

wavelength shift ($\Delta\lambda_{HPCM}$) and CRM-induced spectral response variation ($\Delta\lambda_{CRM}$) can be expressed as:

$$\begin{cases} \Delta\lambda_{\mathrm{HPCM}} = 448\,\frac{\mathrm{nm}}{\mathrm{RIU}} * \Delta \mathrm{n_d} + 75\,\frac{\mathrm{nm}}{\mathrm{um}} * \Delta \mathrm{d} \\ \Delta\lambda_{\mathrm{CRM}} = 240\,\frac{\mathrm{nm}}{\mathrm{RIU}} * \Delta \mathrm{n_d} \end{cases} \quad (6.9)$$

where Δd and $\Delta \mathrm{n_d}$ are the thickness and RI variations of the analyte layer, respectively. Since the wavelength variations of the two spectral dips can be measured independently, by solving Eq. (6.9) using measured values, both the thickness and RI can be determined independently.

6.4 Summary

In this chapter a novel multimode fiber based SPPs biosensor with a subwavelength metal grating layer based on a multilayer model has been proposed and investigated. The proposed biosensor has an estimated sensitivity of 3892 nm/RIU in the RI range from 1.333-1.353, which is comparable with that previously achieved (4262 nm/RIU (RI: 1.355-1.365) in [19]) and an estimated sensitivity of 13000 nm/RIU in the RI range from 1.395 to 1.40, which is significantly higher than that previously achieved (7500 nm/RIU (RI: 1.395-1.40) in [14]). The effects of the grating length, the fiber core diameter and the metal grating layer thickness on the sensitivity *S* are not significant, while the grating period has a relatively strong influence on the sensitivity *S*. Furthermore the quality factor *Q* of the SPR dip is only lightly dependent on the grating length, the fiber core diameter, the metal grating layer thickness and the grating period.

In addition, a novel hybrid plasmonic biosensor based on a subwavelength RMG has been proposed and theoretically analyzed. Our investigations show that the wavelength dip related to HPCM has a higher *Q* value of 72.8 compared to the second dip due to CRM with *Q* value

of 33.1. The sensitivity of the dip related to HPCM from variations in the refractive index of the analyte layer is approximately twice than that of the dip related to CRM. The sensitivity of HPCM to the analyte layer thickness means that HPCM can be used to detect the thickness of a coating layer (i.e. an organic analyte) with a sensitivity of 75 *nm/um*. Finally by measuring the spectral response shifts of both HPCM and CRM dips, it is possible to use the proposed technique to detect both the RI and the thickness of specific biochemical targets or analytes simultaneously.

6.5 References

1. J. Feng, V. S. Siu, A. Roelke, V. H. Mehta, S. Y. Rhieu, G. T. R. Palmore, and D. Pacifici, Nanoscale plasmonic interferometers for multispectral high-throughput biochemical sensing, *Nano Lett.*, 12, pp. 602-609, (2012).
2. Y. K. Gao, Z. M. Xin, Q. Q. Gan, X. H. Cheng, and F. J. Bartoli, Plasmonic interferometers for label-free multiplexed sensing, *Opt. Express*, 21, pp. 5859-5871, (2013).
3. A. G. Brolo, Plasmonic for future biosensors, *Nature Photon.*, 6, pp. 709-713, (2012).
4. Y. Wang, X. G. Jiang, Q. Li, Y. Wang, and Z. Q. Cao, High-resolution monitoring of wavelength shifts utilizing strong spatial dispersion of guide modes, *Appl. Phys. Lett.*, 101, pp. 061106, (2012).
5. A. Abbas, M. J. Linman, and Q. Cheng, New trends in instrumental design for surface plasmon resonance-based biosensors, *Biosens. Bioelectron.*, 26, pp. 1815-1824, (2011).
6. B. H. Ong, X. Yuan, S. C. Tjin, J. Zhang, and H. M. Ng, Optimised film thickness for maximum evanescent field enhancement of a bimetallic film surface plasmon resonance biosensor, *Sens. Actuat. B.*, 114, pp. 1028–1034, (2006).
7. J. Dostálek, A. Kasry, and W. Knoll, Long range surface plasmons for observation of

biomolecular binding events at metallic surfaces, *Plasmonics*, 2, pp. 97-106, (2007).

8. A. Abdennour, J. L. Matthew, and C. Quan, Sensitivity comparison of surface plasmon resonance and plasmon-waveguide resonance biosensors, *Sens. Actuat. B.*, 156, pp. 169-175, (2011).

9. J. Albert, L. Y. Shao, and C. Caucheteur, Titled fiber bragg grating sensors, *Laser Photonic Rev.*, 7, pp. 83-108, (2013).

10. M. Piliarik, J. Homola, and J. Ctyroký, Surface plasmon resonance sensor based on a single-mode polarization-maintaining optical fiber, *Sens. Actuators B.*, 90, pp. 236–242, (2003).

11. C. Caucheteur, C. Chen, V. Voisin, P. Berini, and J. Albert, A thin metal sheath lifts the EH and HE degeneracy in the cladding mode refractometric sensitivity of optical fiber sensors, *Appl. Phys. Lett.*, 99, pp. 041118, (2011).

12. R. Jha, and G. Badenes, Effect of fiber core dopant concentration on the performance of surface plasmon resonance-based fiber optic sensor, *Sens. Actuators A.*, 150, pp. 212–217, (2009).

13. M. Piliarik, J. Homola, Z. Man´ıkova´, and J. Cˇ tyroky´, Surface plasmon resonance sensor based on a single-mode polarization-maintaining optical fiber, *Sens. Actuators B.*, 90, pp. 236–242, (2003).

14. S. K. Mishra, D. Kumari, and B. D. Gupta, Surface plasmon resonance based fiber optic ammonia gas sensor using ITO and polyaniline, *Sens. Actuators B.*, 171-172, pp. 976-983, (2012).

15. A. K. Sharma, and B.D. Gupta, On the sensitivity and signal to noise ratio of a step-index fiber optic surface plasmon resonance sensor with bimetallic layers, *Opt. Commun.*, 245, pp. 159–169, (2005).

16. A. Hosoki, M. Nishiyama, H. Lgawa, A. Seki, Y. Choi, and K. Watanabe, A surface plasmon resonance hydrogen sensor using Au/Ta2O5/Pd multi-layers on hetero-core optical fiber structures, *Sens. Actuators B.*, 185, pp. 53–58, (2013).

17. Karla Balaa , Malak Kanso, Stephane Cuenot, Tiberiu Minea, Guy Louarn, Experimental realization and numerical simulation of wavelength-modulated fibre optic sensor based on surface plasmon resonance, *Sen. Actuators B.*, 126, pp. 198–203, (2007).

18. Yinquan Yuan, Liyun Ding, Zhenqiang Guo, Numerical investigation for SPR-based optical fiber sensor, *Sen. Actuators B.*, 157 (1), pp. 240-245, (2011).

19. P. Bhatia, and B. D. Gupta, Surface-plasmon-resonance-based fiber-optic refractive index sensor: sensitivity enhancement, *Appl. Opt.*, 50, pp. 2032-2036, (2011).

20. C. W. Haggans, and L. F. Li, Effective-medium theory of zeroth-order lamellar gratings in conical mountings, *J. Opt. Soc. Am. A.*, 10, pp. 2217-2225, (1993).

21. Y. S. Dwivedi, A. K. Sharma, and B. D. Gupta, Influence of design parameters on the performance of a surface plasmon sensor based fiber optic sensor, *Plasmonics*, 3, pp. 79–86, (2008).

22. X. F. Li, and S. F. Yu, Long-wavelength optical transmission of extremely narrow slits via hybrid surfaceplasmon and Fabry-Perot modes, *J. Appl. Phys.*, 108 (1), pp. 013302, (2010).

23. X. Y. He, X. N. Fu, and Y. W. Luo, Analysis of the extraordinary transmission properties of arrays of sub-wavelength holes on a metal film in the terahertz region, *J. Mod. Opt.*, 56 (15), pp. 1698-1703, (2009).

24. M. Perino, E. Pasqualotto, A. Detoni, D. Garoli, M. Scaramuzza, P. Zilio, T. Ongarello, A. Paccagnella, and F. Romanato, Development of a complete plasmonic grating-based sensor and its application for self-assembled monolayer detection, *Appl. Opt.*, 53, pp.

5969-5976, (2014).

25. L. Pang, G. M. Hwnag, B. Slutsky, Y. Fainman, Spectral sensitivity of two dimensional nanohole array surface plasmon polariton resonance sensor, *Appl. Phys. Lett.*, 91, pp. 123112, (2007).

26. M. Hong, L. Shi, H. Li, Y. Du, Z. Wang, Y. Weng, and D. Li, Resonance in a sub-wavelength metal-dielectric free-standing grating utilized for gas sensors, *Opt. Commun*, 285, pp. 5480-5485, (2012).

27. A. Dhawan, M. Canva, and T. V. Dinh, Narrow groove plasmonic nano-gratings for surface plasmon resonance sensing, *Opt. Express*, 19, pp. 787-813, (2011).

28. M. Grande, R. Marani, F. Portincasa, G. Morea, V. Petruzzelli, A. D'Orazio, V. Marrocco, D. D. Ceglia, and M. A. Vincenti, Asymmetric plasmonic grating for optical sensing of thin layers of organic materials, *Sen. Actuators B.*, 160, pp. 1056-1062, (2011).

29. X. L. Sun, X. W. Shu, and C. H. Chen, Grating surface plasmon resonance sensor: angular sensitivity, metal oxidization effect of Al-based device in optimal structure, *Appl. Opt.*, 54, pp. 1548-1554, (2015).

30. N. Kato, L. Lee, R. Chandrawati, A. P. R. Johnston, and F. Caruso, Optically Characterized DNA Multilayered Assemblies and Phenomenological Modeling of Layer-by-Layer Hybridization, *J. Phys. Chem. C.*, 113 (50), pp. 21185–21195, (2009).

31. A.j Dhawan, S. J. Norton, M. D. Gerhold, and T. V. Dinh, Comparison of FDTD numerical computations and analytical multipole expansion method for plasmonics active nanosphere dimmers, *Opt. Express*, 17, pp. 9688-9703, (2009).

Chapter 7: Conclusions and future research work

This chapter presents the conclusions from across the thesis, and also discusses possible future research work as an extension of this PhD thesis.

7.1 Conclusions from the research

The primary focus of this thesis has been to improve the understanding, modeling, design and analysis of nanoplasmonic devices and their applications.

Based on the material presented in previous chapters, the key contributions of this thesis can be divided into seven areas: 1) the design and analysis of a metal-insulator-metal (MIM) plasmonic waveguide based Fabry-Perot (FP) cavity-coupled filter; 2) the design of an insulator-metal-insulator (IMI) plasmonic waveguide based polarization beam splitter (PBS); 3) the investigation and fabrication of a microfiber loaded SPPs (MFLSPPs) based TE-pass polarizer; 4) the design of a long-range dielectric loaded SPPs (LRDLSPPs) based waveguide offering a better tradeoff between the propagation length and mode confinement; 5) the development of two ultra-tight mode confinement hybrid SPPs (HSPPs) waveguides with an optimized tradeoff: a long range nanowedge HSPPs (LRWHSPPs) waveguide and a long range wedge-to-wedge HSPPs (LRWWHSPPs) waveguide; 6) the analysis of a multimode fiber based SPPs biosensor coated with a subwavelength metal grating (MG) layer; 7) the design of a subwavelength reflection metal grating (RMG) based biosensor for simultaneous detection of the refractive index and thickness of the analyte layer.

The major conclusions and insights gained for each of these areas is now discussed in detail.

1. Design of a metal-insulator-metal plasmonic Fabry-Perot cavity-coupled filter with nanocavity resonators

In this thesis an ultra-compact FP cavity-coupled filter is numerically investigated utilizing the FDTD method and an analytical FP cavity model. The filter consists of a MIM waveguide with nanocavity resonators. The SPPs propagating within the insulator waveguide can be captured by the nanocavity under resonance conditions which in turn induces dips in the transmission spectrum. The key conclusions from the studies in this area can be drawn as follows:

- The simulation results demonstrate that the transmission band for the filter can be modified by adjusting the geometrical characteristics of the nanocavity.
- For a single-channel filter, the resonance wavelengths show a linear red shift with the slope of 1.742 nm/μm as a function of the nanocavity length and a nonlinear blue-shift with respect to the nanocavity width.
- A dual-channel filter is designed, which shows that the location of the two nanocavities (for example, a nanocavity on either side of the waveguide or both nanocavities on the same side of the waveguide), as well as the distance between the nanocavities, has only a marginal effect on the spectral response of the filter.

2. Analysis of a polarization beam splitter based on the IMI plasmonic waveguide

In this thesis a novel compact PBS with low insertion loss and high extinction ratio is investigated in both two-dimensional (2D) and two-dimensional (3D) models using the FEM. The PBS is based on a three-core plasmonic directional coupler, which utilizes the polarization selective coupling principle between a long range SPPs (LRSPPs) waveguide and a conventional dielectric waveguide. From the studies, it can be concluded that:

- Both 2D model and 3D models have been constructed and simulation results show that 2D model has similar results compared to 3D model, but with a computing time several times shorter.

- With appropriate structural parameters, the PBS can be realized with a low insertion loss of 0.17 dB and a high extinction ratio of 20.17 dB, at a wavelength of 1550 nm for TE polarizaiton.

- The PBS can achieve a low insertion loss of 0.25 dB and a high extinction ratio of 19.83 dB at a wavelength of 1550 nm for TM polarization.

- The PBS can achieve an insertion loss lower than 0.5 dB and an extinction ratio of higher than 14 dB across the entire C-band for both TE and TM polarizations.

3. Demonstration of a MFLSPPs based TE-pass polarizer

A novel surface plasmon TE-pass polarizer, consisting of an optical microfiber placed on a silver coated glass substrate, is theoretically investigated (by means of the FEM) and experimentally demonstrated in this thesis. The microfiber was fabricated using the standard micro-heater brushing-tapering technique. From both the numerical simulation and experimental results, it can be concluded that:

- The fundamental TM mode suffers from a large metal dissipation loss induced by the excited microfiber-loaded surface plasmon mode where a portion of the energy is located on the metal surface.

- The loss for the fundamental TE mode is relatively low due to the fact that the TE mode will not couple to the surface plasmon mode and hence the largest portion of the energy is located within the microfiber.

- By the appropriate selection of structural parameters, the proposed structure can realize a low insertion loss (< 1.6 dB) for TE mode over the wavelength range from 1500 to 1600 nm.

- With appropriate structural parameters, the proposed structure can realize a relatively high insertion loss (> 22 dB) for TM mode over the wavelength range from 1500 to 1600 nm.

- A polarization extinction ratio greater than 20 dB over the whole wavelength range from 1500 nm to 1600 nm is achieved.

4. A LRDLSPPs waveguide offering a better tradeoff between mode confinement and propagation length

In this thesis, a novel LRDLSPPs waveguide offering lower loss but with a higher degree of mode confinement is proposed and investigated using the FEM. The waveguide utilizes the configuration of conventional LRDLSPPs but with an altered metallic geometry.

With the appropriate selection of structural parameters, it can be concluded that:

- For the same mode confinement, the proposed LRDLSPPs waveguide can significantly improve the propagation length by up to six times compared to the conventional LRDLSPPs waveguide.

- For the same propagation length, the proposed LRDLSPPs waveguide can realize a 2-fold tighter field confinement compared to a conventional LRDLSPPs waveguide.

- The proposed LRDLSPPs waveguide offers a lower crosstalk compared to a conventional LRDLSPPs waveguide for the vertically parallel case.

- The proposed LRDLSPPs waveguide offers a similar crosstalk compared to the conventional LRDLSPPs waveguide for the horizontally parallel case.

5. Design of a LRWHSPPs waveguide and a LRWWHSPPs waveguide achieving both a long propagation length and subwavelength mode confinement

To further mitigate the tradeoff between the mode confinement and propagation length, two novel HSPPs waveguides are proposed and investigated in this thesis, identified as a LRWHSPPs waveguide and a LRWWHSPPs waveguide. The coupling between the dielectric waveguide and LRSPPs modes results in a novel hybrid plasmonic mode featuring both long propagation length and strong mode confinement. The conclusions from these studies are:

- With the appropriate structural parameters, the LRWHSPPs waveguide could offer a very useful capability for low loss (propagation length ranges from 1200 μm to 3500 μm) and deep-subwavelength (mode area ranges from $\lambda^2/4000$ to $\lambda^2/400$) light confinement.

- If the refractive index (RI) for the cladding material is deliberately lowered for the LRWHSPPs waveguide, this not only extends the propagation length but also improves the mode confinement.

- By comparison to the HSPPs waveguide reported in [1], the propagation length and the mode confinement of the LRWHSPPs waveguide demonstrates at least a 60-fold and a 5-fold enhancement respectively.

- Compared to the WHSPPs proposed in [2], the LRWHSPPs waveguide has relatively worse mode confinement (roughly twice the mode area), but has 40 times longer propagation length.

- By comparison to the LRHSPPs waveguide reported in Ref. 3, the LRWHSPPs waveguide offers a similar propagation length, but has an order of magnitude higher level of mode confinement.

- Compared to the BTHSPPs (SBTHSPPs) waveguide in Ref. 4, the LRWHSPPs waveguide demonstrates at least a 3-fold (6-fold) and 30-fold (1.5-fold) enhancement for the mode confinement and propagation length compared to those of the BTHSPPs (SBTHSPPs) waveguide respectively.

- Compared to the LRWHSPPs waveguide, the LRWWHSPPs waveguide demonstrate sa 2.4-fold extended propagation length for the same mode confinement or a 9-fold enhancement in mode confinement for the same propagation length, indicating that the LRWWHSPPs waveguide would achieve the best tradeoff compared to the recently published structures.

- Both the LRWHSPPs and LRWWHSPPs waveguides have an acceptable tolerance to fabrication errors, for example, the uneveness of dielectric waveguide surface and the misalignment between the Ag nanowedges and Si waveguides.

6. Analysis of a multimode fiber biosensor coated with a subwavelength metal grating layer

In this thesis, a novel multimode fiber based plasmonic biosensor is studied by means of the transfer-matrix method. Compared to the configuration of a conventional multimode fiber biosensor coated with uniform metal layer, the proposed biosensor utilizes an embedded subwavelength metal grating layer to replace the uniform metal layer. The conclusions from the studies are:

- With the appropriate selection of structural parameters, the proposed biosensor has an estimated sensitivity of 3892 nm/RIU (refractive index unit) in the RI range from

1.333-1.353.

- The proposed biosensor has an estimated sensitivity of 13000 nm/RIU in the RI range from 1.395 to 1.40.

- It has been demonstrated that the fiber based SPPs biosensor with a subwavelength metal grating layer offers an at least a 3-fold enhanced sensitivity compared to the sensor with a uniform metal layer.

- It has been demonstrated that the grating length, the fiber core diameter and the metal grating layer thickness all have a moderate effect on the sensitivity of the sensor.

- It has been demonstrated that the grating period has a relatively strong influence on the sensitivity.

- The quality factor of the SPR dip is weakly dependent on the grating length, the fiber core diameter, the metal grating layer thickness and the grating period.

7. Design of a subwavelength plasmonic grating based sensor for simultaneous measurement of both thickness and the refractive index of the analyte layer

A novel subwavelength RMG based sensor is reported and characterized by the FEM. Investigations on the mode properties of the cavity resonance mode (CRM) and hybrid plasmonic-cavity mode (HPCM) demonstrate that it is possible to determine both refractive index and thickness of the analyte layer simultaneously. The main conclusions from this study are:

- The width of the reflection dip related to the HPCM is much narrower than that of the CRM: the *Q* value for the HPCM dip is 72.8, which is twice that compared with 33.1 for the CRM dip.

- The field distribution of the HPCM offers a larger overlap with the surrounding analyte compared to the CRM, thus the HPCM is more likely to be affected by the analyte propertries, such as the RI and thickness.

- For measurement of RI variation of the analyte $\triangle n$: the sensor involving the CRM has an estimated sensitivity ($\triangle\lambda/\triangle n$) of 240 *nm*/RIU, while the sensitivity of that involving the HPCM is 448 *nm*/RIU.

- For measurement of thickness variation of the analyte layer $\triangle d$: the reflection dip caused by the CRM remains substantially unchanged, while the dip associate with the HPCM offers an estimated sensitivity ($\triangle\lambda/\triangle d$) of 75 *nm/um*.

- The results obtained from the measurements of RI and thickness variations for the analyte layer confirm a useful possibility to distinguish and measure both the thickness and RI simultaneously.

7.2 Future research

For the future work, there are a number of research topics and directions that could extend further the research presented in this thesis.

1. Implementation of the devices proposed in this thesis

The most immediate extension of this work should be further experimental verification of the devices proposed and investigated in this thesis, building on the reported proof of concept experiment based on a microfiber loaded SPPs (MFLSPPs) TE-pass polarizer that has been carried out, showing a good agreement between simulation and experimental results.

2. Extend potential applications of the proposed LRWWHSPPs waveguide

The emerging field of nanophotonics requires coherent light sources free from the limitations imposed by the diffraction limit, which in turn could be used to investigate rich physical phenomena at a nanometer scale [5]. On the other hand, due to the ever-increasing demands for trapping and manipulating biological and non-biological particles (such as cells, viruses and molecules), nanotweezers have been attracting more and more attentions [6].

The proposed LRWWHSPPs waveguide offers three distinct advantages: (1) its subwavelength mode confinement enables it to overcome the diffraction limit; (2) its low propagation loss generally could minimize the material gain required to reach the lasing threshold [5]; (3) its large gradient of the light field in the nanogap could give rise to an enhanced optical force [6]. Therefore, new kinds of LRWWHSPPs waveguide based devices can be explored, for example for applications in the areas of nanolasers and nanotweezers.

3. Exploration of active plasmonic waveguides using gain medium as loss compensation

Guiding light beyond the diffraction limit is a promising route for development of miniaturized integrated photonic circuits (IPCs). However, the propagation loss increases with the confinement factor, posing a fundamental problem in many potential applications. How to balance the tradeoff between the propagation loss and mode confinement is one of the critical considerations for SPPs waveguides. Although the proposed LRWWHSPPs waveguide in this thesis could potentially balance this tradeoff and can act as a guideline for further exploration of plasmonic waveguides, the propagation loss is still a limitation. Thus new strategies are needed to reduce this intrinsic loss still further. Recently researchers have explored the possibility of loss compensation using a gain medium [7-8]. For example, a

plasmonic mode power gain of 8.55 dB mm^{-1} has been achieved by incorporating optically pumped dye molecules as the gain medium [8]. Loss compensation for the deep-subwavelength confined SPPs could also be one of the future tasks.

7.3 References

1. R. F. Oulton, V. J. Sorger, D. A. Genov, D. F. P. Pile, and X. Zhang, A hybrid plasmonic waveguide for subwavelength confinement and long-range propagation, *Nat.Photonics*, 2 (8), pp. 496-500, (2008).
2. Y. S. Bian, Z. Zheng, Y. Liu, J. S. Liu, J. S. Zhu, and T. Zhou, Hybrid wedge plasmon polariton waveguide with good fabrication-error-tolerance for ultra-deep-subwavelength mode confinement, *Opt. Express*, 19, pp. 22417-22422, (2011).
3. L. Chen, T. Zhang, X. Li, and W. P. Huang, Novel hybrid plasmonic waveguide consisting of two identical dielectric nanowires symmetrically placed on each side of a thin metal film, *Opt. Express*, 20, pp. 20535-20544, (2012).
4. Y. S. Bian, and Q. H. Gong, Bow-tie hybrid plasmonic waveguides, *J. Lightw. Technol.*, 32, pp. 3902-3907, (2014).
5. R. M. Ma, R. F. Oulton, V. J. Sorger, and X. Zhang, Plasmon lasers: coherent light source at molecular scales, *Laser Photonic Rev.*, 7, pp. 1-21, (2012).
6. X. D. Yang, Y. M. Liu, R. F. Oulton, X. B. Yin, and X. Zhang, Optical forces in hybrid plasmonic waveguides, Nano Lett., 11, pp. 321-328, (2011).
7. J. Grandidier, G. C. D. Francs, S. Massenot, A. Bouhelier, L. Markey, J. C. Weeber, C. Finot, and A. Dereux, Gain-assisted propagation in a plasmonic waveguide at telecom wavelength, Nano. Lett., 9, pp. 2935-2939, (2009).
8. I. D. Leon, and P. Berini, Amplification of long-range surface plasmons by a dipolar gain

medium, *Nature Photon.*, 4, pp. 382-387, (2010).